



**Improving the durability and performance of
hollow fibre membranes with nanocomposite and
inorganic/organic hybrid materials**

Chi Yan Lai

Bachelor of Engineering (Chemical Engineering) (Honours)

Institute for Sustainability and Innovation
College of Engineering and Science
Victoria University

*Submitted in fulfilment of the requirements of the degree of Doctor of
Philosophy*

(2014)

Abstract

Water is a vital element for our existence but secure supply is challenged by population pressures and climate change. To ensure water security, it is essential to explore new sources and to recycle water for non-potable applications to reduce demand for the more valuable potable water. Membranes are key to the ability to treat such water sources to the required quality. Seawater pretreatment for reverse osmosis (RO) with microfiltration (MF) and ultrafiltration (UF) membranes is technically and economically feasible with significant advantages over conventional granular media filtration. In these applications, current commercial MF and UF membranes may have shorter lifespans and can wear irreversibly over time, especially in the presence of abrasive particles in seawater and other challenging water sources. Recent work in the literature has shown that the physical strength, flux and antifouling properties of membranes can be improved by incorporation of nanoparticles. In this work, advanced nanocomposite membranes were prepared and studied for improvements in physical durability with particular interest in resistance to abrasion. Very little is currently published in the open literature on this subject possibly due to the economic and regulatory sensitive nature of the issue.

Commercially available montmorillonite nanoclays with organic modifiers were dispersed into the solvent 1-methyl-2-pyrrolidinone (NMP) with various techniques. A new approach using high energy mixing with a microfluidizer reduced the nanoclay clusters to the smallest size; other conventional methods including ultrasonication, planetary centrifugal mixing and overhead stirring also had varying degrees of success in dispersing nanoclay into the solvent. Microfluidization resulted in a more homogenous membrane with superior mechanical strength and therefore it was used for the optimised approach applied to fabrication of hollow fibres, which were the main membrane type to be studied for enhanced durability in this work.

Nanocomposite poly(vinylidene fluoride) (PVDF)/nanoclay flat sheet membranes were then prepared by non-solvent induced phase separation (NIPS) and tested for abrasion resistance using a conventional tribological technique. Their material properties were characterized using Fourier-transform infrared spectroscopy (FTIR), thermogravimetric analysis (TGA), tensile testing, scanning electron microscopy (SEM), energy dispersive spectroscopy (EDS) and small angle X-ray scattering (SAXS) at the Australian Synchrotron. Nanoclay Cloisite[®] 15A was selected as the inorganic nanoparticle incorporated into the PVDF membranes. FTIR results showed a shifting of the PVDF crystalline phase from α to β by which the nanoclay altered the PVDF host

material's structure and mechanical properties in terms of stiffness and toughness. Water permeation tests showed that nanoclay at low concentration tended to reduce water flux. The nanocomposite membranes showed phase separated morphology at high loading as shown by SAXS. Although they were not fully exfoliated, all nanocomposite membranes with between 1 wt% and 5 wt% initial nanoclay loading, were more abrasion resistant than the control PVDF membrane. However, the membrane with 1 wt% nanoclay exhibited superior resistance, lasting two times longer than the reference PVDF membrane under the same abrasive condition. The 1 wt% nanoclay membrane appeared less abraded by SEM observation while also having the greatest tensile strength improvement (from 4.5 MPa to 4.9 MPa). Besides, this membrane had the smallest agglomerated nanoclay particle size and highest toughness compared to the higher nanoclay content membranes.

To further understand the impact of casting conditions on membrane properties including PVDF crystalline phase, membrane morphology and nanoclay retention, various parameters were investigated. They included the retention time of casting dope in air, temperature and composition of the quench bath, the PVDF/NMP ratio of the dope as well as the humidity of the casting environment. The effect of nanoclays with different organic modifiers and PVDF with various molecular weights were also studied. The inorganic content of the membranes were measured with both TGA and loss on ignition (LOI) since nanoclay can be lost to the quench medium during the phase inversion process. Nanoclays with hydrophilic modifiers tended to form membranes with larger macrovoids, and membranes modified with Nanomer[®] I.30E had the highest nanoclay retention. Long air exposure time prior to immersion had a negative impact on nanoclay retention while adding sodium chloride to the quench bath helped retain nanoclay. Despite the slight changes, nanoparticle retentions were in the order of 32% to 48%.

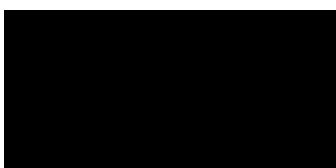
The knowledge gained from dispersion and flat sheet studies was successfully transferred to the more commercially applicable hollow fibre membrane format fabricated by NIPS. LOI testing has shown high nanoclay retention was achieved at low initial nanoclay loading. The incorporation of nanoclay shifted the PVDF crystalline phase from α -phase to β -phase and improved the membrane structure as well as mechanical properties in terms of stiffness and flexibility. Tensile strength increased from 3.8 MPa to 4.3 MPa with 5.08 wt% Cloisite[®] 30B loading while break extension increased from 175% to 229% with 5.08 wt% Nanomer[®] I.44P nanoclay loading. Despite showing lower pure water permeability, nanocomposite membranes exhibited

similar or slightly improved fouling performance when tested with bovine serum albumin (BSA) and sodium alginate model foulant solutions. An accelerated abrasion test was developed for the hollow fibres using abrasive slurry and bubble point as a measure of the deterioration of the membrane. This test revealed the membrane with an initial 5.08% loading of Nanomer[®] I.44P had the most improved abrasion resistance, lasting three times longer than the control membrane with no nanoclay addition. PVDF membranes containing commercial nanoclay are therefore promising for improved durability and performance in water treatment applications.

Declaration by author

"I, Chi Yan Lai, declare that the PhD thesis entitled Improving the durability and performance of hollow fibre membranes with nanocomposite and inorganic/organic hybrid materials is no more than 100,000 words in length including quotes and exclusive of tables, figures, appendices, bibliography, references and footnotes. This thesis contains no material that has been submitted previously, in whole or in part, for the award of any other academic degree or diploma. Except where otherwise indicated, this thesis is my own work."

Signature



Date 7/10/2014

Publications during candidature

- [1] C.Y. Lai, A. Groth, S. Gray, and M. Duke, *Preparation and characterization of poly(vinylidene fluoride)/nanoclay nanocomposite flat sheet membranes for abrasion resistance*, Water Research, 57 (2014) 56-66.

- [2] C.Y. Lai, A. Groth, S. Gray, and M. Duke, *Nanocomposites for improved physical durability of porous PVDF membranes*, Membranes, 4 (2014), 55-78.

- [3] C.Y. Lai, A. Groth, S. Gray, and M. Duke, *Enhanced abrasion resistant PVDF/nanoclay hollow fibre composite membranes for water treatment*, Journal of Membrane Science, 449 (2014) 146-157.

- [4] C.Y. Lai, A. Groth, S. Gray, and M. Duke, *Investigation of the dispersion of nanoclays into PVdF for enhancement of physical membrane properties*, Desalination and Water Treatment, 34 (2011) 251-256.

- [5] C.Y. Lai, A. Groth, S. Gray, and M. Duke, *Impact of casting conditions on PVDF/nanoclay nanocomposite membrane properties*, Chemical Engineering Journal, (2014) Submitted.

Presentations during candidature

Oral presentations

- [1] M. Duke, C.Y. Lai, A. Groth, S. Gray, *PVDF/Inorganic Composite Membranes for Improving Physical Durability in Water Treatment*, 10th International Conference on Membranes and Membrane Processes, Suzhou, China, 20-25 July 2014, Paper OR-7-01110. (Keynote presentation)
- [2] C.Y. Lai, A. Groth, S. Gray, and M. Duke, *Structure-morphology property relationships of PVdF/nanoclay membranes*, Membrane Society of Australasia, 3rd Early Career Researcher Symposium, Brisbane Australia, 28-30 November 2012.
- [3] C.Y. Lai, A. Groth, S. Gray, and M. Duke, *Preparation and characterisation of PVdF/nanoclay hollow fibre composite membranes*, 7th Conference of the Aseanian Membrane Society, Busan, Korea, 4-6 July 2012, Paper ORS2-034.
- [4] C.Y. Lai, A. Groth, S. Gray, and M. Duke, *Incorporation of nanoparticles into PVdF membranes via phase inversion*, Membrane Society of Australasia, 2nd Early Career Researcher Symposium, Adelaide, Australia, 23-25 November 2011.

Poster presentations

- [1] C.Y. Lai, A. Groth, S. Gray, and M. Duke, *Fouling study of abrasion resistant PVDF/nanoclay hollow fibre composite membranes*, 8th International Membrane Science and Technology Conference, Melbourne, Australia, 25-29 November 2013.
- [2] C.Y. Lai, A. Groth, S. Gray, and M. Duke, *Preparation and characterisation of poly(vinylidene fluoride)/nanoclay composite membranes*, AWA Membranes and Desalination Specialty IV Conference, Gold Coast, Australia, 9-11 February 2011, Paper P01.
- [3] C.Y. Lai, A. Groth, S. Gray, and M. Duke, *Dispersion of nanoclays in PVdF membranes for water treatment*, 7th International Membrane Science and Technology Conference in conjunction with 6th Conference of the Aseanian Membrane Society, Sydney, Australia, 22-25 November 2010. (Prize for the best student poster presentation)

Acknowledgements

I would like to thank my supervisors, Prof Mikel Duke (Victoria University), Prof Stephen Gray (Victoria University) and Dr Andrew Groth (Memcor Products), for their continual support and guidance throughout the project. I am very grateful for this opportunity to learn from their expertise and experience in membrane research. Their motivation and patience throughout my entire study is greatly appreciated.

Special thanks to Dr Marlene Cran, Mr Nole Dow, Ms Catherine Enriquez, Dr Darli Myat, Dr Nicolas Milne, Dr Jianhua Zhang, and Dr Bo Zhu from Victoria University, Dr Ludovic Dumez, Dr Mary She and Ms Rosey van Driel from Deakin University, Dr Zongli Xie, Mr John Ward, Mr Mark Greaves, Mr Mark Hickey and Ms Karen Wiener from CSIRO for their advice and assistance in the project. Furthermore, I wish to extend my sincere gratitude to Dr Clem Powell and the Memcor Products R&D department during my two-month visit in 2011.

I would also like to acknowledge the financial support from the Australia Research Council Linkage Project LP100100103, Memcor Products, Evoqua Water Technologies and National Centre of Excellence in Desalination Australia which is funded by the Australian Government through the National Urban Water and Desalination Plan.

Finally, I am thankful to my family and friends for their support and encouragement throughout my PhD study. Without them, I could not possibly finish this incredible journey.

I dedicate this thesis to the memory of my grandfather, Yee Kau Lai.

Table of Contents

Abstract	i
Declaration by author	iv
Publications during candidature	v
Presentations during candidature	vi
Oral presentations	vi
Poster presentations	vi
Acknowledgements	vii
List of figures	xi
List of tables	xv
List of abbreviations	xvii
1. Introduction	1
1.1. The water issue and role of membrane technology	1
1.2. Current performance issues	3
1.2.1 Membrane fouling.....	3
1.2.2 Physical durability.....	5
1.3. Polymer composite and nanocomposite	7
1.4. Summary and research scope	8
2. Literature review	9
2.1. Introduction	9
2.2. Polymeric membranes	9
2.2.1 Membrane materials.....	9
2.2.2 Membrane fabrication.....	10
2.3. PVDF nanocomposites	18
2.3.1 PVDF	18
2.3.2 Nanofillers	19
2.3.3 Synthesis of PVDF/nanoclay nanocomposites.....	28
2.4. Abrasion theory	30
2.5. Objective of this work	31
3. Experimental	33
3.1. Materials	33
3.2. Dispersion of nanoclay	36

3.2.1	Methods to disperse nanoclay.....	36
3.2.2	Characterization of dispersions	36
3.3.	Membrane preparation.....	37
3.3.1	Flat sheet membrane preparation	37
3.3.2	Membrane preparation for optimization of nanoclay inclusion	37
3.3.3	Hollow fibre membrane preparation	39
3.4.	Characterization of membranes.....	41
3.4.2	Thermal decomposition	41
3.4.3	Characterisation of polymer crystalline phase.....	43
3.4.4	Small angle X-ray scattering	44
3.4.5	Electron microscopy	45
3.4.6	Porosity and average pore size (hollow fibre membranes)	46
3.4.7	Mechanical testing.....	47
3.4.8	Abrasion testing.....	47
3.4.9	Membrane permeation testing.....	50
3.4.10	Fouling resistance testing.....	51
4.	Investigation of effective methodology to disperse nanoclays	53
4.1.	Results and Discussion	53
4.1.1	Dispersion with conventional methods	53
4.1.2	Dispersion with microfluidizer	57
4.1.3	Nanoclay distribution in membrane	60
4.2.	Conclusions	65
5.	Preparation and characterization of PVDF/nanoclay nanocomposite flat sheet membranes for material properties and durability assessment	68
5.1.	Membrane preparation and characterization.....	68
5.2.	Results and Discussion	69
5.2.1	TGA.....	69
5.2.2	Effect of nanoclay on membrane crystal structure	71
5.2.3	Effect of nanoclay on membrane morphology.....	72
5.2.4	Dispersion of nanoclay particles.....	77
5.2.5	Effect of nanoclay on water flux	79
5.2.6	Effect of nanoclay on mechanical properties.....	80
5.2.7	Effect of nanoclay on abrasion resistance.....	82
5.3.	Conclusions	85

6. Impact of casting conditions on membrane properties.....	87
6.1. Results and discussion	87
6.1.1 Effect of various nanoclays	87
6.1.2 Effect of casting conditions on membrane morphology.....	91
6.1.3 Effect of casting conditions on nanoclay retention	96
6.1.4 Effect of casting conditions on membrane crystal phase	98
6.1.5 Effect of casting conditions on mechanical properties	99
6.2. Conclusions	100
7. Enhanced abrasion resistant PVDF/nanoclay hollow fibre composite	
membranes for water treatment.....	102
7.1. Membrane preparation and characterization.....	102
7.2. Results and Discussion	102
7.2.1 Nanoclay retention by LOI.....	102
7.2.2 Effect of nanoclay on membrane material crystal structure	104
7.2.3 Effect of nanoclay on membrane morphology.....	106
7.2.4 Pure water permeability.....	112
7.2.5 Membrane fouling studies	113
7.2.6 Mechanical properties	116
7.2.7 Abrasion resistance.....	118
7.3. Conclusions	124
8. Conclusions and recommendations.....	126
8.1. Conclusions	126
8.2. Recommendations for future work.....	128
Reference	130

List of figures

Figure 1-1. Typical membrane processes and applications	2
Figure 1-2. Sand particle abrasion	6
Figure 2-1. Flat sheet fabrication by hand casting (a) and membrane casting machine (b)	12
Figure 2-2. Schematic diagram of the wet spinning apparatus	13
Figure 2-3. Schematic diagram of a typical asymmetric flat sheet membrane cross-section	14
Figure 2-4. Conformation of PVDF α - and β -phase.....	18
Figure 2-5. The structure of 2:1 layered silicate	22
Figure 2-6. Schematic of three main types of polymer/layer structure composite morphologies: (a) microcomposites, (b) intercalated nanocomposites, and (c) exfoliated nanocomposites.....	28
Figure 2-7. TEM image of precipitated 2 wt% Cloisite 15A/PVDF after hot-pressing into a film.....	29
Figure 2-8. A plot of wear rate as a function of the reciprocal of the product of tensile strength and elongation at max load.	31
Figure 3-1. X-ray diffraction patterns (a) and FTIR spectra (b) of PVDF and PVDF/30B nanocomposite membranes.	44
Figure 3-2. Sample plate for SAXS	45
Figure 3-3. Setup for each membrane fibre in the slurry flask for the abrasion resistance testing	49
Figure 3-4. Bubble point of the membranes during the initial abrasion testing to confirm the abrasion testing experiment used in this work	50
Figure 3-5. Schematic diagram of dead-end hollow fibre filtration unit.....	52
Figure 4-1. SEM image of dry Cloisite [®] 30B particles	54
Figure 4-2. Z-average particle size of Cloisite [®] 30B dispersed in NMP vs mixing time using various mixing techniques.	55
Figure 4-3. Size distribution by intensity of Cloisite [®] 30B dispersed with ultrasonication at various time intervals.....	56
Figure 4-4. Size distribution by intensity of Cloisite [®] 30B (a) and Nanomer [®] I.30E (b) dispersed in NMP with microfluidizer and Z-average particle size of the nanoclays (c).	58
Figure 4-5. Size distribution by intensity of Cloisite [®] 30B using different dispersion methods.....	58

Figure 4-6. Z-average particle size of microfluidized nanoclay particles redispersed by ultrasonication after 12 days or more of stagnation	59
Figure 4-7. SAXS patterns of (a) PVDF/30B membranes & Cloisite® 30B powder and (b) PVDF/I30E membranes and Nanomer® I.30E powder	61
Figure 4-8. TEM image of PVDF/I30E-M membrane	62
Figure 4-9. Backscattering SEM and Si mapping images using EDS of PVDF/I30E 5% membrane quench side surface dispersed by (a) ultrasonication and (b) microfluidizer.	64
Figure 5-1. TGA thermograms of PVDF composite membranes and Cloisite® 15A.....	69
Figure 5-2. FTIR spectra of the membranes	71
Figure 5-3. Cross-sectional morphology of (a) PVDF/15A-0, (b) PVDF/15A-1, (c) PVDF/15A-2, (d) PVDF/15A-3 and (e) PVDF/15A-3 (edge).....	74
Figure 5-4. Backscattering SEM and silicon mapping images using EDS of membrane quench side surface: (a) PVDF/15A-0, (b) PVDF/15A-1, (c) PVDF/15A-2 and (d) PVDF/15A-3	76
Figure 5-5. SAXS patterns of membranes and Cloisite® 15A powder	78
Figure 5-6. Impact of nanoclay on (a) membrane water flux (175 kPa) and (b) water flux times skin thickness (specific skin flux)	80
Figure 5-7. Young's modulus and modulus of toughness of PVDF composite membranes	82
Figure 5-8. Weight loss per unit area of membrane after 200 abrasion cycles with two different grades of sand paper	83
Figure 5-9. SEM images of membrane surface after abrasion testing: (a) PVDF/15A-0, (b) PVDF/15A-1, (c) PVDF/15A-2 and (d) PVDF/15A-3. Original surface is shown as inset in each image.....	84
Figure 6-1. Cross-section morphology of (a) PVDF, (b) PVDF/10A, (c) PVDF/15A, (d) PVDF/30B, (e) PVDF/I28E, (f) PVDF/I30E, (g) PVDF/I31PS, (h) PVDF/I34TCN and (i) PVDF/I44P membranes.	90
Figure 6-2. Cross-section morphology of PVDF/I30E membranes prepared with retention time of (a) 0 minutes, (b) 1 minute, (c) 5 minutes and (d) 10 minutes....	92
Figure 6-3. Cross-section morphology of PVDF/I30E membranes prepared with quench bath temperature at (a) 20°C, (b) 40°C and (c) 60°C.....	93
Figure 6-4. Cross-section morphology of PVDF/I30E membranes prepared with (a) water, (b) 10% NaCl & 90% water, (c) 10% NMP & 90% water and (d) 10% glycerol & 90% water as the quench bath medium.	94

Figure 6-5. Cross-section morphology of PVDF/I30E membranes prepared at (a) 30%RH and (b) 90%RH.....	95
Figure 6-6. Cross-section morphology of PVDF/I30E membranes prepared with ratio of PVDF/nanoclay to NMP at (a) 10:90, (b) 15:85 and (c) 20:80.	95
Figure 6-7. Cross-section morphology of PVDF/I30E membranes prepared with PVDF molecular weight of (a) 244 kDa (Solef [®] 6008), (b) 573 kDa (Solef [®] 1015) and (c) 687 kDa (Solef [®] 6020).....	96
Figure 6-8. F_{β} vs percentage of nanoclay retained in PVDF/I30E membranes prepared with various casting conditions.....	99
Figure 7-1. Percentage of nanoclay from the NMP solution retained in the membranes	104
Figure 7-2. FTIR spectra of membranes incorporated with Cloisite [®] 30B (a) and Nanomer [®] I.44P (b)	105
Figure 7-3. Actual nanoclay loading vs F_{β} of membranes.	106
Figure 7-4. SEM and X-ray Si mapping images using EDS of membrane cross-section: (a) 0% Nanoclay, (b) 30B 0.88, (c) 30B 2.61, (d) 30B 5.08, (e) I44P 0.88, (f) I44P 2.61 and (g) I44P 5.08.....	108
Figure 7-5. Backscattering SEM and X-ray Si mapping images using EDS of membrane outer surface: (a) 0% Nanoclay, (b) 30B 0.88, (c) 30B 2.61, (d) 30B 5.08, (e) I44P 0.88, (f) I44P 2.61 and (g) I44P 5.08	110
Figure 7-6. Impact of nanoclay on (a) overall water permeability and (b) permeability times skin thickness (material permeability).....	112
Figure 7-7. TMP of 0% Nanoclay membrane during BSA filtration using 100 ppm BSA, 450 ppm NaCl, 50 ppm CaCl ₂ at 50 L/m ² h, 20°C.....	113
Figure 7-8. TMP after backwashing during BSA filtration using 100 ppm BSA, 450 ppm NaCl, 50 ppm CaCl ₂ at 50 L/m ² h, 20°C.....	114
Figure 7-9. Relative TMP of membranes after backwashing during (a) BSA filtration using 100 ppm BSA, 450 ppm NaCl, 50 ppm CaCl ₂ at 50 L/m ² h, 20°C and (b) alginate filtration using 100 ppm sodium alginate, 450 ppm NaCl, 50 ppm CaCl ₂ at 50 L/m ² h, 20°C.	115
Figure 7-10. Relative bubble point (a) and maximum pore size (b) of the membranes during the abrasion test.....	119
Figure 7-11. Time taken for 10% decrease in bubble point on abraded membranes.	121
Figure 7-12. SEM images of membrane surface before and after the abrasion test: (a) 0% Nanoclay and (b) I44P 5.08	122

Figure 7-13. Abrasion rate normalised by membrane thickness	123
Figure 7-14. Proposed model for abrasion of (a) unmodified membrane and (b) the mechanically stabilized PVDF/nanoclay membrane	124

List of tables

Table 1-1. Properties of various fouling types	3
Table 2-1. Typical parameters used to control production of flat sheet and hollow fibre membrane casting.....	17
Table 2-2. Summary of selected PVDF nanocomposite membranes prepared by NIPS	26
Table 3-1. Properties of PVDF raw materials	33
Table 3-2. Properties of nanoclays.....	34
Table 3-3. Standard casting conditions.	38
Table 3-4. Composition of the quench bathes.....	39
Table 3-5. Mechanical properties of membranes	40
Table 3-6. Membrane composition	40
Table 3-7. Composition of the foulant solutions	52
Table 4-1. Composition of synthesis solutions and dispersion method.....	60
Table 4-2. Mechanical properties of membranes	65
Table 4-3. Summary of key parameters of membranes prepared by different dispersion methods.....	67
Table 5-1. Composition of synthesis solutions	68
Table 5-2. Comparison between original and actual inorganic loading	70
Table 5-3. F_{β} of membranes.....	72
Table 5-4. Overall membrane thickness and average thickness of skin layer.....	77
Table 5-5. Comparison of the casting conditions of PVDF/Cloisite [®] 15A nanocomposites	79
Table 5-6. Mechanical properties of membranes	81
Table 5-7. Summary of key parameters of PVDF/15A membranes.	86
Table 6-1. Percentage of nanoclay retained in membranes using different types of nanoclays and F_{β} of the membranes.....	88
Table 6-2. Percentage of nanoclay retained in membranes, F_{β} and mechanical properties of membranes prepared with various casting conditions	97
Table 7-1. Comparison between dope and membrane inorganic loading	103
Table 7-2. F_{β} of membranes.....	105
Table 7-3. Membrane porosity, overall and skin thickness determined by SEM cross section measurement and average pore size determined by SEM surface measurement.	111
Table 7-4. Mechanical properties of membranes	117

Table 7-5. Initial bubble point and corresponding maximum pore size of membranes
..... 118

List of abbreviations

Al ₂ O ₃	Aluminium oxide
BSA	Bovine serum albumin
CaCl ₂	Calcium chloride
CNF	Carbon nanofibers
CNT	Carbon nanotubes
DBP	Dibutyl phthalate
DCMD	Direct contact membrane distillation
DMAc	N,N-dimethylacetamide
DMF	N,N-dimethylformamide
DMP	Dimethyl phthalate
EDS	Energy Dispersive Spectroscopy
EG	Ethylene glycol
FESEM	Field Emission Scanning Electron microscope
FTIR	Fourier-transform infrared
LOI	Loss on ignition
MD	Membrane distillation
MF	Microfiltration
MFI	Modified fouling index
MMT	Montmorillonite
MWCNT	Multi-walled nanotubes
NaCl	Sodium chloride
NF	Nanofiltration
NIPS	Non-solvent induced phase separation
NMP	1-methyl-2-pyrrolidinone
NOM	Natural organic matters
PE	Polyethylene
PEG	Poly(ethylene glycol)
PMMA	Poly(methyl methacrylate)
PP	Polypropylene
PSf	Polysulfone
PTFE	Polytetrafluoroethylene
PVC	Poly(vinyl chloride)
PVDF	Poly(vinylidene fluoride)
PVP	Poly(vinyl pyrrolidone)
RO	Reverse Osmosis
SAXS	Small angle X-ray scattering
SBA-15	Santa Barbara Amorphous No. 15
SEM	Scanning electron microscopy
SiO ₂	Silicon dioxide
SWCNT	Single-walled nanotubes
TEM	Transmission electron microscopy
TGA	Thermogravimetric analysis
THF	Tetrahydrofuran
TiO ₂	Titanium dioxide
TIPS	Thermally induced phase separation
TMP	Trans-membrane pressure
UF	Ultrafiltration
VIPS	Vapour induced phase separation
WAXD	Wide angle X-ray diffraction
XRD	X-ray powder diffraction.
XRD	X-ray powder diffraction
ZrO ₂	Zirconium dioxide

1. Introduction

1.1. The water issue and role of membrane technology

Water is becoming scarcer due to droughts brought on by climate change, as well as increased pressures on water sources due to increased urbanization and population growth. Water is essential for human life and culture, and is thus a critical resource for our sustainable future. To address the shortages and ensure water security, there is a rapid rise in the demand for new sources (e.g. sea and groundwater desalination) and the use of recycled water to replace more valuable potable water. A key technology in our ability to access new water sources is membranes [1].

The development of membrane technology has occurred over 150 years [2, 3]. It started as a research interest with limited large scale applications. A key milestone for this technology was the development of a reverse osmosis (RO) membrane in the late 1950s [4, 5] using cellulose acetate, which showed high salt rejection and high fluxes and thus was promising for membrane seawater desalination process. RO technologies have been commercialized since 1964 [6]. With continual development of other membrane materials, large scale application of membrane filtration to produce high-quality drinking water commenced in the mid-1980s. The first large scale use of microfiltration/ultrafiltration plant was established in Saratoga, CA, USA in 1993 with a capacity of 3.6 million gallons per day [7].

The most common applications include producing valuable water from seawater and brackish water (desalination), as well as treating industrial wastewaters (desalination and filtration). Membrane systems are used to replace procedures such as secondary sedimentation, flocculation, settling tanks, and granular filtration [8] that are usually found in conventional water treatment plants. One of the major advantages of incorporating a membrane system is that a reduced amount of chemicals that are used in the treatment process. Membrane systems also have smaller footprint and consistently produce high quality water. The ability to rapidly and continuously remove salt, contaminants and pathogens makes membrane technology attractive [9].

The general classification of membrane types in order of decreasing pore size is microfiltration (MF), ultrafiltration (UF), nanofiltration (NF) and RO. MF and UF membranes are used as an advanced water treatment process for removing particles including silt and pathogens [9], while RO and NF are typical processes for desalination of saline water (e.g. seawater). Figure 1-1 summarizes the application range of the typical membrane processes. The operating pressure for each membrane application

is generally based on the pore size of the membranes; typically low pressure range of for MF and UF (1-2 bar and 2-10 bar) and higher pressure required for NF and RO (7-14 bar and 10-70 bar) [9].

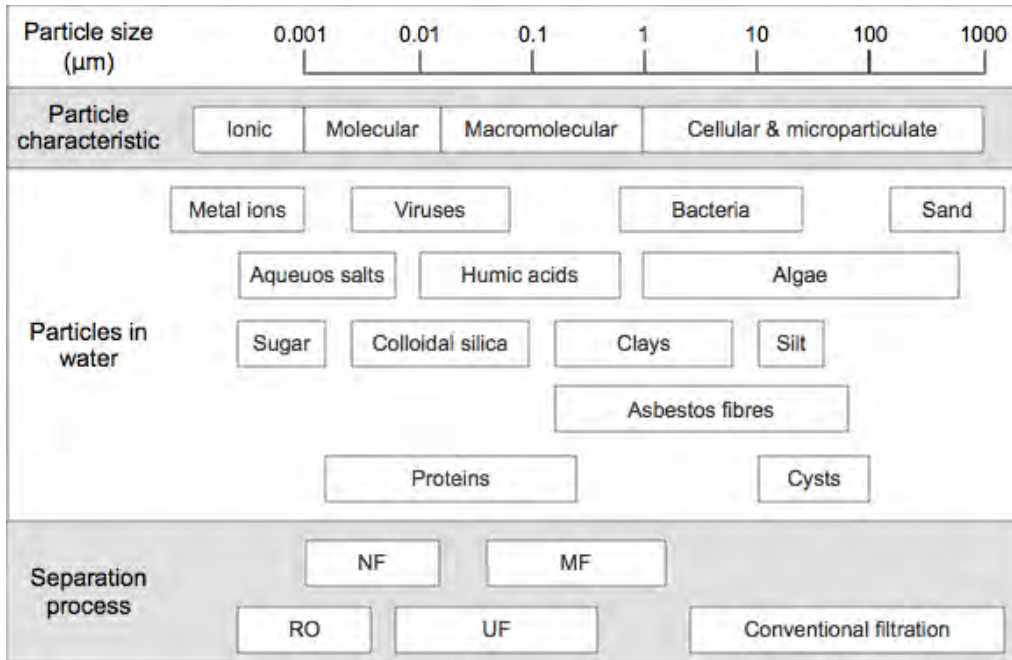


Figure 1-1. Typical membrane processes and applications (redrawn from [9]).

Membranes can be made of polymers, inorganic materials (ceramic, carbon or metal) or composites of these materials [10]. The most commonly considered for water treatment are polymeric and ceramic. Commonly used materials for ceramic membranes include aluminium oxide (Al_2O_3), titanium dioxide (TiO_2), zirconium dioxide (ZrO_2), silicon dioxide (SiO_2), or their combinations, to achieve the desired filtration mode and performance [11] and can carry out MF and UF. Ceramic membranes show better performance than polymer membranes in applications that require superior physical, chemical and thermal stability [12]. However, ceramic membranes are generally more expensive, brittle and difficult to produce [13]. Polymeric membranes, are lower cost, and flexible, and are widely adopted in the water industry. They usually come in the format of flat sheet or hollow fibre, where hollow fibre is the most popular membrane format for water treatment applications.

Despite the success of polymer membranes in treating waters today, the conventional polymeric materials is limiting them from their ability to treat waters that are major contributors to membrane fouling or require a higher physical durability [1]. Addressing these issues are essential for the growth of membrane applications and its

future development. One avenue that can be considered is a composite membrane material, which combines the physical durability of ceramics with the low cost virtues of polymers.

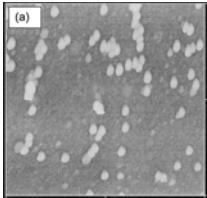
1.2. Current performance issues

1.2.1 Membrane fouling

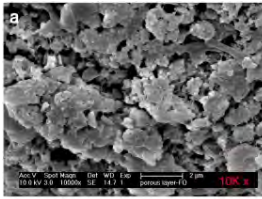
Membrane fouling is one of the major problems encountered in the water industry. Fouling hinders the flux of clean water through the membrane [14] which leads to an increase in feed pressure and requires frequent cleaning of membranes. Other than that, membrane life is also reduced due to biological growth, physical pore blocking and polymer degradation. With established membrane processes today, a portion of the fouling can be reversed by flow management including backwashing and flow relaxation. Additional cleaning protocols such as air scouring and chemical cleaning are also implemented to control fouling. Although these are quite effective in practice, there is an irreversible component which eventually requires membranes to be replaced.

Fouling may be caused by one or more of the following: particulate deposition, adsorption of organic molecules, inorganic deposits as well as microbial adhesion and growth [9]. The foulants, mechanism and the mitigation of each type of fouling are summarised in Table 1-1.

Table 1-1. Properties of various fouling types [9, 15, 16].

Fouling type	Foulants	Mechanism	Mitigation
Particulate deposition  (Reprinted with permission from [17], copyright (2001) Elsevier)	Inorganic particles and colloids from weathering of rocks (e.g. silts and clays).	Deposition of particles and colloids forms cake layer on top of membrane which become compressed and reduce flux.	Backwashing or air scrubbing is often effective to remove the cake.

Organic fouling



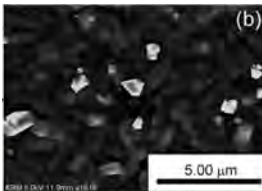
(Reprinted with permission from [18], copyright (2013) Elsevier)

Natural organic matters (NOM) including humic acids, fulvic acids, proteins, amino sugars, polysaccharides, polyoxyaromatics.

Negative charged foulants have an affinity for charged membrane surface which forms layer reducing flux and salt rejection.

Chemical cleaning with caustic and/or chlorine is used to control organic fouling.

Inorganic fouling



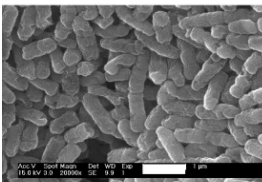
(Reprinted with permission from [19], copyright (2013) Elsevier)

Inorganic precipitates such as metal hydroxides

Accumulation of inorganic precipitates causes scaling on membrane surface or within pore structure.

Cleaning with acids and chelating agents can remove scales and metal dioxides from fouling layers.

Biofouling



(Reprinted with permission from [20], copyright (2007) Elsevier)

Microorganism including bacteria, algae and fungi

Microbial activities lead to formation of biofilms on the membrane.

Biofouling is commonly controlled using chlorine (including chloramine) and biocide cleans.

Organic fouling caused by NOM may be viewed as the most challenging type to mitigate due to the complexity and varied composition of NOM. To simulate a fouling environment in laboratory scale, model foulant solutions made up by bovine serum albumin (BSA) and sodium alginate have been used. These represent the predominant organic foulants proteins and polysaccharides respectively [21]. Biofouling and particle deposition are also major fouling types [9] but are harder to

replicate in a laboratory environment; although model foulant testing may give some indication of biofouling as it involves proteins and polysaccharides as well.

Membrane fouling remains a major challenge to overcome for the water industry due to its complex mechanism and varieties. Besides conventional mitigation methods like backwashing and chemical cleaning, there has been some interest in improving low pressure membrane anti-fouling performance by incorporating nanoparticles into the membranes [22-27]. While progress into anti-fouling properties has been made via nanoparticles, it is also important to explore current research aiming to improve physical durability.

1.2.2 Physical durability

Conventionally, pretreatment of seawater is achieved via coagulation/flocculation followed by granular media or dual media filtration. Such pre-treatment is necessary to remove particles, silt, colloids and micro-organisms before the water is treated by RO so as to reduce fouling on the RO membranes. Recently pretreatment with low pressure MF and UF membranes has become more popular and seawater desalination plants that have adopted UF pretreatment include those in Adelaide (Australia), Perth (Australia), Yu-Huan (China), Fukuoka (Japan), Saudi Arabia and Turkey [28]. Filtration by MF or UF removes a wider spectrum of particles [29] than conventional coagulation/filtration and the improved water quality subsequently reduces RO fouling and cleaning frequency. Other than having smaller plant footprint size which reduces capital investment [30], MF/UF pretreatment uses fewer chemicals compared to coagulation and flocculation ahead of dual media filtration [31].

While these benefits and the technical and economic feasibility of MF/UF pretreatment have been demonstrated in field studies [30, 32, 33], conventional granular media filtration still remains the pretreatment process for medium and large size desalination plants. One reason for this is the shortened lifespan of MF/UF membranes treating seawater compared to wastewaters and surface waters. Lifetimes of only 3-5 years are achieved for seawater applications [34] compared to 7-10 years for water and wastewater applications [35]. This shorter life expectancy is likely to be related to the harsher condition provided by the water source. Surface water and wastewater contain bio/organic particles, while harder and more abrasive particles including sand and silica based debris are present in seawater [36]. This discrepancy in contaminant characteristics between water sources is likely to be the reason for the

shorter life expectancy of polymer MF/UF membranes in seawater, and is supported by an autopsy of RO membranes that identified abrasion with biofouling as the leading cause (28%) [37]. Figure 1-2 shows membrane surface damage caused by sand particle abrasion. Further, the quality of the seawater fed to a desalination plant is subject to the location of the intake. In general, MF and UF pretreatment are associated with cleaner seawaters taken from costly deep offshore intakes, and avoiding the poorer water qualities associated with shallow, near shore intakes [38, 39]. MF/UF filtration membranes with stronger abrasion resistance may relax the costly need for deeper offshore intakes and/or offer more options to the types of water suitable for desalination plants with MF/UF pretreatment.

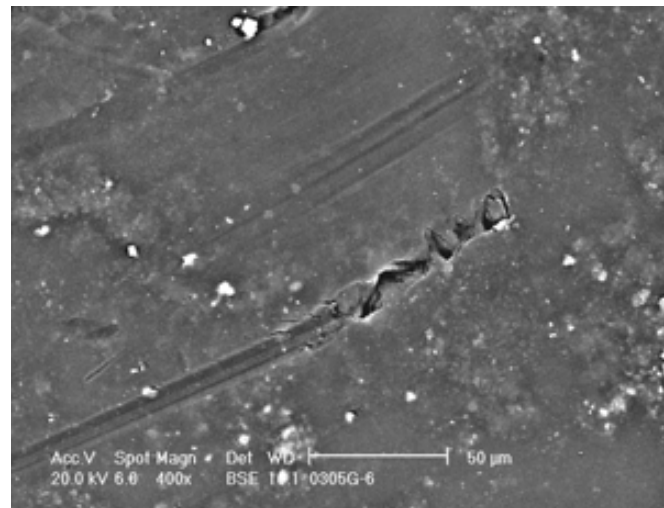


Figure 1-2. Sand particle abrasion (reprinted with permission from [37], copyright (2011) Genesys).

Microscreening with mesh size of 120 μm or less is currently installed ahead of the membranes [38] to prevent damage from shells and other abrasive particles in seawater. This increases both the capital and running costs, and abrasive particles smaller than the screen mesh size, such as clay/silt aggregates are in the range of 1-40 μm and that of phytoplankton ranges from 4 to 120 μm [40], still can accelerate the wear of membranes. Additionally, some algae and diatoms with exoskeletons made of silicon or calcite are less than 5 μm in size [37] and have low removal efficiencies by screening. Therefore increased abrasion from seawaters appears unavoidable and improved physical endurance of the MF/UF membranes is required to improve their in service life.

Other than abrasive wear, fibre breakage is another durability issue for MF/UF membranes which leads to loss of membrane integrity. Fibre breakage can be attributed to membrane stress and strain from operating conditions, including backwashing or excessive movement owing to vigorous bubbling [41]. Study on commercial membranes based on data obtained from the literature, membrane manufacturers and water treatment plants showed that the annual fibre failure rate was between 1 to 10 per million fibres [42]. Although this failure rate was acceptable based on the overall satisfactory microbiological filtration performance, further reducing this rate can lower replacement costs and down-time. To reduce fibre breakage, one of the keys is to improve the mechanical properties including tensile strength and stiffness of the membrane materials [42, 43].

There has been little published work focused on improving MF/UF physical durability, but nanocomposite inorganic/polymer materials are known to have improved physical performance over polymers [44] and fabrication of nanocomposite MF/UF membranes may be a means to achieve greater service lifetimes.

1.3. Polymer composite and nanocomposite

In order to gain the specialised benefits of both organic and inorganic materials, inorganic materials can be included into the polymer matrix. Fillers in the micrometre scale, including calcium carbonate, glass beads and talc, are commonly used in conventional polymer composites that are commercially available. By modifying their volume fraction, shape and size, various mechanical properties of the composite materials are enhanced [45]. Composites incorporating short glass fibres which have a high aspect ratio (ratio of length to thickness) have been reported to improve mechanical performance such as fatigue strength and tensile strength [46, 47]. More recently, fillers including layered silicates and carbon nanotubes (CNT) have demonstrated similar mechanical improvement with considerably lower loading given their large aspect ratio at the nanometre scale [45].

These nanofillers can be incorporated into membranes producing a new class of membranes known as nanocomposite membranes. They are receiving increasing attention worldwide including from the water treatment industry. Polymer membranes incorporated with TiO₂ were often reported with increased hydrophilicity and improved antifouling behaviour [23, 48]. As for silver nanoparticles, Lee *et al* [49] utilised them

as a biocide to inhibit microbial fouling on polyamide membranes, with results demonstrating a substantial anti-fouling property borne from the inclusion of the silver nanoparticles. The mechanical enhancement observed in conventional composite materials also has great potential in increasing the robustness of MF and UF membranes.

Given the wide varieties of nanofillers available and their abilities to enhance different properties, careful selection of suitable nanofillers and exploring how nanocomposites are developed for membranes could possibly improve the durability of low pressure filtration membranes.

1.4. Summary and research scope

Polymer membranes are widely utilised in water treatment due to their low cost, availability, ease of manufacture and high performance. However further applications, such as sea water pretreatment, limit their life due to fouling and physical degradation. Nanocomposite materials are widely explored for anti-fouling properties, showing positive results. Since nanocomposites have also exhibited superior physical durability in other industries, the issue of physical durability could also be addressed but so far there is little research on this topic. Therefore, the scope of this research is to:

- Assess various nanofillers for production of nanocomposite membranes.
- Demonstrate if the improved physical durability observed in composite materials can be translated to practical benefit in membranes for water treatment.
- Explore the mechanisms of abrasive wear and how the more durable materials provide resistance.

2. Literature review

2.1. Introduction

Nanocomposite membranes with inorganic/organic hybrid materials are potential solutions to current performance issues including physical durability and membrane fouling in low pressure filtration membranes. Exploring the nanocomposite materials for application to durable membrane filtration requires an understanding of the current knowledge in polymer membrane fabrication that leads to their functional properties in separation and water productivity. The state of the art in literature on nanocomposites on physical durability and theory proposed for abrasive wear were also reviewed.

2.2. Polymeric membranes

At the same time as improving durability of polymer materials to be applied as water treatment membranes, the material must also have the correct pore size to enable it to function as a membrane. This section reviews the most common materials used in polymeric membranes for water treatment, their key properties and the fabrication process that have been proven to give the desired properties.

2.2.1 Membrane materials

Typical polymers used for low pressure membranes in the water industry include polypropylene (PP), polytetrafluoroethylene (PTFE), polysulfone (PSf) and poly(vinylidene fluoride) (PVDF) [50, 51].

PP membranes are prepared by stretching and phase inversion and can be used for MF and membrane distillation (MD). They have good chemical resistance and mechanical strength but are not oxidant tolerant [52].

PTFE is highly crystalline with outstanding thermal and chemical properties [50]. It can be used as membrane materials for MF, UF and MD and the membranes are usually prepared by sintering and stretching [9, 50].

PSf has excellent chemical resistance, thermal stability and a wide pH tolerance [52]. It can be fabricated as UF membrane or used a support material for composite membranes [50].

PVDF is another popular UF material among membrane manufactures. PVDF plays an important role in various industries, such as pulp and paper, nuclear-waste

processing and chemical processing [53], owing to its remarkable chemical and physical properties. Its strong chemical resistance against corrosive chemicals including acids, bases, oxidants and halogens [54] makes it an excellent polymeric membrane material and popular among various research groups. As membranes, it is the most widely used in water treatment for the same reasons but in a hydrophilic form, and also has the ability to be controllably porous for MF and UF application. Therefore efforts to improve durability on PVDF membranes are likely to reach in to many more water treatment applications.

2.2.2 Membrane fabrication

Membranes are made from a range of processes depending on the polymer type. These techniques include sintering, stretching, track-etching, template leaching, phase inversion and coating [50, 55]. As PVDF is the most popular material in MF and UF water treatment applications, opportunities to improve its physical properties ties back to membrane fabrication processes. PVDF MF and UF membranes are commonly prepared by phase inversion [9, 56], and the most common technique for commercial fabrication of MF/UF membranes.

2.2.2.1 *Phase inversion*

Phase inversion is also known as phase separation and polymer precipitation. During the phase inversion process, a one-phase liquid polymer solution changes into two separate phases, which includes a polymer-rich solid phase that forms the membrane structure and a polymer-poor liquid phase that attributes to the membrane pores [57]. There are a number of phase inversion processes, namely (1) thermally induced phase separation (TIPS), (2) solvent evaporation, (3) vapour induced phase separation (VIPS) and (4) non-solvent induced phase separation (NIPS) or immersion precipitation.

2.2.2.1.1 Thermally induced phase separation (TIPS)

Fabrication of microporous membranes via TIPS was first employed and commercialized by Akzo in 1980s [58]. This method is common for fabricating PP and polyethylene (PE) membrane and has become more popular for PVDF membrane fabrication in recent years [59, 60]. In the TIPS process, the polymer is dissolved in a

diluent with high boiling point and low molecular weight such as sulfolane and oil. The hot polymer solution is cast then cooled to allow precipitation to occur. The removal of thermal energy separates the casting solution into two phases followed by polymer crystallisation [59].

The choice of a diluent in TIPS can alter the crystallisation process via different degrees of polymer-diluent interaction and also changing the crystallisation temperature of the polymer [59, 61]. This subsequently changes the membrane morphology and other properties including pore size, flux and mechanical strength. For instance, using dibutyl phthalate (DBP) as diluent resulted in PVDF membrane with irregular fuzzy structures [62] while dimethyl phthalate (DMP) gave spherical semicrystalline structures [63].

The cooling rate during TIPS also impacts polymer crystallization. While increasing the cooling rate was shown to reduce the PVDF crystallization temperature and enhanced the crystallization [63], decreasing the cooling rate resulted in membrane with broader pore size distribution and weaker mechanical strength [64].

Despite the emerging importance of this technique, the shorter history of TIPS being commercialized makes it comparatively less well studied than NIPS.

2.2.2.1.2 Solvent evaporation

Solvent evaporation is one of the earliest techniques used for microporous membrane fabrication, having been used by researchers such as Ferry since the 1920s [65], and in recent years for filtration application [66]. In this technique, polymer is first dissolved in a volatile solvent and a less volatile non-solvent; the membrane is then cast onto a support surface. The dope is then placed under inert gas to avoid adsorbing water vapour during the evaporation process. As the volatile solvent is removed by evaporation, the ratio between the non-solvent and polymer in the dope increases. Eventually, the polymer precipitates and forms the membrane structure [50, 57].

The porosity of the membrane can be increased by increasing the non-solvent component in the dope or by reducing the polymer concentration [57]. Solvent evaporation is a relatively slow process and as a result membranes formed with solvent evaporation often have large pore size.

2.2.2.1.3 *Vapour induced phase separation (VIPS)*

VIPS was first used in 1918 by Zsigmondy [67] and it brings about membrane formation when the non-solvent in the vapour atmosphere diffuses into the cast solution [50]. When solvent of low volatility is used to make up the dope, the solvent evaporation rate is slower than the non-solvent absorption rate during the casting process. This brings about low polymer concentration in the area close to the film surface [68] which in turn contributes to a highly porous membrane surface which is beneficial to improving flux. With these features, VIPS is a suitable process for fabricating membranes for MF and MD as it is able to produce highly porous membranes with pore sizes in micron and sub-micron range [69].

2.2.2.1.4 *Non-solvent induced phase separation (NIPS)*

NIPS was first used by Sidney Loeb and Srinivasa Sourirajan to prepare cellulose acetate RO membranes in late 1950s [5]. For flat sheet membranes, the polymer is dissolved in a suitable solvent then cast onto a flat support layer with a defined thickness before immersing into a non-solvent bath for precipitation to produce flat sheet membranes. Flat sheet can be either hand cast by a doctor blade in lab scale (Figure 2-1(a)) or fabricated by automated casting machine (Figure 2-1(b)).

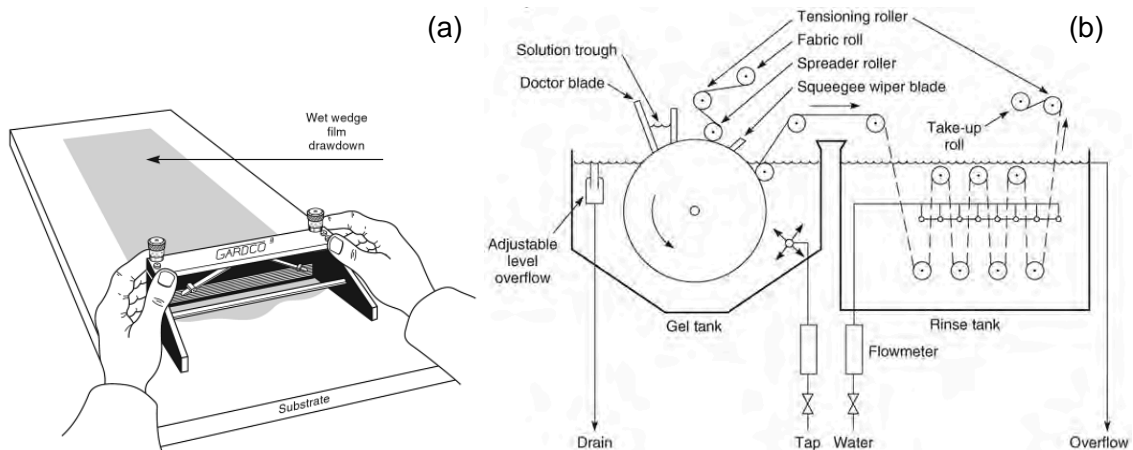


Figure 2-1. Flat sheet fabrication by hand casting (a) and membrane casting machine (b) (reprinted with permission from [70], copyright (2012) John Wiley & Sons).

In the case of hollow fibre membranes, they are fabricated by one of the following methods: wet spinning (or dry-wet spinning), melt spinning or dry spinning. Wet spinning (as shown in Figure 2-2) is the most common method, where the polymer solution is loaded into a spinneret with a bore fluid pumping through the inner tube.

The fibre is drawn from the spinneret before entering a quench (coagulation) bath for precipitation [50].

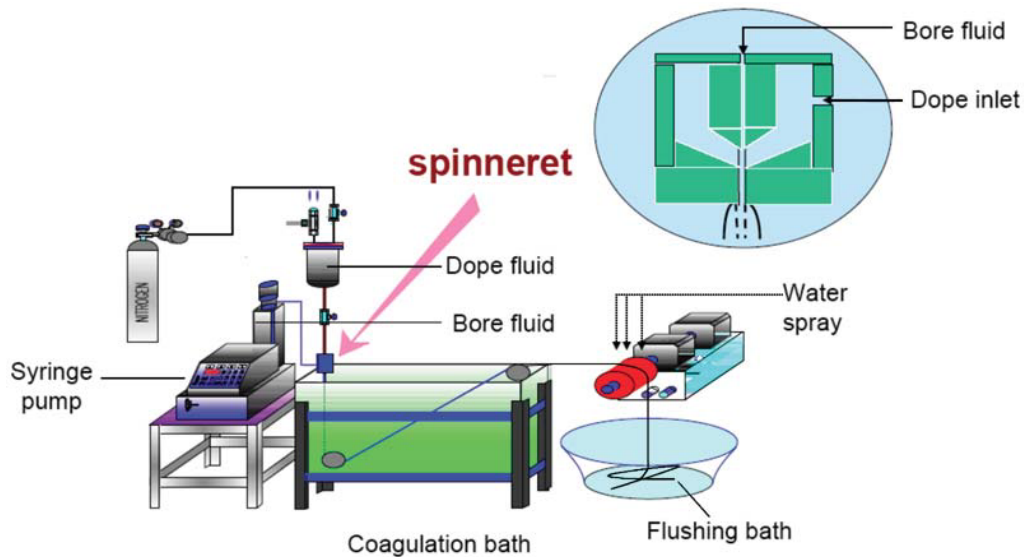


Figure 2-2. Schematic diagram of the wet spinning apparatus (reprinted with permission from [9], copyright (2006) Springer).

For the selected polymer, the solvent and the non-solvent have to be miscible with each other. As the cast dope makes contact with the non-solvent, the dope consisting of the polymer and the solvent demixes into two liquid phases which is known as liquid-liquid demixing [50]. Solvent begins to leave the casting solution while non-solvent moves into the dope. As this process progresses, the polymer solution becomes thermodynamically unstable and separates into two phases. The top surface is first precipitated to form a skin layer which acts as a barrier slowing the solvent/non-solvent exchange rate. This leads to increased average pore size as the precipitation takes longer to occur and results in a sponge-like layer [57]. Figure 2-3 shows a schematic drawing of a typical asymmetric flat sheet membrane cross-section. Finger-like voids, also known as macrovoids, are another feature that are often observed in membranes prepared with NIPS. They tend to occur in systems that show instant liquid-liquid demixing which is yet a favourable condition for formation of porous membranes [50]. Macrovoids in membranes are usually undesirable as they tend to weaken the mechanical structure and cause the membrane to be more prone to failure under high-pressure operation [71]. While the size/depth of macrovoids can be reduced by a number of methods such as increasing the dope viscosity [72] and addition of surfactants into the synthesis solution [73], other membrane properties can be altered

in the process and at such a balance needs to be taken. For semi-crystalline polymers, such as PVDF, the phase inversion process is more complicated as it can be driven not only by liquid-liquid demixing but also by crystallisation [59]. The two mechanisms give rise to different membrane morphology and properties.

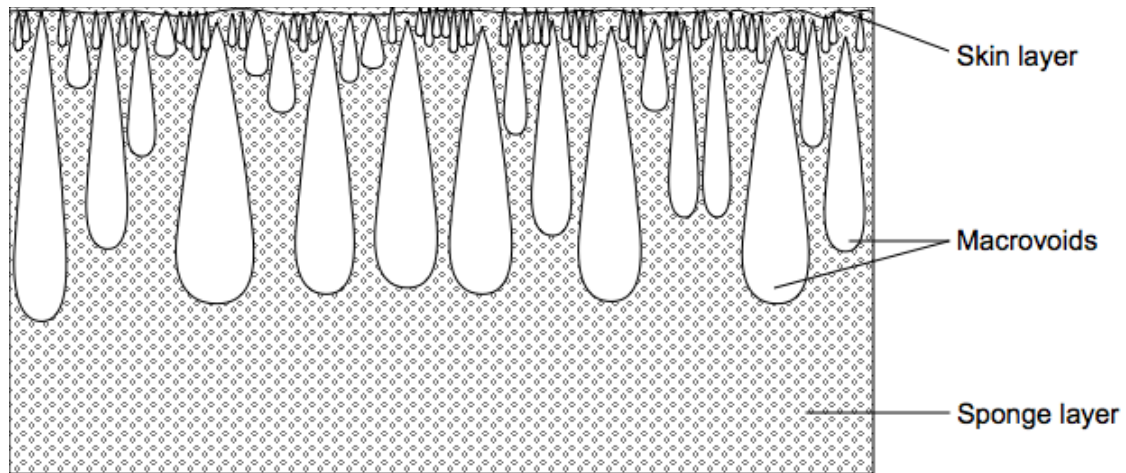


Figure 2-3. Schematic diagram of a typical asymmetric flat sheet membrane cross-section.

Other phase inversion processes can be incorporated with NIPS to control membrane properties. Varying the solvent evaporation time (air retention time) prior to NIPS can change the average pore size; shortening the evaporation time gives smaller pores and vice versa [57]. [50]. VIPS can be used prior NIPS during membrane fabrication by controlling humidity and the air retention time. Due to the gas phase mass transfer resistance, the non-solvent enters the casting film at a much slower rate compared to the NIPS process. This membrane formation mechanism leans towards crystallization rather than liquid-liquid demixing [74].

In summary, membranes can be fabricated by phase inversion through a number of processes including, TIPS, solvent evaporation, VIPS, and NIPS. The fabrication techniques highlight the steps needed to make high quality polymer membranes. These common methods of membrane fabrication can be utilised to produce membranes with increased durability. A technique considered to alter physical properties of membranes is to include inorganic materials within the polymers and produce composites. NIPS was selected in this study not only because it is the most common industrial method for MF and UF fabrication, but also it is a fast process with parameters that are easy to control [75].

2.2.2.2 *Conditions and parameters for controlling membranes made by NIPS*

There is a range of conditions and parameters associated with the casting process which influence the membrane physical dimensions and morphology. This leads to variation in membrane properties including pore size, mechanical strength, flux and selectivity.

2.2.2.2.1 Conditions to control membrane formation

The most common conditions used to control membrane formation are:

- Choice of solvent

The morphology of membrane is affected by the solvent solubility parameter and the mutual diffusivity between solvent and coagulant. Solvents with strong solvent power such as N,N-dimethylacetamide (DMAc), N,N-dimethylformamide (DMF) and 1-methyl-2-pyrrolidinone (NMP) often undergo rapid demixing process and result in porous membranes [57, 59].

- Polymer concentration and composition of dope

Increasing polymer concentration in dope tends to form a denser and less porous skin layer resulting in lower flux [50]. Additives in the dope can also change membrane morphology and performance as they affect pore formation, dope viscosity or the phase inversion rate [59]. Using polymeric additives such as poly(vinyl pyrrolidone) (PVP) and poly(ethylene glycol) (PEG) can form highly porous membranes and increase the membrane hydrophilicity [57]. The addition of surfactants in the casting dope can either enhance or suppress the formation of macrovoids, depending on the miscibility between the surfactant and the coagulant [73].

- Composition of the quench bath

A strong non-solvent such as water brings about rapid liquid-liquid demixing which results in asymmetric membrane structure with finger-like voids [59]. Using organic-based coagulants such as methanol or isopropanol delays the demixing process and form denser membranes with lower flux [57]. Multiple components can also be used in the coagulation bath to control the demixing parameters. For instance, adding NMP (a solvent for PVDF) into the water bath (a strong non-solvent for PVDF) delays the onset of liquid-liquid demixing [50]. Addition of an inorganic salt, such as sodium chloride

(NaCl), to the aqueous quench bath can also slow down the demixing and suppress the formation of macrovoids [76, 77].

- Temperature of the quench bath

Membranes produced with low bath temperature tend to exhibit lower flux and smaller pore size [57]. The bath temperature also affects the morphology and crystallinity of membranes. At low temperature (15-20°C), the PVDF membrane undergoes crystallisation-dominated precipitation which results in symmetric structure with spherical crystallites. At high temperature (60-65°C), liquid-liquid demixing occurs and the membrane has an asymmetric morphology with skin and sponge layer with finger-like voids [78-80].

- Humidity

For flat sheet membranes, the dope is exposed to air after it is cast onto a support surface. And for hollow fibres, the dope has contact with air in the air gap, which is the space between the spinneret and the coagulation bath. Atmospheric humidity in the casting environment has effect on membrane properties as water vapour presents in air reacts with the dope. At high humidity with increased water vapour pressure, water vapour can induce early precipitation and increase the membrane skin thickness [81]. Larger surface pore size which resulted in higher water flux but lower BSA retention was also observed [82].

2.2.2.2.2 Parameters for membrane production

The effect of these conditions has been translated to control parameters typical for flat sheet and hollow fibre membrane production respectively. These are summarised in Table 2-1.

Table 2-1. Typical parameters used to control production of flat sheet and hollow fibre membrane casting.

Flat sheet membrane	Hollow fibre membrane
<ul style="list-style-type: none"> • Air retention time After casting onto a rigid flat support material (e.g. glass plate), the dope can be exposed in air for a defined time before precipitation. During this time, water vapour in air starts the phase separation process (refer Section 2.2.2.1.3) and solvent evaporation can occur if it is volatile (e.g. tetrahydrofuran (THF) and acetone). PVDF and PVDF/nanoclay membranes with longer retention time in air before immersing to coagulation bath were observed to have increased finger-like macrovoids [83]. 	<ul style="list-style-type: none"> • Distance of air gap Varying the distance of the air gap affects the formation of the outer skin of the membrane [59]. Reducing air gap tends to increase the water permeability of PVDF hollow fibre [84, 85]. By increasing air gap distance, membrane with thinner and denser sponge layer was formed [84]. • Extrusion rate of dope The extrusion rate of the dope affects the membrane dimensions including the outer diameter and the wall thickness. Increased extrusion rate is also associated with an increase in water permeability of membrane [59].

Despite these few parameters for controlling flat sheet and hollow fibre casting, both formats are similar in chemistry and have common effects of operating properties such as dope composition and coagulation bath conditions. As such, it would be reasonable to use flat sheet as preliminary study given its relatively simpler setup then proceed to hollow fibre fabrication and characterization. Taking this approach allows for rapid exploration of the effect of various production conditions on membrane morphology and performance. Hollow fibre production is more complex, where specialist facilities are operated using proprietary techniques by membrane companies. However as commercial membranes in water treatment are produced on hollow fibres, the conditions verified on flat sheets need to be confirmed on hollow fibres. A number of conditions and parameters for controlling membranes made by NIPS were evaluated. However how these conditions influence the inclusion of nanoparticles is unknown.

2.3. PVDF nanocomposites

2.3.1 PVDF

The key durability issues to be improved would be viable through the popular and versatile PVDF as a nanocomposite. However as mentioned in Section 2.2.2.1.4, PVDF as a crystalline polymer can add a degree of complexity to the fabrication process and its various crystalline phases often associate with changes in material properties that must be explored. Then the properties of the nanofiller also need to be explored.

2.3.1.1 PVDF crystalline phases

Among the five phases of PVDF, namely α , β , γ , δ and ϵ [54], α - and β -phase are the most reported in the literature [86]. While α -phase is kinetically favourable owing to a trans-gauche configuration, β -phase has all-trans conformation which is the most thermodynamically stable form (Figure 2-4) [87]. β -phase also exhibits the most activity for piezo/pyroelectric properties [88, 89] which is good for electromechanical and electroacoustic transducer applications. Furthermore, previous studies [53, 90] have identified that shifting from α -phase to β -phase is related to an improvement in abrasion resistance and mechanical properties such as stiffness and toughness in nanocomposite materials. As the β -phase has these attractive properties, studies were carried out to investigate ways to shifting PVDF crystalline phase from α to β . Particularly for membranes, these methods include: incorporating nanoparticles such as CNT [56]; decreasing the temperature of the coagulation bath [91] and changing the coagulation bath medium from water to C1-C8 alcohols [86].

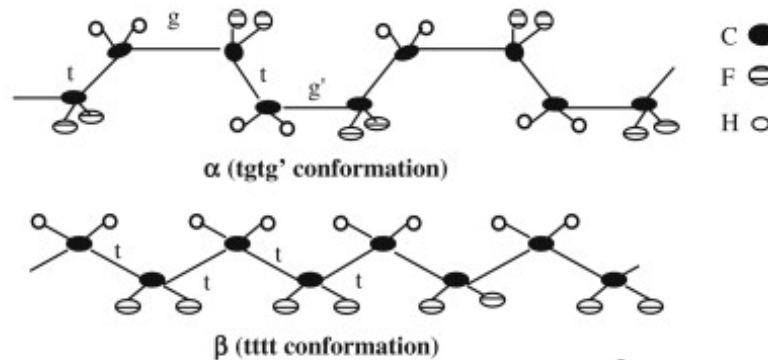


Figure 2-4. Conformation of PVDF α - and β -phase.. Black, white and striped spheres denote carbon, hydrogen and fluorine atoms respectively. (Reprinted with permission from [92], copyright (2009) Elsevier).

2.3.2 Nanofillers

2.3.2.1 *Nanoparticles*

Inorganic nanoparticles such as Al_2O_3 , TiO_2 , ZrO_2 and SiO_2 can be used for reinforcing or toughening polymeric materials [45]. Recently, these particles were incorporated into PVDF membranes and the effect on membrane properties including mechanical enhancement, hydraulic performance and fouling resistance was evaluated.

2.3.2.1.1 *Mechanical enhancement*

PVDF membrane incorporated with 40 wt% of TiO_2 was tested for mechanical resistance for the use in vapour permeation processes. It demonstrated stronger resistance to compaction than pure PVDF membrane under pressure of 30 bar as shown from the decrease of pore volume percentage of 17% compared to 83% [93].

Nanoparticles also have potential for improving membrane mechanical properties in UF applications shown by tensile testing. In particular, PVDF flat sheet membrane with 0.54 wt% of Santa Barbara Amorphous No. 15 (SBA-15) (a mesoporous silica material with a highly ordered 2D hexagonal mesostructure and thick uniform silica walls) increased tensile strength from 0.151 MPa to 0.183 MPa while that loaded with 0.36 wt% increased elongation-at-break from 22.6% to 49.4% [22]. This showed that both stiffness and ductility of the nanocomposite membrane were improved. PVDF/ TiO_2 hollow fibre membranes prepared by either TiO_2 sol-gel or blending method showed 30% increase in tensile strength [26]. However, elongation at break decreased from 162% to 120% likely due to the rigidity of the inorganic particles. Han *et al* [94] explored the effect of using multiple types of nanoparticles (TiO_2 , SiO_2 and Al_2O_3) in PVDF hollow fibre membranes. It was noted that all nanocomposite membranes had higher tensile strength, and the best improvement was from 1.71 MPa to 3.74 MPa with a combination of 2 wt% TiO_2 and 1 wt% Al_2O_3 . The improvement could be attributed to the reduced macrovoid formation observed in the nanocomposite membranes. Yet, ductility of the composite membranes was reduced compared to the neat PVDF membrane. The authors suggested the decrease was due to the brittleness of the particles compared to the more flexible polymer chain. However, the decreased ductility could be owing to the increased cross-linking arising from the nanoparticle inclusion rather than the brittleness of the particles, as the loads used for the tensile

testing are of a magnitude likely to break the polymer-nanoparticle bonds but not the particles themselves.

On a side note, the nanoparticle loadings appeared to have large variation as they were of different applications. For instance, the 40 wt% of TiO₂ (by weight of PVDF) was for mechanical support in vapour permeation process while the combination of 2 wt% TiO₂ and 1 wt% Al₂O₃ (by weight of dope) was used for ultrafiltration. Rather for direct comparison between these membranes, this section demonstrated nanoparticles can be used to improve membrane physical strength.

2.3.2.1.2 Hydraulic performance

Increase in water flux has been observed with PVDF membranes incorporated with TiO₂ [26, 94, 95], SiO₂ [25, 96] and SBA-15 [22]. This was associated with change in hydrophilicity, surface pore size and porosity. Hydrophilicity of the PVDF material was reported to be associated with its crystalline phase and polarity [97]. PVDF/SiO₂ hollow fibre membranes prepared by Yu *et al* [25] showed the PVDF β -phase crystallinity was directly proportional to the membrane hydrophilicity as measured by X-ray power diffraction (XRD) and contact angle respectively. The greater hydrophilicity was one of the reasons for increased in water permeability. Composite membranes also demonstrated better rejection rates in waste water treatment [22, 95]. Here, the PVDF composite membrane with 1.95% of TiO₂ (by weight of dope) tested with oil refinery wastewater showed 99% rejection compared to 63% by neat PVDF membrane [95]. It was likely because of the more hydrophilic membrane surface which repelled the oily components in the wastewater.

2.3.2.1.3 Fouling resistance

Neat PVDF and PVDF/TiO₂ (2 wt% in dope) membranes were tested with 100 ppm of casein at constant pressure [23]. The composite membrane had a lower modified fouling index (MFI) which showed that TiO₂ improved membrane fouling resistance. Indicated by decrease in the ratio of permeate flux decline (flux ratio from start of filtration with foulant solution to stable permeate flux), various kinds of nanoparticles including SBA-15 [22], SiO₂ [25] and TiO₂ [26] had the potential to improve the anti-fouling properties of PVDF membranes. Again, the improved fouling resistance was likely related to the higher hydrophilicity influenced by the crystalline phase [25, 26].

Although nanoparticles have shown potential to reduce fouling, the fouling tests in the reviewed studies were conducted by measuring flux decline with constant pressure applied. These were different from real operating conditions which use constant flux with variable pressure. Also, backwashing was not implemented which is essential to distinguish between reversible and irreversible fouling. As such, testing with periodic backwashing and constant flux measuring the trans-membrane pressure is needed to provide a more realistic fouling study.

2.3.2.2 CNT

CNT are allotropes of carbon with cylindrical shape and they can be classified into single-walled nanotubes (SWCNT), multi-walled nanotubes (MWCNT) and carbon nanofibers (CNF) [45]. CNT often have excellent strain to failure and stiffness, making them good reinforcement for polymers. PVDF/MWNTs nanocomposites prepared with solvent evaporation have shown higher tensile strength and Young's modulus [98, 99].

In the membrane context, Mago *et al* [56] prepared PVDF nanocomposites membranes by NIPS with ethanol or water as the non-solvents. 5 wt% MWCNT were used in this study. The addition of MWCNT and the use of ethanol as the non-solvent increased β -phase crystallization of the PVDF. In contrast, without incorporating MWCNT or using water as the non-solvent resulted in crystallization of the PVDF mainly in the α -phase.

Compared to other types of nanofillers, the effect of CNT on PVDF membrane properties has not been widely explored. Despite increased β -phase crystallization and improved mechanical properties, the ability of CNT solving current durability issues including abrasive wear and fouling is still unknown. However CNT are costly and lower cost nanofillers such as nanoclays, may be more viable for improved membrane properties.

2.3.2.3 Nanoclay

Nanoclay, which is of relatively low cost and commercially available [45], has been widely investigated as a nanofiller for nanocomposite materials which have enhanced mechanical properties [53, 100-103] and abrasion resistance [90, 104, 105] in uses including engineering applications, car manufacturing and food packaging industries. These improvements are associated with nanoclay acting as a reinforcing agent as well as changing the PVDF crystalline phase [53, 90]. Nanoclay has a layered silicate

structure as show in Figure 2-5, where its thickness is about 1 nm while its width and length can be up to hundreds of nm [106]. Without modification, nanoclays, such as montmorillonite (MMT), have hydrophilic properties. In order to increase its compatibility with the polymeric material, it is often modified with organic surfactants. The inorganic nanoclay has a general formula $(\text{Na,Ca})_{0.33}(\text{Al,Mg})_2(\text{Si}_4\text{O}_{10})(\text{OH})_2 \cdot n\text{H}_2\text{O}$. Examples of modified nanoclay are Cloisite[®] 30B (Southern Clay Products) modified with 30 wt% methyl dihydroxyethyl tallow ammonium and Nanomer[®] I.44P (Nanocor) modified with 35-45 wt% dimethyl dialkyl(C14-C18).

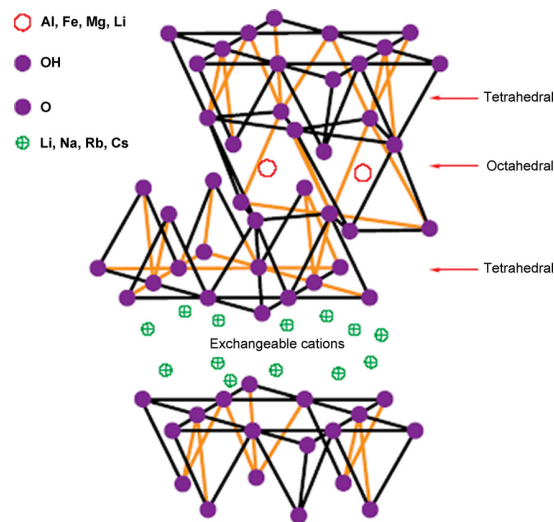


Figure 2-5. The structure of 2:1 layered silicate (reprinted with permission from [106], copyright (2002) Elsevier).

2.3.2.3.1 *Mechanical enhancement*

The addition of nanoclay changed the mechanism of PVDF nucleation and promoted the shift to β -phase in the PVDF matrix [107]. Shah *et al* [53] proposed that this change was linked to the mechanical enhancement in PVDF/nanoclay composites. Commercially available unmodified sodium montmorillonite (NCMU) and bis(hydroxyethyl) methyltallowammonium ion-exchanged montmorillonite (NCM) nanoclays were dispersed within PVDF to 5 wt% in a high energy mixer and melt extruded at 200°C. For the PVDF/NCM material, tensile tests showed that the Young's modulus increased from 1.3 to 1.8 GPa and the elongation at break increased from 20% to 140%. This inferred significant increase in toughness of ~700% higher than pure PVDF material. The authors suggested that nucleation of the fibre-like PVDF β -phase on the faces of individual silicate layers of the nanoclay brings about a structure

which is more favourable to plastic flow under applied stress. This results in a more efficient energy-dissipation mechanism in the nanocomposites to delay cracking.

As membranes, PVDF/nanoclay nanocomposite materials also demonstrated improved mechanical properties [83, 108]. Among four different types of nanoclays (Cloisite[®] Na⁺ (unmodified clay), Cloisite[®] 15A (modified with 43 wt.% dimethyl, dehydrogenated tallow, quaternary ammonium), Cloisite[®] 20A (modified with 38% dimethyl, dehydrogenated tallow, quaternary ammonium), and Cloisite[®] 30B (modified with 30 wt.% methyl dihydroxyethyl tallow ammonium)), maximum tensile strength was observed for the flat sheet membrane with 1 wt% of Cloisite[®] 15A prepared with an air exposure time of 30 s before immersion into a water bath. The likely reason was because Cloisite[®] 15A had the highest hydrophobicity which gave good affinity to the PVDF matrix [83].

Wang *et al* [108] studied the effect of adding Cloisite[®] 20A into PVDF hollow fibre for direct contact membrane distillation (DCMD) applications. Cloisite[®] 20A was mixed with PVDF in NMP and ethylene glycol (EG) and the membranes were fabricated using the dry-jet wet phase inversion mechanism by using water as both internal and external coagulants. The ratio of dope was PVDF/NMP/Cloisite[®] 20A/EG (10.0/74.7/3.3/12.0). The PVDF/20A membranes had lower ductility (extension at break) and stretch resistance (tensile stress), but increased stiffness (Young's modulus) compared to the unmodified membranes. Unlike neat PVDF fibres which collapsed under long operation time, nanocomposite membrane was able to withstand the desalination test over 220 hours with stable vapour flux. This study also showed the inclusion of clay particles enhanced long-term mechanical stability.

2.3.2.3.2 Abrasion resistance

Peng *et al* [90] studied the tribological properties, including the abrasive wear resistance, of PVDF/nanoclay nanocomposite. 1-5 wt% of Nanomer[®] I34TCN (modified with 25-30 wt.% methyl dihydroxyethyl hydrogenated tallow ammonium) was melt extruded with PVDF at 190°C, 180 rpm. It was observed that low nanoclay loading (1-2 wt%) had the highest ductility and impact strength as nanoclay can act as a temporary crosslinker to the polymer chains given their size and mobility are comparable. This provides localized regions of increased strength and inhibits the development of cracks and cavities. Nanocomposite at low nanoclay loading also had the lowest friction coefficient and wear rate. The author postulated that the shifting of the PVDF crystal phase induced by nanoclay addition increased the binding energy

between macromolecules and improved abrasion resistance, as the material was less likely to peel off.

It was observed that nanoclay changed PVDF crystal phase and the PVDF/nanoclay nanocomposites demonstrated improvements to properties such as increases in toughness, strength and abrasion resistance. The incorporation into PVDF had benefits not only in providing physical reinforcement to the polymer network, but also acting as morphology directors by stabilising a metastable or conventionally inaccessible polymer phase, or introducing new energy dissipation mechanisms [53, 109]. This led to enhanced toughness of the nanocomposites and greater abrasion resistance. It is evident that nanoclay has potential in improving these physical properties and hence the durability of PVDF membranes. However so far, this feature has not been explored on nanocomposite membranes.

2.3.2.3.3 Flux performance

PVDF/nanoclay membrane showed slightly lower water vapour flux than neat PVDF membrane during DCMD operation [108]. At inlet temperatures of 81.5°C (3.5 wt% NaCl aqueous solution) and 17.5°C (fresh water distillate), flux of the composite and the neat membrane was 79 kg/m²h and 84 kg/m²h respectively. The drop in flux could be due to increases in tortuosity and thermal conductivity that acts to lower the thermal efficiency of the DCMS process. Despite this drawback, the composite membrane demonstrated enhanced mechanical performance especially for long operation times as stated in Section 2.3.2.3.1.

2.3.2.3.4 Fouling resistance

A laboratory N-vinylpyrrolidone modified MMT improved the anti-fouling properties of PVDF membrane when tested with BSA fouling solution due to changes of surface hydrophilicity and morphologies [27]. The anti-fouling properties of PVDF nanocomposites using commercial nanoclay have yet to be investigated.

A summary of the major findings of selected PVDF nanocomposite flat sheet and hollow fibre membranes is listed in Table 2-2. Currently there is more work done on flat sheet membranes than hollow fibres likely due to the simpler setup procedures. Although flat sheet membranes can be used to evaluate water treatment performance including water permeability and fouling profiles, hollow fibre is the more common membrane format used in water treatment and as such studies performed on hollow fibres would be more relevant and applicable for water filtration uses. It was noted that the majority of the water treatment membrane studies focused on antifouling performance using nanoparticles including TiO_2 and SBA-15. While fouling is one of the durability issues mentioned in Section 1.2 and nanocomposite membranes have shown considerable improvement, fewer works focused on mechanical strength and none on abrasion resistance. Both PVDF flat sheet and hollow fibre membrane incorporated with commercial nanoclay have shown improved mechanical strength [83, 108]. While SBA-15 [22] and combination of $\text{TiO}_2/\text{Al}_2\text{O}_3$ [94] also showed better mechanical performance than neat PVDF membrane, nanoclay had the advantage of low cost, commercial availability and effectiveness with low loading. Although SBA-15 was promising for both anti-fouling and mechanical improvement, it was required to be synthesized in-house and thus complicated the membrane preparation process. As for $\text{TiO}_2/\text{Al}_2\text{O}_3$, a much higher loading was often required compared to nanoclay. Han *et al* [94] used 3% by weight of dope which was equivalent to 17% by weight of PVDF, which was considerably more than the 1 wt% Cloisite[®] nanoclay (by weight of PVDF) used by Wang *et al* [108]. Cost wise, nanoclay is more attractive and effective. The smaller loading of nanoclay is likely due to its ability to exfoliate and become finely dispersed in the polymer matrix. With the improvements observed in PVDF/nanoclay membranes for applications on lithium-ion battery and DCMD, there seems to be scope to improve MF/UF performance by inclusion of nanoclays.

Table 2-2. Summary of selected PVDF nanocomposite membranes prepared by NIPS

Nanofiller added	Type	Application	Casting condition	Observed changes	Ref
40% TiO ₂ by weight of PVDF	Flat sheet	Mechanical support for composite membrane	PVDF dissolved in DMAc with lithium chloride then mixed with TiO ₂ Quench bath medium: water	<ul style="list-style-type: none">• Stronger resistance to compaction under pressure of 30 bar. Decrease of pore volume % improved from 83% to 17%.• Produced better permeate quality with higher flux at elevated temperature and pressure (135°C/6.5 bar) in the vapour permeation test.	[93]
TiO ₂ , SiO ₂ and Al ₂ O ₃ Ratio of dope: PVDF/DMAc/NMP/nanoparticles/ PVP (18/59.2/14.8/3/5)	Hollow fibre	UF	24 h of mechanical stirring of PVDF and nanoparticles in DMAc/NMP/PVP at 25°C then 1 h of ultrasonic stirring. Internal coagulant: 40 wt% ethanol aqueous solution at 60°C External coagulant: water at 60°C	<ul style="list-style-type: none">• Increased dope viscosity.• Denser skin layer on the outer membrane surface.• Higher water permeability (increased from 82 L/m²h.bar to 352 L/m²h.bar with 2 wt% TiO₂ & 1 wt% Al₂O₃) but varying BSA rejection percentages.• Tensile strength was improved from 1.71 MPa to 3.74 MPa with 2 wt% TiO₂ & 1 wt% Al₂O₃.	[94]

0.12-0.72 wt% SBA-15 by weight of PVDF	Flat sheet	UF	PVDF dissolved in DMAc and mixed with PVP and SBA-15 at 60°C Quench bath medium: water	<ul style="list-style-type: none"> Improved mechanical properties: tensile strength increases from 0.151 MPa to 0.183 MPa (0.54 wt%); strain-at-break increases from 22.6% to 49.4% (0.36 wt%). Pure water flux increased from 372 L/m²h.bar to 502 L/m²h.bar (0.36 wt%). Ratio of permeate flux decline (flux ratio from start of filtration over set time) reduced from 24.4% to 15.5% (0.72 wt%) indicating antifouling property. 	[22]
1 wt% of Cloisite [®] Na+ or 1 wt% of Cloisite [®] 15A or 1 wt% of Cloisite [®] 20A, or 1 wt% of Cloisite [®] 30B by weight of PVDF	Flat sheet	Lithium-ion battery	PVDF dissolved in DMF at 70°C then mixed with clay/DMF suspensions. Air retention time: 30 s or 60 s Quench bath medium: water	<ul style="list-style-type: none"> Longer retention time resulted in increase of finger-like macrovoids. PVDF/15A with 30s in air had highest tensile strength (improved from 15 to 54 MPa). 	[83]
Cloisite [®] 20A Ratio of dope: PVDF/NMP/Cloisite [®] 20A/EG (10.0/74.7/3.3/12.0)	Hollow fibre	DCMD	PVDF stirred with clay in NMP and EG mixture. Internal and external coagulants: water	<ul style="list-style-type: none"> Lower ductility and tensile stress but higher modulus. Enhanced long-term mechanical stability. Reduced water vapour flux from 84 kg/m²h to 79 kg/m²h at inlet temperatures of 81.5°C/17.5°C (3.5 wt% NaCl/water). 	[108]

2.3.3 Synthesis of PVDF/nanoclay nanocomposites

To incorporate nanoclay into the PVDF matrix, an appropriate dispersion technique is needed so that uniform nanocomposite material can be formed. Depending on the status of layered silicate distribution in the polymer matrix, the morphology of polymer composite can be classified as phase separated, intercalated or exfoliated [110] as shown in Figure 2-6. For phase separated morphology, the polymer chain is unable to integrate with the clay layers and thus this type of polymer composite is considered as a conventional microcomposite. Polymer composites can be categorized as nanocomposites if they have either intercalated or exfoliated morphology. In intercalated nanocomposites, polymer chains are inserted between the clay layers to extend and expand the d-spacing (spacing between adjacent planes). In exfoliated state, the individual platelets randomly disperse in the polymer matrix and the d-spacing between the layers is further expanded. Complete exfoliation is often the preferred morphology, as it is associated with significant mechanical improvement with very low nanoparticle loading needed [103, 111, 112].

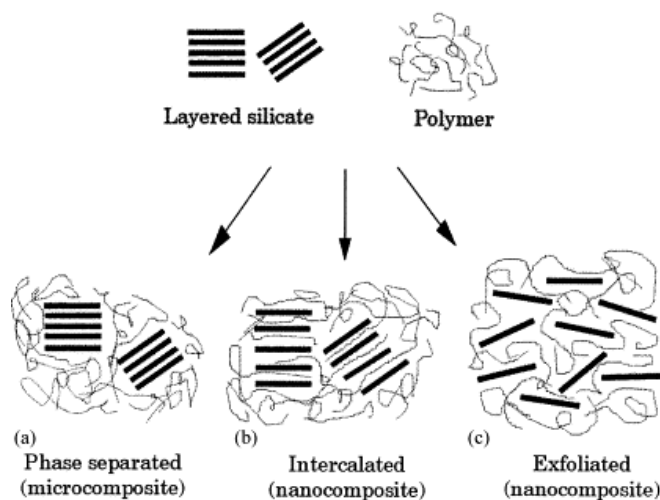


Figure 2-6. Schematic of three main types of polymer/layer structure composite morphologies: (a) microcomposites, (b) intercalated nanocomposites, and (c) exfoliated nanocomposites (reprinted with permission from [102], copyright (2000) Elsevier).

Various methods have been adopted to produce PVDF/nanoclay nanocomposites. For thermoplastics, high energy mixing with melt-intercalation can be used. As for nanocomposite synthesis that involves solvent, such as solution casting and NIPS, dispersing the nanoclay in solvent with prolonged stirring or ultrasonication is often adopted [45, 113]. Solvent is used to swell up the individual layers such that polymer

intercalation can occur in the galleries of the dispersed clay [103]. Dillon *et al* [113] work compared the properties of PVDF/nanoclay nanocomposite prepared by two different phase inversion techniques – co-precipitation (NIPS) and solution casting (solvent evaporation). It was shown that co-precipitation was the casting method that results in complete exfoliation of nanoclays (Cloisite[®] 15A and Cloisite[®] 25A) in PVDF composites while solution casting led to phase separation and intercalation in the nanocomposites. The nanoclay morphology was determined using wide angle X-ray diffraction (WAXD) and was confirmed by TEM images (Figure 2-7). PVDF β -phase was enhanced in all nanocomposites regardless the nanoclay morphology or loading.



Figure 2-7. TEM image of precipitated 2 wt% Cloisite 15A/PVDF after hot-pressing into a film. The exfoliated silicate layers appear as sharp lines on a grey background from the PVDF matrix (reprinted with permission from [113], copyright (2006) Elsevier).

In recent development, a new method using a microfluidizer has been adopted to deagglomerate and disperse CNT [114]. Results showed that the microfluidizer was able to further reduce the particle cluster size and narrow the size distribution of the dispersant that was originally prepared by stirring or shear-mixing. A microfluidizer is a high shear fluid processor, which can generate shear forces several orders of magnitude greater than that of conventional mixing techniques. Comparing with

ultrasonication, it was reported that nano-emulsion dispersed by microfluidizer had narrower size distributions, indicating the particle size was more uniform [115]. Microfluidizers are popular among the pharmaceutical, biotechnology and food industries for uniform particle size reduction in their respective applications. However the role of mixing in formation of more durable nanocomposite membranes has not been widely explored.

2.4. Abrasion theory

Ratner *et al* [116] has proposed a theory for abrasive wearing of polymer as:

$$W = \frac{k\mu}{H\sigma\varepsilon} \quad (1)$$

where W is the specific wear rate, μ is the coefficient of friction, H is the indentation hardness, σ is the tensile strength, ε is the elongation at max load and k is a proportionality constant. In particular, the product $\sigma\varepsilon$ denotes the work needed to separate a particle from the wearing surface by tensile failure and it is indirectly proportional to the abrasion wear rate. This correlation between wear rate and $\sigma\varepsilon$ has shown reasonably good linear agreement for a number of polymers at room temperature including PE, poly(methyl methacrylate) (PMMA), PTFE and poly(vinyl chloride) (PVC) [117, 118] as shown in Figure 2-8. The convenience of this method is that it relies on mechanical properties that can be readily measured by tensile testing instrument. How this theory applies to wear on porous membranes is yet to be confirmed against actual abrasion resistance, as membranes have an asymmetric morphology while uniform polymer blocks were used in the wear tests for establishing the theory. Also, the theory was developed based on neat polymeric materials and this study will verify if it is applicable on nanocomposite materials.

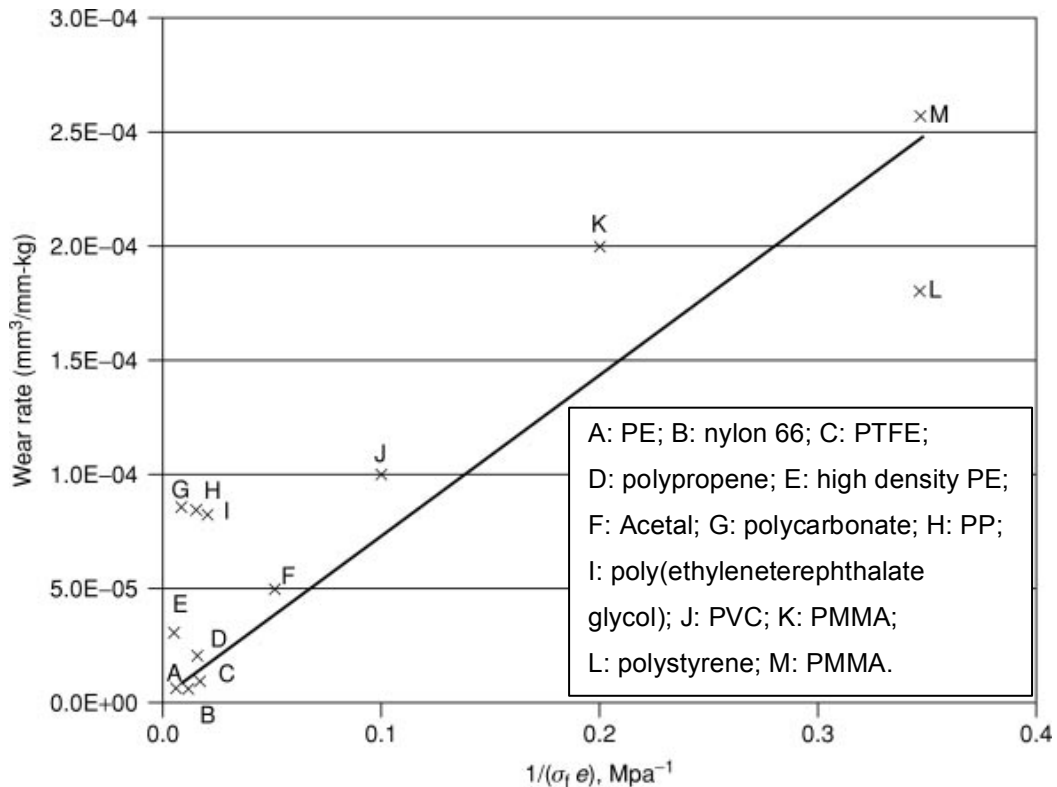


Figure 2-8. A plot of wear rate as a function of the reciprocal of the product of tensile strength and elongation at max load (reprinted with permission from [118], copyright (2006) Wiley).

2.5. Objective of this work

From this review, it is clear that some work has been carried out exploring the improvement to physical strength [22, 26, 83, 93, 95, 108], flux [22, 25, 26, 94-96] and antifouling [22-27] properties of membranes by inclusion of nanoparticles. However, one of the major factors limiting wider application of membranes is physical durability. Their ability for enhanced abrasion resistance has not been explored, where improved materials are useful for applications treating feed containing abrasive particulates. Further work in this area is therefore needed in order to extend the mechanical improvement on general nanocomposite materials to membranes.

The aim of this research is to develop novel nanocomposite membrane materials that will improve the durability and performance of hollow fibre membranes in water treatment. The key issues which the new materials aim to improve are membrane abrasion resistance and mechanical strength with either uncompromised or improved performance in terms of flux and separation. The project will carry this out using a materials science approach, harnessing conventional and sophisticated (i.e.

synchrotron) characterization systems to understand and select the required material features. This will be done via developing procedures to produce stable polymer materials with excellent dispersion of the inorganic nanoparticles, test them under realistic working environments (such as abrasive and high fouling environments) as well as to investigate the meaningful characteristics of materials using imaging (SEM and TEM) and other materials characterization systems (FTIR, X-ray scattering, pore size, etc.). These tools have been vital to the researchers exploring functional membrane properties and hence their interest in this study.

Based on the literature review, the following specific objectives were set to address this overall outcome of improved abrasion resistance of PVDF-nanoclay membranes:

1. Determine the best dispersion techniques to incorporate nanoclays into PVDF and explore how this dispersion influences the performance as membranes.
2. Explore how membrane properties of water permeability, mechanical strength and abrasion resistance are influenced by nanoclay using flat sheet membrane materials; then link these to changes in thermal properties, crystal phase and morphology.
3. Optimize casting conditions of flat sheet membranes to achieve high nanoparticle retention as well as intact membrane films, then explore how these conditions alter material properties including crystal phase and morphology.
4. Apply knowledge from objectives 1-3 to develop hollow fibre nanocomposite membranes to demonstrate the improved membrane properties and abrasion resistance on the more industrially applicable membrane format.

3. Experimental

In this chapter, the experimental methods for this research are presented. First, the materials used are summarised. Then, the methods to disperse nanoparticles are introduced and the procedure of the preparation of flat sheet and hollow fibre membranes are described. Various casting conditions in order to optimise nanoclay incorporation are also listed. Finally, a variety of characterization techniques which were used to study membrane properties and performance are explained in detail.

3.1. Materials

Three commercially available PVDF materials (Solef[®] 1015, Solef[®] 6008 and Solef[®] 6020) from Solvay Solexis were used as membrane materials. The details of these materials are listed in Table 3-1. Eight types of commercially available nanoclay, which were organically modified MMT (MMT is a natural clay product), were used in this study. The inorganic cations between the nanoclay platelets were exchanged with various alkylammonium ions to give better compatibility with the polymer matrix [103]. Cloisite[®] 10A, Cloisite[®] 15A and Cloisite[®] 30B were supplied by Southern Clay Products (Gonzales, TX, USA). Nanomer[®] I.28E, Nanomer[®] I.30E, Nanomer[®] I.31PS, Nanomer[®] I.34TCN and Nanomer[®] I.44P were obtained from Nanocor (Hoffman Estates, IL, USA). The properties of these nanoclays are listed in Table 3-2. The inorganic part of the nanoclay has the general formula $(\text{Na,Ca})_{0.33}(\text{Al,Mg})_2(\text{Si}_4\text{O}_{10})(\text{OH})_2 \cdot n\text{H}_2\text{O}$. The solvent used to dissolve the PVDF and disperse the nanoclays was industrial grade NMP from ISP (Wayne, NJ, USA). Glycerol, ReagentPlus[®], $\geq 99.0\%$ (GC), from Sigma-Aldrich and sodium chloride (NaCl) AR grade from Merck were used as additives in the quench baths. Milli-Q water was used in the quench bath, filtration tests and abrasion slurries, and the resistivity of the Milli-Q water was 18.2 M Ω -cm at 25°C.

Table 3-1. Properties of PVDF raw materials

Name	Molecular Weight (kDa)	Specific gravity
Solef [®] 6008	244	1.78
Solef [®] 1015	573	1.78
Solef [®] 6020	687	1.78

Table 3-2. Properties of nanoclays

Name	Organic modifier		% Weight loss on ignition	Specific gravity	d ₀₀₁ spacing (nm)
Cloisite [®] 10A	dimethyl, benzyl, hydrogenated tallow, quaternary ammonium	$ \begin{array}{c} \text{CH}_3 \\ \\ \text{CH}_3 - \text{N}^+ - \text{CH}_2 - \text{C}_6\text{H}_5 \\ \\ \text{HT} \end{array} $	39%	1.90	1.92
Cloisite [®] 15A	dimethyl, dihydrogenated tallow, quaternary ammonium	$ \begin{array}{c} \text{CH}_3 \\ \\ \text{CH}_3 - \text{N}^+ - \text{HT} \\ \\ \text{HT} \end{array} $	43%	1.66	3.15
Cloisite [®] 30B	methyl, tallow, bis-2-hydroxyethyl, quaternary ammonium	$ \begin{array}{c} \text{CH}_2\text{CH}_2\text{OH} \\ \\ \text{CH}_3 - \text{N}^+ - \text{T} \\ \\ \text{CH}_2\text{CH}_2\text{OH} \end{array} $	30%	1.98	1.85
Nanomer [®] I.28E	trimethyl stearyl ammonium	$ \begin{array}{c} \text{CH}_3 \\ \\ \text{CH}_3 - \text{N}^+ - (\text{CH}_2)_{17}\text{CH}_3 \\ \\ \text{CH}_3 \end{array} $	25-30%	1.80	2.4-2.6
Nanomer [®] I.30E	octadecyl ammonium	$ \begin{array}{c} \text{H} \\ \\ \text{H} - \text{N}^+ - (\text{CH}_2)_{17}\text{CH}_3 \\ \\ \text{H} \end{array} $	25-30%	1.90	1.8-2.2

Nanomer [®] I.31PS	octadecyl ammonium	$\begin{array}{c} \text{H} \\ \\ \text{H} - \text{N}^+ - (\text{CH}_2)_{17}\text{CH}_3 \\ \\ \text{H} \end{array}$	15-40%	1.90	1.8-2.2
	and				
	aminopropyltriethoxysilane	$\begin{array}{c} \text{H} \qquad \text{OC}_2\text{H}_5 \\ \qquad \\ \text{H} - \text{N}^+ - (\text{CH}_2)_3 - \text{Si} - \text{OC}_2\text{H}_5 \\ \qquad \\ \text{H} \qquad \text{OC}_2\text{H}_5 \end{array}$			
Nanomer [®] I.34TCN	methyl dihydroxyethyl hydrogenated tallow ammonium	$\begin{array}{c} \text{CH}_2\text{CH}_2\text{OH} \\ \\ \text{CH}_3 - \text{N}^+ - \text{HT} \\ \\ \text{CH}_2\text{CH}_2\text{OH} \end{array}$	25-30%	1.90	1.8-2.2
Nanomer [®] I.44P	dimethyl dialkyl(C14-C18) amine	$\begin{array}{c} \text{CH}_3 \\ \\ \text{CH}_3(\text{CH}_2)_{17} - \text{N}^+ - (\text{CH}_2)_{17}\text{CH}_3 \\ \\ \text{CH}_3 \end{array}$	35-45%	1.90	2.4-2.6

* where T is tallow (~65% C18; ~30% C16; ~5% C14)

3.2. Dispersion of nanoclay

3.2.1 Methods to disperse nanoclay

In order to select the most appropriate option for dispersing nanoclay for membrane fabrication, various methods were investigated for their ability to disperse nanoclay in the selected solvent. Four different instruments were used to disperse nanoclay into NMP: (1) ultrasonication at 40 W with operating frequency of 50 kHz in an Ultra K42-752 ultrasonic bath by Unisonics Pty Ltd (NSW, Australia), (2) Thinky Mixer ARE-250 by Thinky Corporation (Tokyo, Japan), a planetary centrifugal mixer, at 2000 rpm, (3) overhead stirrer with 60 mm stirring paddle from VELP Scientifica at 200 rpm in a 250 ml flask and (4) M-110Y Microfluidizer Processor by Microfluidics (Newton, MA, USA) for high-shear fluid processing. As the nanoclay formed very large agglomerates after NMP was added, the nanoclay/NMP mixture was ultrasonicated for one hour in order to break down the agglomerates so that they would not obstruct the inlet of the microfluidizer. The stability of the microfluidized dispersions was tested by measuring the particle size after the dispersions were stagnant for at least 12 days. The ability of using ultrasonication to redisperse the microfluidized nanoclay was also investigated.

Two nanoclay dispersions made with Cloisite[®] 30B and Nanomer I.30E were tested respectively. The mass ratio of nanoclay to NMP used was 1:84, assuming the dope solution has a mass ratio of nanoclay to PVDF to NMP 1:15:84 as the PVDF to solvent ratio usually ranges from 10:90 to 20:80 [86].

3.2.2 Characterization of dispersions

Dynamic light scattering (DLS) using a Zetasizer Nano ZS from Malvern Instruments was carried out to measure the size and the size distribution of the nanoparticles in the dispersions. For dispersion methods (1) to (3) mentioned in Section 3.2.1, small samples were taken from the dispersions at various time intervals and particles were measured for their size by DLS described in Section 3.4.1. For method (4), sample size was measured after completion of each dispersion cycle. For each cycle, the entire batch of nanoclay dispersion entered from the product inlet reservoir and underwent a high-shear fluid process at 5000 psi (34.5 MPa) before exiting through the outlet. At least three size distribution measurements were taken for each sample, and the average intensity-weighted mean diameter recorded.

3.3. Membrane preparation

3.3.1 Flat sheet membrane preparation

Pure PVDF and PVDF/nanoclay nanocomposite membranes were prepared by NIPS. PVDF Solef® 1015 and half of the NMP solvent was stirred with an overhead mixer with a 60 mm stirring paddle at 200 rpm at 90°C for 20 hours. The nanoclay was dispersed in the remaining half of the NMP by ultrasonication for two hours before mixing with the PVDF/NMP solution. The combined solution (or dope) was stirred at 90°C for 3.5 hours, followed by 30 minutes settling time under vacuum to remove excessive air bubbles. The dope appeared to be clear for pure PVDF and became cloudier as the nanoclay loading increased.

The dope was then coated on a glass substrate with a doctor blade using a gap thickness of 300 µm to form thin films. The membrane was formed by immersion in Milli-Q water at 60°C for 15 minutes, where skin layer was formed on the membrane surface that was in contact with the quench medium. A portion of the membranes were soaked overnight in a 15 wt% glycerol/water solution in order to preserve their porous structure [95] so they could be stored for later analysis. The membranes were dried in a thermostat cabinet at 30°C for 48 hours.

A number of flat sheet membranes were prepared with this procedure and the detailed composition will be specified in the respective results and discussion chapters. Several membranes were also fabricated by dispersing the nanoclay in NMP with ultrasonication for one hour followed by processing with the microfluidizer for ten cycles. This was to investigate the impact of combining dispersing technique to the membrane material properties.

3.3.2 Membrane preparation for optimization of nanoclay inclusion

To minimize the loss of nanoparticles during the membrane formation process, casting conditions were varied to identify the impact on the retention of nanoparticles within the membrane material. This also provided an opportunity to understand more about casting conditions using flat sheet membranes, which were relatively easier to fabricate, before proceeding to fabrication of hollow fibre membranes at larger scale. The conditions that were investigated are described in the following sections, which include the type of nanoclay, retention time of casting dope in air, temperature and composition of the quench bath, the humidity of the casting environment, the PVDF/NMP ratio of the dope and finally the molecular weight of PVDF. To investigate

the effect of each condition, only one parameter was changed at a time in the casting process. PVDF/nanoclay nanocomposite flat sheet membranes (5 wt% nanoclay, by weight of PVDF in the synthesis solution) were prepared according to Section 3.3.1 as the standard conditions. The standard conditions are summarized in Table 3-3.

Table 3-3. Standard casting conditions.

Parameter	Condition
Air retention time	0 minutes (immediate immersion)
Quench bath temperature	60°C
Quench bath medium	Water
Humidity	Room condition (40-50%RH)
Ratio of PVDF/Nanoclay to NMP	15:85
Molecular weight of PVDF	570 kDa (Solef [®] 1015)

3.3.2.1 *Effect of various nanoclays*

Eight different types of nanoclay listed in Table 3-2: Cloisite[®] 10A, 15A and 30B and Nanomer[®] I.28E, I.30E, I31PS, I.34TCN and I.44P, were used. Dopes with 5 wt% nanoclay (by weight of PVDF) were prepared. I.30E was selected for use in the subsequent experiments investigating changes in casting conditions as it had the highest percentage retained in the membrane as measured by TGA (Section 3.4.2.1).

3.3.2.2 *Air retention time*

One sample of dope was poured into the doctor blade and cast into films which were exposed in air for 0, 1, 5 and 10 minutes before immersing into the quench bath.

3.3.2.3 *Quench bath temperature*

Three water baths were set at 20°C, 40°C and 60°C respectively. These temperatures are commonly used in NIPS processes [78]. One sample of dope was cast and placed into each of the three different baths.

3.3.2.4 *Quench bath medium*

Four quench baths each with different non-solvent were prepared and membranes were cast using the same dope. The use of additives can influence the demixing rate

or the interaction between the polymer and the nanoclay. Table 3-4 shows the components of each quench bath.

Table 3-4. Composition of the quench bathes

Quench bath no.	Components
1	Water
2	10wt% NaCl; 90wt% water
3	10wt% NMP; 90wt% water
4	10wt% glycerol; 90wt% water

3.3.2.5 Humidity of the casting environment

A temperature-humidity cabinet from Thermoline was used to create casting environments variously with low and high humidity. The temperature of the cabinet was set at 30°C and the humidity were set at either 30%RH or 90%RH for each experiment. For two different trials with the same dope composition, the film was cast onto the glass plate and left in the cabinet for 1.5 minutes before immersing into the water bath at 60°C.

3.3.2.6 Ratio of PVDF/Nanoclay to NMP

The ratio of PVDF+nanoclay to NMP in the dope was varied between 10:90, 15:85, and 20:80.

3.3.2.7 Molecular weight of PVDF

Three types of PVDF with different molecular weight (Solef[®] 6008, 244 kDa; Solef[®] 1015, 570 kDa and Solef[®] 6020, 700 kDa) were used.

3.3.3 Hollow fibre membrane preparation

Hollow fibre membranes with various nanoclay loadings and a control membrane which contained 0 wt% nanoclay were prepared. The hollow fibres were all prepared at the Research and Development laboratories of Memcor Products, Siemens Ltd, South Windsor, Australia, using their pilot extrusion extruder. A preliminary study was carried out that fabricated nanocomposite hollow fibres with 5.08% loading each of eight type of nanoclay as listed in Table 3-2. Mechanical testing (Section 3.4.7)

showed that membranes with Cloisite[®] 30B and Nanomer[®] I.44P had the best mechanical properties in terms of stiffness and ductility respectively (Table 3-5). As such, those two nanoclays were selected for further study with various loadings. Table 3-6 summarises the various nanoclay loadings used, with nanoclays loadings up to 5.08 wt%. 300 g of dope was prepared for each membrane extrusion trial.

Table 3-5. Mechanical properties of membranes

Membrane	Tensile strength, σ (MPa)	Elongation at max load, ϵ (%)	Young's modulus (MPa)
0% Nanoclay	3.78 \pm 0.19	175 \pm 15	63 \pm 6
10A 5.08	3.27 \pm 0.05	174 \pm 6	62 \pm 2
15A 5.08	4.14 \pm 0.05	207 \pm 9	71 \pm 1
30B 5.08	4.30 \pm 0.28	161 \pm 28	84 \pm 10
I28E 5.08	3.31 \pm 0.52	164 \pm 23	56 \pm 7
I30E 5.08	Fibres were lumpy and unable to be used for test.		
I31PS 5.08	3.75 \pm 0.10	183 \pm 8	62 \pm 6
I34TCN 5.08	4.25 \pm 0.10	194 \pm 16	73 \pm 2
I44P 5.08	3.84 \pm 0.12	229 \pm 3	65 \pm 3

Table 3-6. Membrane composition

Name	Nanoclay Type	Nanoclay loading % in dope (by weight of PVDF)
0% Nanoclay	-	0
30B 0.88	Cloisite [®] 30B	0.88
30B 2.61	Cloisite [®] 30B	2.61
30B 5.08	Cloisite [®] 30B	5.08
I44P 0.88	Nanomer [®] I.44P	0.88
I44P 2.61	Nanomer [®] I.44P	2.61
I44P 5.08	Nanomer [®] I.44P	5.08

The nanoclay was first dispersed in NMP with ultrasonication for one hour and further dispersed with the microfluidizer for 10 cycles. The dispersion was then mixed with the PVDF based polymer in an oven at 90°C for 48 hours under a nitrogen atmosphere. The hollow fibre membranes were extruded with a dry-wet spinning process and they were formed through a non-solvent induced phase separation mechanism using a 60°C water bath. A portion of the membranes were soaked

overnight in a 10 wt% glycerol/water solution in order to preserve their porous structure for later characterisation. The membranes were dried at ambient temperature for 48 hours. No abnormalities were observed among all batches of membranes and sections of fibres that appeared intact were selected for subsequent testings.

3.4. Characterization of membranes

3.4.1 Particle size in dispersions

To give an indication of the nanoparticle size in the NMP suspensions, a Zetasizer Nano ZS (Malvern Instruments) was used to measure the size of the nanoparticles following the dispersion process. The instrument uses the DLS technique which measures the diffusion of particles moving under Brownian motion, and converts this to size and a size distribution based on the Stokes-Einstein equation. As the Stokes-Einstein equation was developed upon the assumption of hypothetical hard spheres, the measurement from the particle sizer does not necessarily reflect the true size of nanoclay as it has a platelet or aggregate structure. It can however be used as a reference to other size measurement methods such as elemental mapping by SEM/EDS (Section 3.4.5.1) or for comparison purpose.

To do the measurement, small samples were taken from the nanoclay dispersions and diluted with NMP to about 0.02 wt%, so as to be in the concentration range suitable for particle sizer operation. At least three measurements were taken for each sample, and the average recorded. No apparent change in particle size was observed during the measurements, occurring over a period 30 minutes.

3.4.2 Thermal decomposition

Thermogravimetric analysis (TGA) was carried out to study the thermal decomposition profile of the nanoclays and the membranes. It was also one of the methods used to determine the weight of inorganic residue and thus calculate nanoclay retention in the membrane as described elsewhere [119]. The end point of TGA reveals the actual nanoclay loading that has been incorporated into the membranes when all of the organic component (both from the PVDF and original nanoclay) has been combusted. However large variability was observed when using TGA to determine nanoclay loading, so loss on ignition (LOI) was considered instead. The sample size used in LOI was greater than that in TGA, typically 500 mg verses 10 mg.

This greater amount of sample resulted in a smaller relative error for the residual nanoclay content.

3.4.2.1 Thermogravimetric analysis (TGA)

TGA was performed using a PerkinElmer TGA 7. Nanoclay, PVDF and nanocomposite membrane samples were heated from 50°C to 850°C at a rate of 20°C/min under air at 20 mL/min. TGA thermograms were plotted to show the weight loss percentage of the samples as the temperature increased. Three samples of each type of membrane were tested to ensure statistical certainty of the results.

3.4.2.2 Loss on ignition (LOI)

The LOI testing was carried out by Sharp & Howells, a National Association of Testing Authorities, Australia (NATA) accredited laboratory, using platinum crucibles based on Australian Standard AS3583.3-1991 [120]. Several types of crucible including porcelain, nickel and Inconel were initially used but discontinued due to their inability to resist the reaction of fluorinated polymer combustion by-products released upon the decomposition of PVDF (e.g. hydrogen fluoride). A platinum crucible was eventually selected due to its strong resistance to the breakdown products of fluorinated polymers. An empty crucible was first weighed (m_0) before an average of 0.5 g of membrane was added. The total weight was then recorded (m_1). The crucible with the membrane was placed inside a muffle furnace at 750°C for 60 minutes to remove the organic content. After cooling, the crucible with the residue was weighed again (m_2) to determine the ash content of the membrane. The residue % was calculated by Equation (2).

$$\text{Residue \%} = \frac{m_2 - m_0}{m_1 - m_0} \times 100\% \quad (2)$$

The inorganic content of the various nanoclays was also determined by the same method. Based on this and the original nanoclay loading in the synthesis solution, the original inorganic loading was calculated. This value was compared against the residue % to find out the percentage of nanoclay retained in the membrane. At least three tests were carried out for each type of membrane and nanoclay.

3.4.3 Characterisation of polymer crystalline phase

The crystalline phase of the polymer was determined with Fourier-transform infrared spectroscopy (FTIR). To confirm the viability of FTIR as a simple check for crystallinity, results were compared against X-ray powder diffraction (XRD).

3.4.3.1 Fourier-transform infrared spectroscopy

FTIR absorption spectra of the membranes were measured with a PerkinElmer Spectrum™ 100 FTIR-ATR to compare the crystalline phases present in the membranes. A segment of membrane was placed onto the diamond ATR top-plate and pressure was applied until clear spectral bands were shown on the display. Based on the method reported in the literature [121, 122], the beta fraction (F_β) of a crystalline phase, which is the mass fraction of the β -phase in the PVDF crystal, can be estimated from the absorbance of the characteristic peaks of all crystalline phases and their absorption coefficients as follows:

$$F_\beta = \frac{A_\beta}{\left(\frac{k_\beta}{k_\alpha}\right)A_\alpha + A_\beta} \quad (3)$$

where A_α and A_β are the peak areas of the absorption peaks of α -phase and β -phase at 763 cm^{-1} and 840 cm^{-1} respectively. Absorption coefficients of α -phase (k_α) and β -phase (k_β) were taken as $6.1 \times 10^4 \text{ cm}^2/\text{mol}$ and $7.7 \times 10^4 \text{ cm}^2/\text{mol}$ accordingly [121, 122].

To confirm the FTIR's ability to determine crystal phase change, the crystalline structure of the membranes was also studied using XRD.

3.4.3.2 X-ray powder diffraction

The XRD patterns were recorded using a Bruker D8 X-ray diffractometer (Germany) with Ni-filtered Cu K α radiation ($\lambda=1.5406 \text{ \AA}$) operated at 40 kV, 40 mA from 10° to for 30° for 2θ . No special sample preparation was needed as the membranes were thin films and could be examined directly.

The X-ray diffraction patterns and FTIR spectra of PVDF and PVDF/nanoclay nanocomposite membranes made with 1 wt%, 3 wt% and 5 wt% initial loading of Cloisite® 30B are shown in Figure 3-1. In Figure 3-1(a), pure PVDF membrane showed

characteristic α -phase peaks for (020), (110) and (021) at 18.4° , 20.0° and 26.7° , corresponding to d-spacing of 0.49 nm, 0.45 nm and 0.34 nm respectively. With addition of nanoclay, these α -phase peaks disappeared and the peak size of β -phase peak at 20.5° ($d_{200/100}=0.44$ nm) increased with the nanoclay loading. A similar trend was also observed with FTIR as shown in Figure 3-1(b). The spectra exhibit strong peaks that are associated with different crystalline phases of PVDF. Major peaks were observed at 763 cm^{-1} and 796 cm^{-1} corresponding to the α -phase of PVDF, as well as at 840 cm^{-1} corresponding to the β -phase of PVDF [53, 122]. The α -phase peak intensity decreased in tandem with an increase in the β -phase peak for the nanocomposite membrane samples. While XRD, a technique that specifically responds to crystalline materials, confirmed the FTIR findings, FTIR is more convenient to measure a large quantity of samples. As such, FTIR was selected as the method to study membrane crystal structure in subsequent chapters.

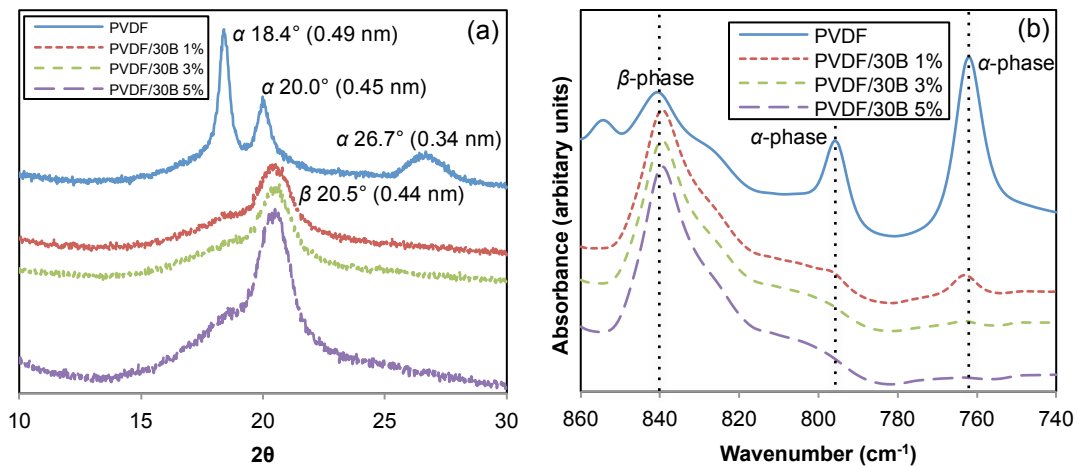


Figure 3-1. X-ray diffraction patterns (a) and FTIR spectra (b) of PVDF and PVDF/30B nanocomposite membranes.

3.4.4 Small angle X-ray scattering

Small angle X-ray scattering (SAXS) is a technique to analyze nanostructured materials providing information including particle sizes and size distributions. Synchrotron SAXS measurements on the nanocomposite membranes and nanoclay were performed using the SAXS beam line at the Australian Synchrotron. The advantage of using synchrotron SAXS is that X-rays are produced at very high flux which results in fast measurement and clear signals. A sample of membrane was

mounted over the holes on sample plate as shown in Figure 3-2. As for the nanoclays, the powder samples were first filled into 1.5 mm diameter quartz capillaries then mounted onto the sample plate. The camera length (sample to detector distance) used was 0.6 m to measure Q range from 0.029 to 1.514 Å⁻¹. This spacing corresponds to a d-spacing of 0.4 to 21.7 nm, which is useful for exploring the space between nanoclay plates. The X-ray energy used was 12 KeV and acquisition time of 2 s was used for all samples.

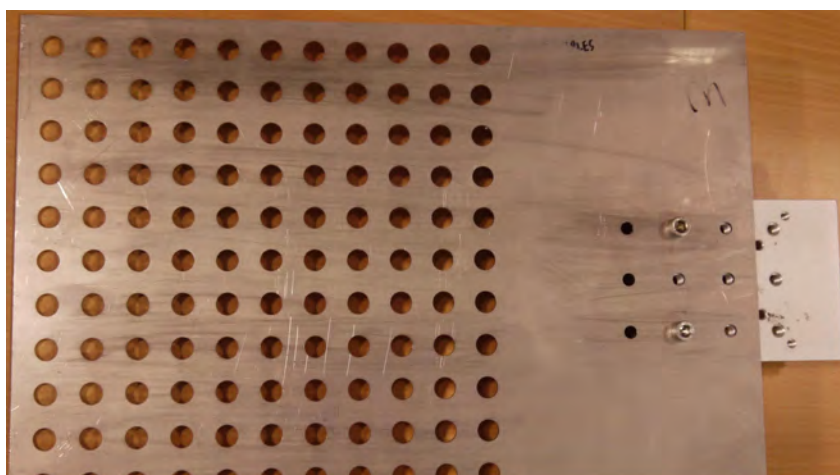


Figure 3-2. Sample plate for SAXS (image from the Australian Synchrotron website).

3.4.5 Electron microscopy

3.4.5.1 *Scanning electron microscopy*

Scanning electron microscopy (SEM) of the cross sections of the flat sheet membranes and the hollow fibres were taken with a Nikon/JEOL NeoScope JCM-5000 and a Philips XL30 Field Emission Scanning Electron microscope (FESEM) respectively. To obtain the cross section, the membrane sample was first fractured after dipping into liquid nitrogen. Imaging and elemental mapping was carried out on both the skin layer surface (outer surface for hollow fibre and quench side surface for flat sheet) and the cross section of the hollow fibre membranes. The samples were mounted on aluminium stubs with double-sided conductive carbon tape. These samples were then carbon coated using a Polaron carbon sputter coater. The thickness of the carbon coating was approximately 240 Å. Once coated, the samples were placed into a Philips XL30 FESEM for imaging. An accelerating voltage of 10kV was used for the images and X-ray maps. The EDS (Energy Dispersive Spectroscopy)

X-ray analysis system was an Oxford Instruments Pty Ltd system which incorporated an X-Max 80 mm² x-ray detector and Aztec software.

3.4.5.2 Transmission electron microscopy

The morphology of the nanocomposite membranes was examined with transmission electron microscopy (TEM). A JEOL 2100 TEM, situated at Deakin University (Institute for Frontier Materials, Waurn Ponds) with an accelerating voltage of 200 kV was used for the TEM experiments. To prepare the ultrathin cross section for TEM, a membrane sample was first embedded and cured in an epoxy resin block. A Leica ultramicrotome with diamond knife was then used to prepare approximately 150 nm thick samples at room temperature, which were collected on copper grids for TEM experiments.

3.4.6 Porosity and average pore size (hollow fibre membranes)

The porous structure of the bulk membrane material (including supporting layers) was characterised by determining porosity and average pore size. Porosity of the membrane (ε) refers to the amount of void space that the membrane contains. It was calculated from the bulk density of the membrane ($\rho_{membrane}$) and the density of PVDF and nanoclay ($\rho_{nanocomposite}$), using Equation (4)

$$\varepsilon = 1 - \frac{\rho_{membrane}}{\rho_{nanocomposite}} \times 100\% = 1 - \frac{M_{membrane}/V_{membrane}}{\rho_{PVDF} \times (1 - nanoclay\%) + \rho_{nanoclay} \times nanoclay\%} \times 100\% \quad (4)$$

where $M_{membrane}$ (g) is the mass of a 10 cm membrane segment, $V_{membrane}$ (cm³) is the volume of the membrane segment (its cross sectional area was determined via SEM imaging and used to estimate the volume), ρ_{PVDF} and $\rho_{nanoclay}$ (g/cm³) are the density of the raw materials obtained from the material data sheet and *nanoclay %* was determined by LOI. It was assumed that the hollow fibre membrane was a perfect annulus and three weight measurements were taken for each type of membrane.

Average pore size of the membrane skin layer surface was determined via SEM imaging of the surface (Philips XL30 FESEM instrument described in Section 3.4.5.1). 20 pore diameters were measured and the average was recorded. This technique gives the dry pore size of the membrane which may be different from the actual pore size under filtration conditions. To estimate pore size under atmospheric conditions, a capillary flow porometer can be used. However, the hollow fibre membranes in this

study could not withstand the pressure applied during attempts to determine the pore size this technique. Therefore, the visual SEM approach was adopted to provide an estimate of the membrane pore size.

3.4.7 Mechanical testing

Mechanical properties including elongation at maximum load, tensile strength, Young's modulus and the modulus of toughness of the membranes were measured using an Instron (5567 for flat sheet and 5500R for hollow fibre) tensile testing instrument at room temperature. The initial gauge length was 20 mm for flat sheet membranes and 100 mm for hollow fibre membranes, and the testing speed was 400 mm/min. At least five samples of each type of membrane were tested to ensure statistical certainty of the results.

3.4.8 Abrasion testing

The abrasion resistance of flat sheet and hollow fibre membranes were tested with different approaches due to their different physical features of being either a flat sheet or hollow fibre. Flat sheet membranes were tested with a standard tribological technique of two surfaces moving in relative motion to each other with one being harder or more abrasive than the other. Because of their flat surface, they could be easily placed into the holder of a commercial wear and abrasion tester and sandpaper was used as the abrasive material. On the other hand, for hollow fibres of cylindrical shape this was difficult to evaluate. As such, an in-house testing method using abrasive slurry and bubble point measurement was developed to examine the abrasion resistance of the hollow fibre membranes. This method also simulates more realistic abrasion conditions in water treatment applications, but is slower to obtain results. Details of the two testing methods are presented below.

3.4.8.1 *Standard tribological technique with sand paper*

Abrasion resistance of the flat sheet membrane was tested with a Martindale Wear & Abrasion Tester (James H. Heal & Co. LTD) under a pressure of 9 kPa at Standard Textile Testing Conditions ($20 \pm 2^\circ\text{C}$ and $65 \pm 3\%$ RH). All membranes were tested on the same instrument at the same time. The membranes were mounted to holders so that the skin layer of the membrane was contacting the abrasive material underneath.

It was essential to ensure this arrangement as the skin layer controls the functional separation process and its abrasion resistance is thus more significant than the supporting membrane material. The test was repeated using two different grades of sandpaper made with silicon carbide grain of grit size P1000 and P1200 as the abrasive material. The membrane samples were weighed using a digital balance with an accuracy of 0.0001 g before and in between the abrasion cycles to record the loss in mass due to abrasive wearing. SEM images of the original and the abraded membrane surface were taken using the Nikon/JEOL NeoScope JCM-5000 described in Section 3.4.5.1.

3.4.8.2 Abrasive slurry and bubble point method

Silicon carbide with 200-450 mesh (32-75 μm) particle size obtained from Sigma-Aldrich was selected to be the abrasive material. It is commonly used in abrasion testing, but represents the harder and more abrasive particles such as sand and silica based debris which are commonly found in seawater described in Section 1.2.2. As it is impractical to simulate a real life conditions with abrasion occurring over an extended time (3-8 years) [34, 35], an accelerated test method with high concentrations of abrasive particle was used, in the order of 10 wt%, where they normally occur in the order of parts per million. The abrasive slurry test was a comparative experiment which evaluated the abrasion resistance of the nanocomposite membranes relative to a control membrane without nanoclay.

To setup the abrasion test, 100 g of abrasive slurry made up of 10 wt% silicon carbide in deionized water was placed in a 150 ml Erlenmeyer flask to allow sufficient movement of the slurry. For each type of membrane, a single fibre was coiled into a loop and potted in a nylon support with epoxy resin. It was then secured in the flask with a rubber stopper as shown in Figure 3-3. All membranes had an identical geometric arrangement with up to 12 membranes tested in parallel during the same experiment. The flasks were placed in a Ratek SWB20 shaking instrument and the membranes were shaken at a fast speed in the abrasive slurry for several days.

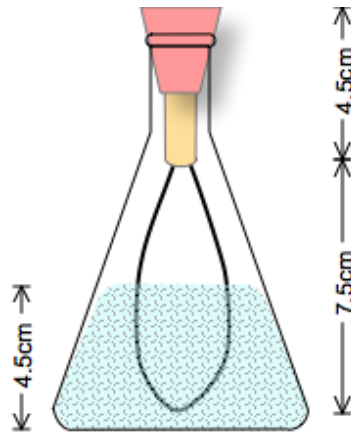


Figure 3-3. Setup for each membrane fibre in the slurry flask for the abrasion resistance testing

Hollow fibre membranes made according to Section 3.3.3 were typically asymmetric with the skin layer on the outer surface. It was expected that the surface of the membranes would be abraded by the silicon carbide particles and lead to an increase in the maximum pore size as a result of breaking through the smaller pore size skin layer to the more openly porous support layer. Such a mechanism can be considered as failure of the membrane, as the functional separation layer has been compromised. To verify this, the membranes were taken out periodically to measure their respective bubble point which indicates the maximum pore size. A decrease in the measured bubble point representing an increase in the maximum pore size was interpreted as abrasive wear of the membranes.

The maximum pore size, d (μm), was estimated using bubble point theory [123] from Equation (5)

$$d = \frac{4 \cdot \kappa \cdot \sigma \cdot \cos \theta}{p_{bp}} \quad (5)$$

where κ is the pore shape correction factor, σ (dynes/cm) is the surface tension at the air-liquid interface, θ ($^\circ$) is the liquid-membrane contact angle and p_{bp} (kPa) is the bubble point pressure. The surface tension of water is 72.8 dynes/cm at 20°C. Contact angle was assumed to be 0° which results in the largest estimate of pore size. The pore shape correction factor was chosen as 1, assuming a perfectly cylindrical pore. These parameters were selected as such to give the most conservative pore size (largest pore size) following the Membrane Filtration Guidance Manual by US EPA [124]. It also allowed assessment of the relative changes in pore size during abrasion testing for monitoring membrane integrity.

SEM images of the original and the abraded membrane surface were taken with the Philips XL30 FESEM described in Section 3.4.5.1.

Validation of the abrasion test using four 0% nanocomposite membranes was conducted and the results are shown in Figure 3-4.

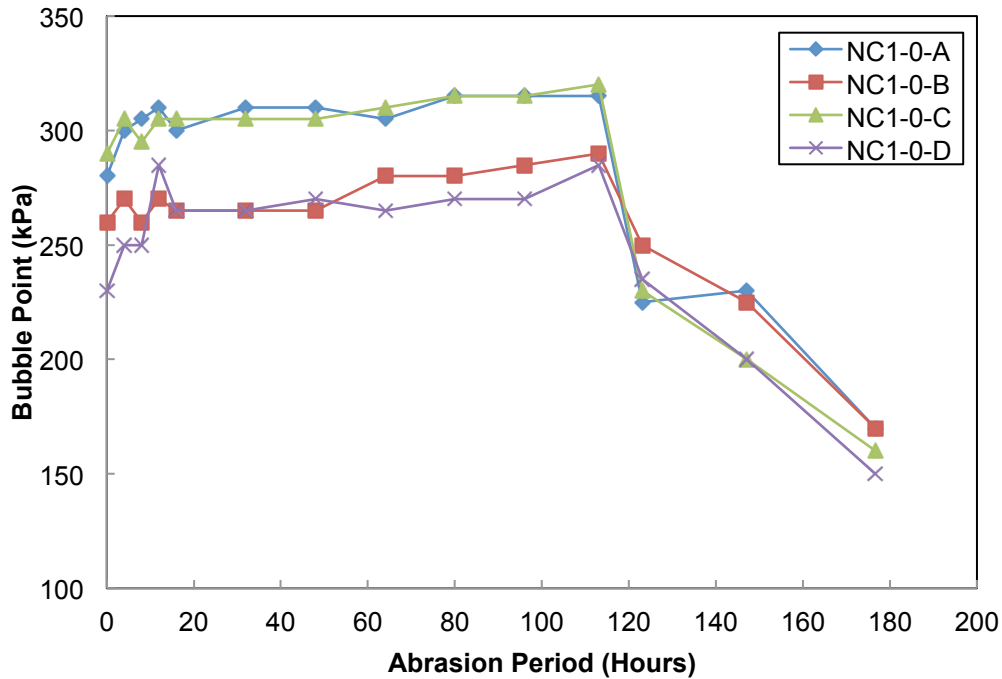


Figure 3-4. Bubble point of the membranes during the initial abrasion testing to confirm the abrasion testing experiment used in this work

It was observed that the bubble point of all four membranes dropped more than 20% after 120 hours (5 days) of abrasion, indicating that the membranes had been subjected to abrasive wear. A sudden decrease of bubble point occurred in the same period (between 113 and 123 hours) for all four membranes, demonstrating that the testing setup was reliable and repeatable. The initial testing also helped to decide how often the bubble point measurement should be taken. Since the bubble point had remained stable for the first 100 hours, bubble point testing every 20-25 hours was adopted for subsequent testing.

3.4.9 Membrane permeation testing

For flat sheet membranes, filtration testing was carried out using a Sterlitech CF042 membrane cell. This is a laboratory scale cross flow filtration unit. The active membrane area was 42 cm² and pure water flux of the membranes was measured at

175 kPa trans-membrane pressure (TMP). For hollow fibre membranes, double fibres of ~ 40cm (total length) were first potted in a 6.5 cm piece of nylon tubing with epoxy resin. Pure water flux of the membranes was measured at 100 kPa TMP. The active membrane area was determined using the outer circumference calculated from images taken by SEM and the length of fibre used in the test. The average length of fibre used was about 40 cm. Milli-Q water was used as the filtration medium. Pure water permeability (P_w) was determined using Equation (6),

$$P_w = \frac{Q}{A \cdot \Delta t \cdot p} \quad (6)$$

where Q (L) is the amount of water collected as permeate, A (m^2) is the membrane area, Δt (h) was the sampling time and p (bar) is the TMP. Three measurements were taken and the average determined.

3.4.10 Fouling resistance testing

Membrane fouling studies on single hollow fibre membrane were conducted with extended operation and periodic backwashing. The setup was similar to the method presented in previous work [125]. The membrane modules were first prepared by inserting a single hollow fibre membrane of 60 cm length folded at the mid-point into transparent polyurethane tubing. The open ends of the membrane were potted at one end of the tubing with an epoxy resin such that water entered the outer surface of the membrane and exited from the lumen. Figure 3-5 shows the schematic diagram of the filtration unit setup. A data acquisition and control system was used to regulate the solenoid valves (labelled as 1 to 5 in Figure 3-5) for the filtration and backwash sequences, as well as for continuous recording of pressure. A low flow positive displacement pump from Fluid Meter Instruments (model no. 348745) was used to provide constant flux (50 L/ m^2 h) throughout the experiments. Each filtration cycle included 30 minutes of filtration followed by a 5-minute transition period where 60 seconds of backwash occurred within it. Liquid backwashing was performed via pressurized Milli-Q water at 1.4 bars and a series of valves, in order to flush off the foulants from the membrane surface. The filtration cycle repeated for 24 hours and TMP was continuously measured every 1 s by a pressure transducer ($\pm 0.1\%$, -1 to 9 bar) and 1 minute average data were recorded. The increase of pressure with time was a measure of fouling rate of the membrane.

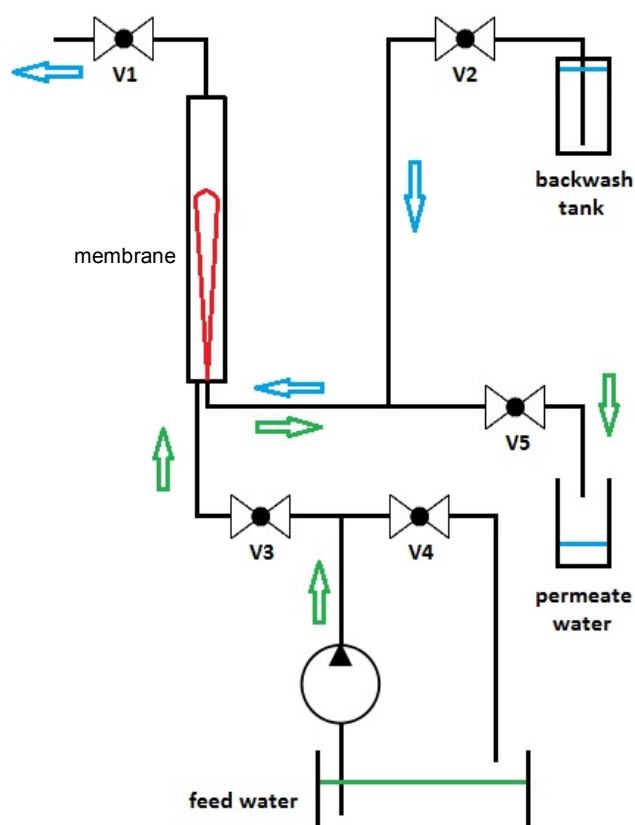


Figure 3-5. Schematic diagram of dead-end hollow fibre filtration unit (numbers refer to solenoid valves).

The membranes were tested with two foulant solutions made up with Milli-Q water. Bovine serum albumin (BSA) and sodium alginate were used as foulants, representing proteins and polysaccharides respectively which are common NOMs (natural organic matters) causing organic fouling. As pure water provides unusual results and has the potential for dewetting of the membrane during backwash, salt (sodium chloride (NaCl) and calcium chloride (CaCl₂)) was added to the foulant solutions as a background electrolyte and naturally occurring multivalent cations [126]. The detailed composition of each solution is listed in Table 3-7.

Table 3-7. Composition of the foulant solutions

Foulant solution no.	Components
1	100 ppm BSA, 450 ppm NaCl, 50 ppm CaCl ₂
2	100 ppm sodium alginate, 450 ppm NaCl, 50 ppm CaCl ₂

4. Investigation of effective methodology to disperse nanoclays

This chapter evaluates four different approaches to disperse nanoclay in solvent – ultrasonication, planetary centrifugal mixer, overhead stirrer and high shear fluid processing. This study was undertaken to determine the most effective way to disperse nanoparticles in dope for subsequent membrane casting. The dispersions were characterized for particle size and particle size distribution. The details of the experimental setup are described in Section 3.2.

Following this, membranes cast with different dispersion techniques were evaluated for nanoclay dispersion within the membranes. As mentioned in Section 2.3.3, nanoclay platelets can be phase separated, intercalated or exfoliated in the polymer matrix [110]. Ideally, nanoclay platelets would swell up in the solvent and be separated with the dispersion techniques. Upon mixing the nanoclay dispersion with the polymer, the individual platelets distribute randomly in the polymer matrix (exfoliation). TEM and SAXS were used to study the impact of various dispersion techniques on nanoclay morphology in the membranes. Membrane structure and mechanical properties were also examined.

4.1. Results and Discussion

4.1.1 Dispersion with conventional methods

As-packed dry nanoclay powder exists as large clusters due to adhesive forces between the particles. Using Cloisite[®] 30B as an example, the supplier's product data sheet [127] indicates the typical dry particle sizes as follow: 10% less than 2 μm , 50% less than 6 μm and 90% less than 13 μm . This is also verified by the SEM image as shown in Figure 4-1 as the dry particles appeared as lumps of differing sizes, all greater than 1 μm . So in order to disperse as nanoparticles into functional membranes, a technique to first disperse the clay particles into smaller size was needed.

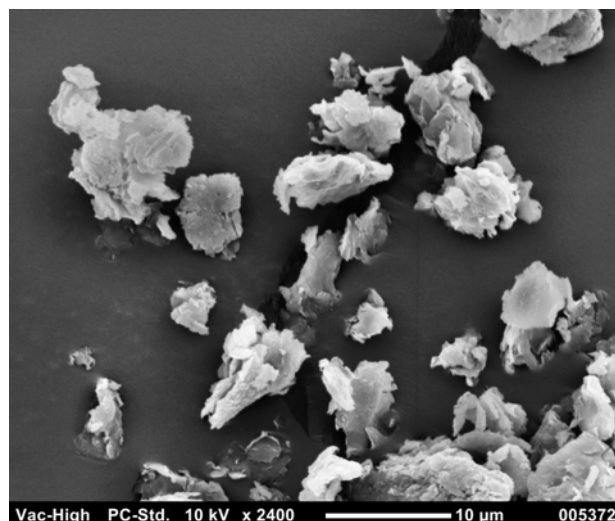


Figure 4-1. SEM image of dry Cloisite[®] 30B particles

Ultrasonication [56, 128] and mechanical stirring [83, 108] are common ways to provide the energy necessary to disperse nanoparticles in solvents for membrane fabrication prior to NIPS processing. To explore the effectiveness of these methods, the size and size distribution of Cloisite[®] 30B/NMP dispersions using ultrasonication, planetary centrifugal mixer, and overhead stirrer was measured periodically over a given total mixing time. Figure 4-2 shows the Z-average size, which is the intensity-weighted mean diameter derived from the cumulants analysis of the nanoparticles versus the mixing time with three different dispersion methods. Although the Z-average size only reflects the actual particle size if the sample is monomodal, spherical and monodisperse, for the same material it was able to show all three dispersion methods reduced the particle size at different rates. It also resulted in different particle sizes at the end of the test when the mixing was stopped due to an equilibrium being reached. All three methods demonstrated the most rapid change in particle size in the first hour of operation and the size gradually settled upon further operation. Ultrasonication resulted in the smallest final average particle size of 273 nm (2 hours), followed by planetary centrifugal mixer (Thinky Mixer) of 366 nm (4 hours) and overhead stirrer of 480 nm (12 hours).

Ultrasonication appeared to be the best method in terms of dispersing the particles to the smallest size within the shortest period of time. The vibration produced by ultrasound appeared to be more efficient and effective to break apart the particles than physical force imposed by centrifugal mixer and overhead stirrer. Ultrasonication also had higher operating frequency than the mixing methods (50 kHz vs 2000 rpm and 200 rpm) which helped separating the particle clusters more quickly. The smaller size

achieved by the Thinky Mixer than the overhead stirrer was likely because of the higher mixing speed applied that produced higher shear forces. A key question for this test was whether a lower energy, lower cost mixing technique like overhead stirring, could achieve the same particle size over a longer time. Prolonged stirring may be a more economical way to disperse the nanoparticles, but gradual breakdown of size after 12 hours reduced the particle size to only about 480 nm, which was still larger than the size achieved after 2 hours with the ultrasonication method (273 nm).

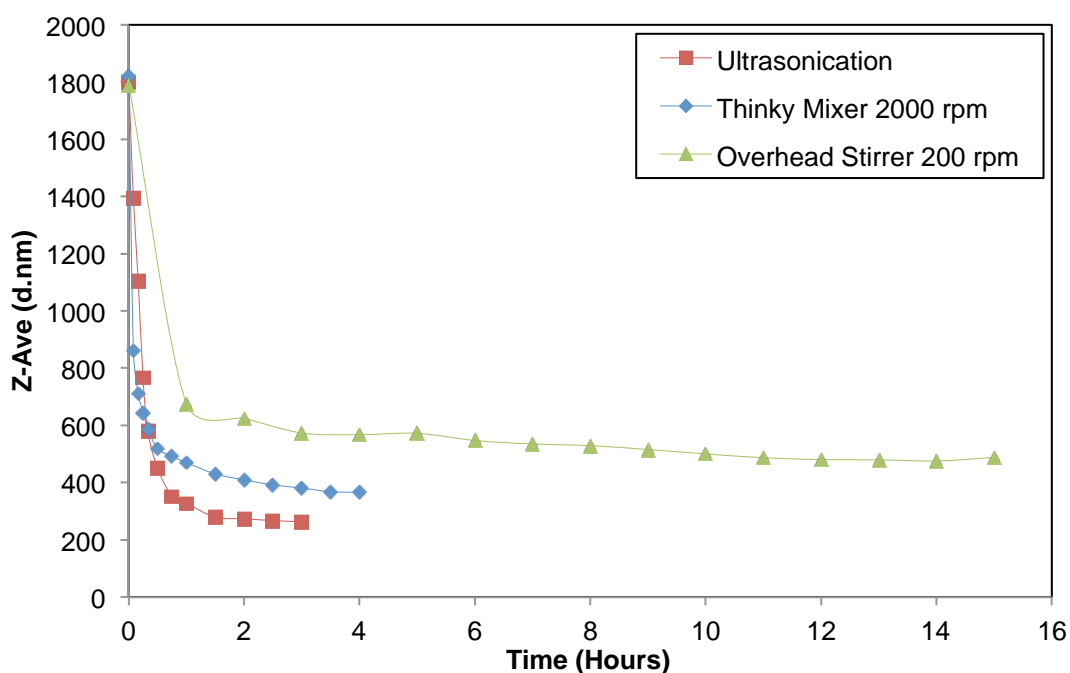


Figure 4-2. Z-average particle size of Cloisite® 30B dispersed in NMP vs mixing time using various mixing techniques.

Figure 4-3 shows the size distribution by intensity of Cloisite® 30B using ultrasonication as the dispersion method at various time intervals. Initially (t = 0 hours), the size distribution shows a major peak at 3090 nm and a minor peak at 295 nm. The major peak has a narrow size distribution which implies the initial particle size was uniform and the majority of the particles remained at the micron scale. The range of the major peak was from 900 nm to 6500 nm which is slightly smaller than the dry particle size (Figure 4-1), showing that nanoclay was scattered to smaller clusters once it was added to the solvent. With ultrasonication, the distribution became monomodal and widened as smaller particles started breaking off. As time progressed, the size distribution then narrowed again as the larger particles had mostly been broken apart to the uniform sub- particles and became more uniform. It was also observed that

ultrasonication for one hour gave the highest dispersion rate of the particles. After one hour the particle size decreased slowly and eventually remained at about 300 nm.

As mentioned in Section 2.3.2.3, at the molecular level, nanoclay has a platelet structure with each platelet having thickness of about 1 nm and several hundreds of nm for its width and length. Meanwhile the particle size measured by the particle sizer refers to the nanoclay cluster size rather than the size of individual platelet. With ultrasonication of two hours, the Z-average size of Cloisite® 30B was reduced from 1800 nm to 273 nm. Assuming the d-spacing (1.85 nm) [127] remained unchanged, a simple ratio of particle diameter to d-spacing shows that the nanoclay cluster size was reduced from about 973 to 148 platelets in width through the particle cluster. Therefore, there are still many agglomerated platelets indicating smaller particles are achievable.

One approach to reduce particle size further is to increase mixing power. Prior work on dispersing alumina in aqueous suspensions by Nguyen et al [129] has shown that increasing the power input or the vibration amplitude of ultrasonication did not break up the nanoparticle clusters further. As such, in order to further disperse the nanoclay, an alternative method was needed. A high shear mixing process with microfluidizer was then used.

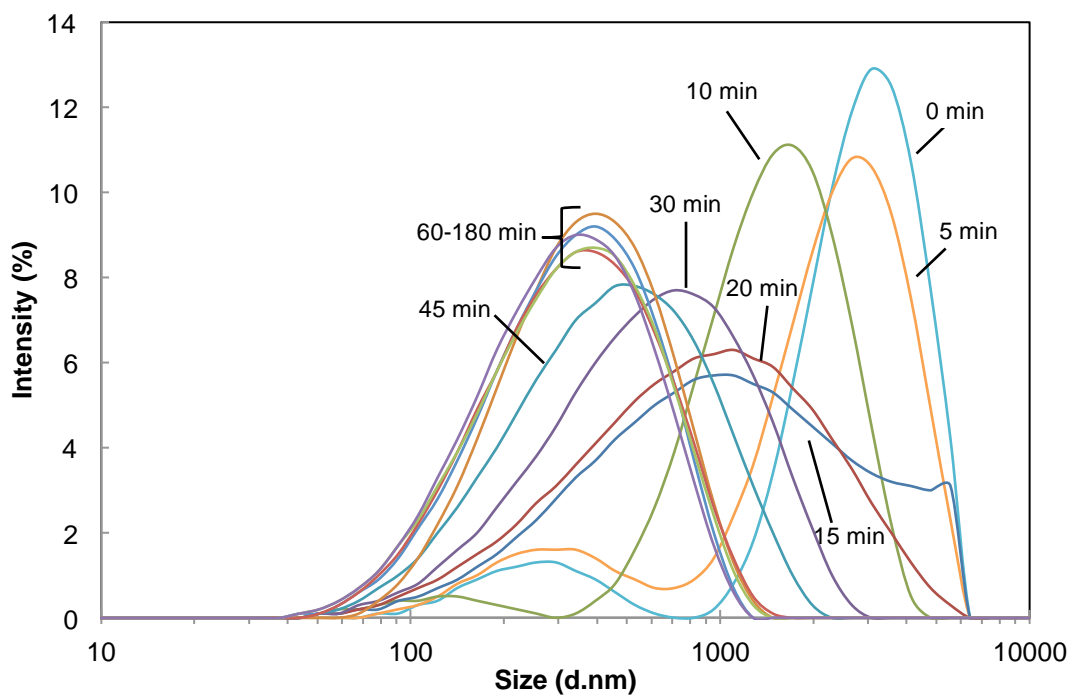


Figure 4-3. Size distribution by intensity of Cloisite® 30B dispersed with ultrasonication at various time intervals.

4.1.2 Dispersion with microfluidizer

While microfluidizer, a high shear fluid processor, has been used in various disciplines including pharmaceutical, biotechnology and food industries to reduce particle size as described in Section 2.3.3, its effect on dispersing nanoclay has yet to be explored. In this section, a microfluidizer was used to disperse Cloisite[®] 30B and Nanomer[®] I.30E and the particle size and size distribution diagram after each dispersion cycle is presented in Figure 4-4. From the size distribution diagrams in Figure 4-4(a) and (b), the effect of high shear dispersion could be observed after just one dispersion cycle, where the size distribution for both nanoclays changed from multimodal to unimodal. The peak position gradually reduced, while its width became narrower after each dispersion cycle. This shows that uniformly sized small particles were being formed.

From Figure 4-4(c), the initial value of Cloisite[®] 30B was similar to the one-hour ultrasonicated value presented in Figure 4-2 as ultrasonication was performed initially in order to mix the nanoparticles in the NMP prior to loading into the microfluidizer. It is noted that Nanomer[®] I.30E had a much larger initial Z-average size (2883 nm vs 345 nm) showing that dispersion using ultrasonication was not very effective. Comparing the organic modifier of both nanoclays (Table 3-2), Cloisite[®] 30B has two hydroxyl groups while Nanomer[®] I.30E has none. Nanomer[®] I.30E instead has one tallow group. The smaller size of 30B was likely due to greater affinity to the solvent once it was dispersed, as NMP is a polar solvent. The Z-average size of Cloisite[®] 30B was reduced from an initial 345 nm to 231 nm after 10 cycles of microfluidization. Therefore, the microfluidizer can reduce particle size by a further 33%. For Nanomer[®] I.30E which has much stronger affinity among the clay particles, the effect of using microfluidizer was even more significant. The majority of the particle size reduction occurred after the first cycle, with size decreasing from 2883 nm to 1046 nm. From the sixth to tenth cycle, there was no further reduction and the final size was about 680 nm, which was 76% smaller than initial size (one hour of ultrasonication).

This shows that microfluidizer dispersed the nanoclay even further than ultrasonication, which was the best of the three conventional methods. It was likely the shear force had higher energy than ultrasound to break apart the nanoparticles. Figure 4-5 shows the size distribution of Cloisite[®] 30B using the optimal condition of all dispersion techniques investigated. Microfluidizer showed the smallest particle size with narrowest size distribution followed by ultrasonication, planetary centrifugal mixing

(Thinky mixer) and overhead stirring. This once again confirmed that the microfluidizer was the best technique for nanoclay dispersion.

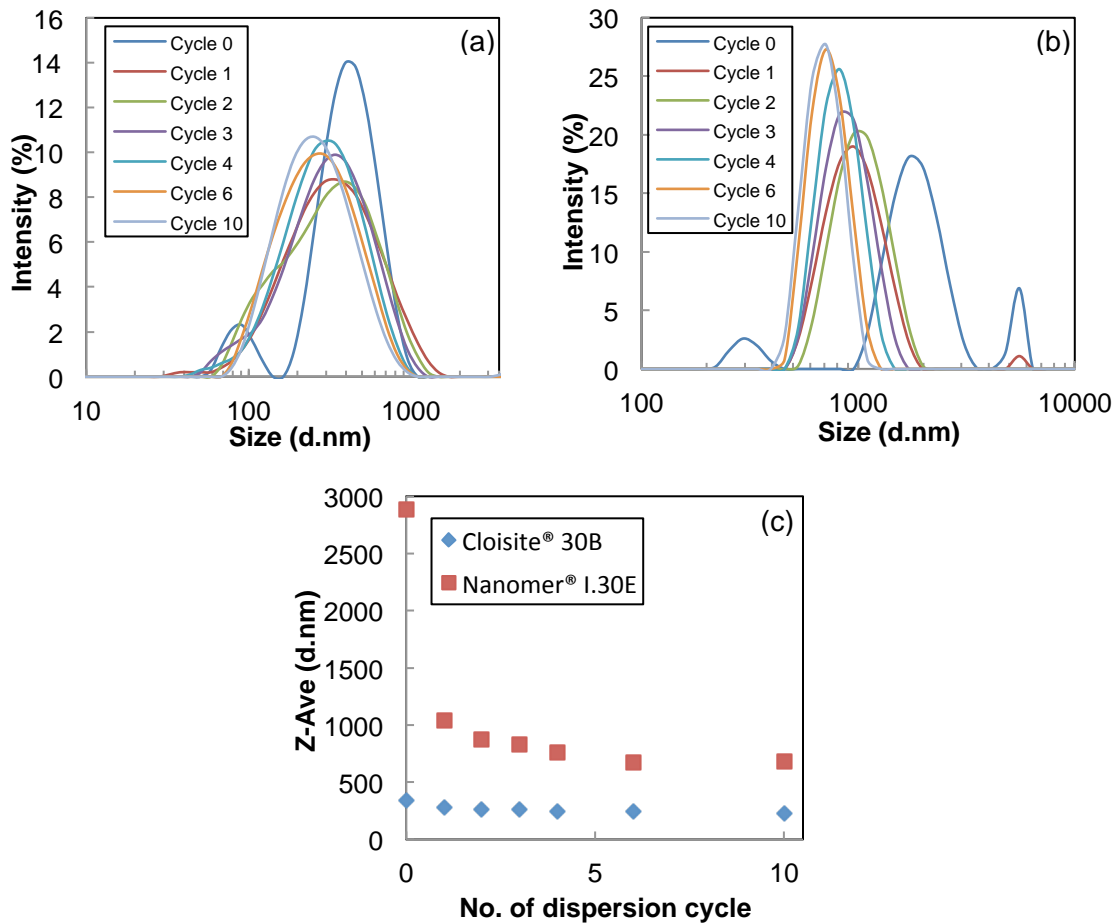


Figure 4-4. Size distribution by intensity of Cloisite® 30B (a) and Nanomer® I.30E (b) dispersed in NMP with microfluidizer and Z-average particle size of the nanoclays (c).

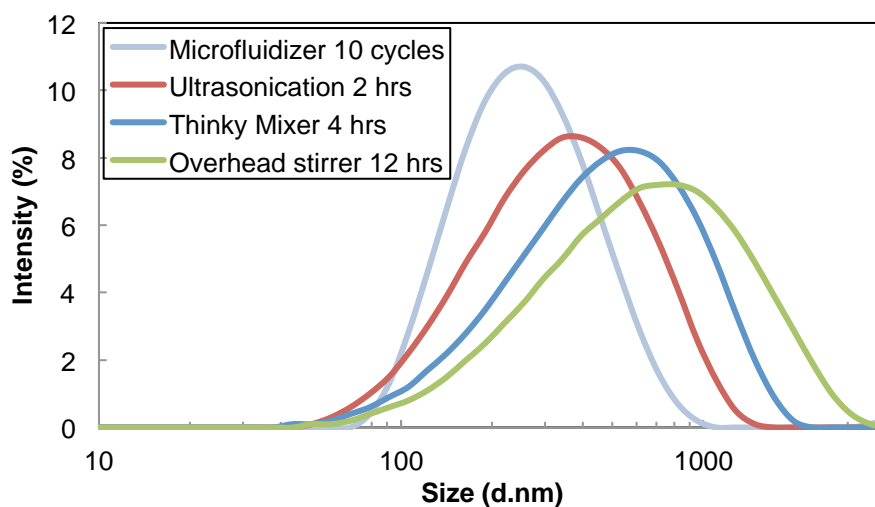


Figure 4-5. Size distribution by intensity of Cloisite® 30B using different dispersion methods.

4.1.2.1 Stability of microfluidized dispersion

After at least 12 days of stagnancy, the particle size of the Cloisite[®] 30B and Nanomer[®] I.30E microfluidized dispersions were measured again. As shown in Figure 4-6, the Z-average size of Cloisite[®] 30B was found to be 235 nm which was similar to the particle size immediately following dispersion (231 nm). This showed that the Cloisite[®] 30B dispersion was very stable as no apparent re-agglomeration had occurred. For Nanomer[®] I.30E, the Z-average size after stagnancy increased from 680 nm to 1261 nm, indicating some degree of re-agglomeration occurred. This was likely due to the stronger affinity between I.30E nanoparticles in NMP, but despite the re-agglomeration the size was still considerably smaller than that before microfluidizing (2883 nm).

It was also interesting to note that upon ultrasonication of these stagnant dispersions, especially the Nanomer[®] I.30E dispersion, the cluster size was reinstated to that as before the stagnant state. With as little as 30 minutes of ultrasonication, the Z-average size of Nanomer[®] I.30E dispersion reduced to 608 nm which was even lower than that after 10 cycles of microfluidization. With ultrasonication of up to two hours, the size was further reduced to 555 nm. It was possible that microfluidization initially broke up the more strongly bound particles but the re-agglomerated particles were less strongly bound together and the looser flocs could be easily broken apart again by a simple ultrasonication step. The effect of using ultrasonication to redisperse Cloisite[®] 30B was not as significant possibly because the cluster size of Cloisite[®] 30B was already at its lower limit (about 124 platelets in width per cluster based on the simple ratio mentioned in Section 4.1.1).

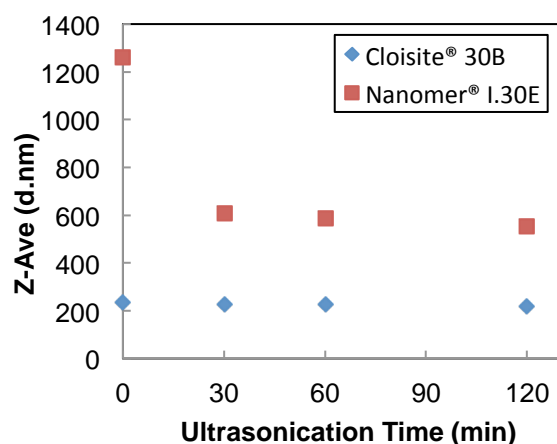


Figure 4-6. Z-average particle size of microfluidized nanoclay particles redispersed by ultrasonication after 12 days or more of stagnation

4.1.3 Nanoclay distribution in membrane

While it would be ideal to study the dispersion of clay particles in the casting solution as well, it was not feasible in this situation. Upon diluting the dope to the concentration required by the particle sizer, temperature would drop below the original dope temperature of 90°C, which causes PVDF to precipitate. Nevertheless, nanocomposite membranes were cast using ultrasonication and microfluidization respectively to explore the nanoclay distribution at both the macro and molecular levels with SEM/EDS, SAXS and TEM. PVDF membranes with 5 wt% of either Cloisite[®] 30B or Nanomer[®] I.30E in the initial dope were fabricated according to Section 3.3.1 and the composition of the synthesis solution is listed in Table 4-1. The membranes were also tested for their mechanical properties to compare the effect of using different dispersion techniques.

Table 4-1. Composition of synthesis solutions and dispersion method

Membranes	Nanoclay type	PVDF (wt%)	NMP (wt%)	Nanoclay (wt%, by weight of PVDF)	Dispersion method
PVDF	-	15	85	0	-
PVDF/30B-U	Cloisite [®] 30B	14.25	85	5	Ultrasonication 2 hours
PVDF/30B-M	Cloisite [®] 30B	14.25	85	5	Ultrasonication 1 hour & microfluidizer 10 cycles
PVDF/I30E-U	Nanomer [®] I.30E	14.25	85	5	Ultrasonication 2 hours
PVDF/I30E-M	Nanomer [®] I.30E	14.25	85	5	Ultrasonication 1 hour & microfluidizer 10 cycles

4.1.3.1 SAXS

The basal spacing (d_{001}) of the nanoclay and the nanocomposite membranes were measured using the SAXS beam line in the Australian Synchrotron. From the SAXS pattern shown in Figure 4-7(a), the Q-range for Cloisite[®] 30B was 0.34 \AA^{-1} which was equivalent to nominal d_{001} spacing of 1.85 nm. This value was the same (1.85 nm) as the manufacturer's data listed in Table 3-2. While the neat PVDF membrane showed no peak, both PVDF/30B-U and PVDF/30B-M displayed similar patterns with a possible peak near 0.35 \AA^{-1} ($d_{001}=1.80 \text{ nm}$). Likewise in Figure 4-7(b), the Q-range for

Nanomer[®] I.30E was 0.30 \AA^{-1} , which was equivalent to nominal d_{001} spacing of 2.10 nm. This value was within the range (1.8-2.2 nm) of the manufacturer's data listed in Table 3-2. Both PVDF/I30E-U and PVDF/I30E-M displayed similar patterns with a possible peak near 0.36 \AA^{-1} ($d_{001}=1.75 \text{ nm}$). In both types of nanocomposite membranes, the decrease in the basal spacing suggested the nanoclay silicate layers remained phase separated regardless of the dispersion method. This can be confirmed with TEM imaging.

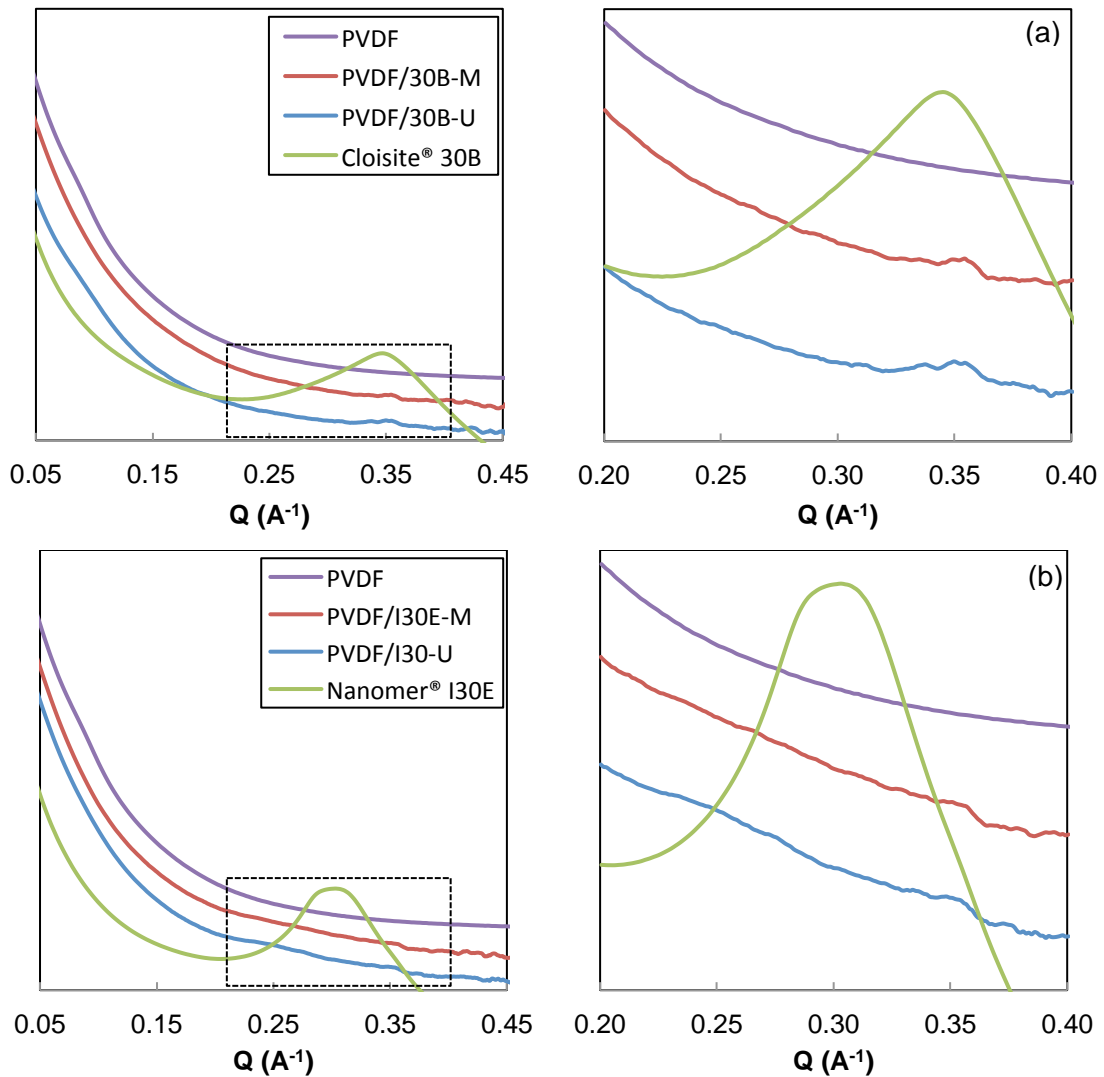


Figure 4-7. SAXS patterns of (a) PVDF/30B membranes & Cloisite[®] 30B powder and (b) PVDF/I30E membranes and Nanomer[®] I.30E powder.

4.1.3.2 TEM

Figure 4-8 shows the TEM image of PVDF/I30E-M membrane. The dark hair-like lines could be attributed to the individual silicate platelets of the nanoclay. As confirmed by the image, the platelets were still closely packed together. By placing the 20 nm scale bar (white lines in Figure 4-8) at various locations on the image, an average of 9 layers was counted across this length indicating the d-spacing was about 2.2 nm. This value appeared to be slightly larger than that measured by SAXS (1.75 nm). The TEM measurements were taken from an area in which the platelets were distinguishable and this may have skewed the result to a larger value. Nevertheless, the d-spacing measured with TEM was not greater than the original nanoclay d-spacing (1.8-2.2 nm) and this affirmed the SAXS results that Nanomer[®] I.30E had a phase separated morphology within the PVDF matrix.

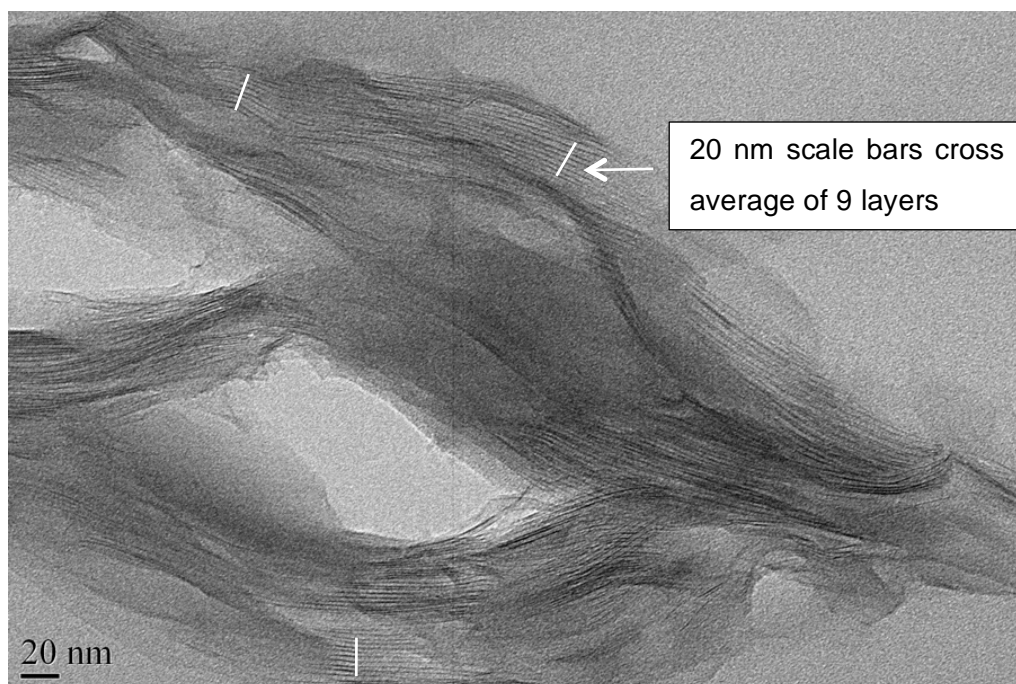


Figure 4-8. TEM image of PVDF/I30E-M membrane

In theory, and as described in Section 2.3.3, nanoclay can be swollen in solvent and dispersed with shear force. Polymer solution is then added to intercalate or exfoliate between the nanoclay layers and the position of the clay platelets are fixed in the polymer matrix as the polymer precipitates in a non-solvent [103]. While other researchers [83, 113] were able to produce intercalated or exfoliated PVDF/nanoclay nanocomposites using this technique, it was not achieved in this study. One possible

reason may be due to differences between casting parameters such as solvent and polymer concentration. Also, as the dispersion of nanoclay using either ultrasonication or microfluidizer was not done with the presence of polymer, there may be chance that the nanoclay platelets re-agglomerated when mixing the nanoclay dispersion with the PVDF solution with an overhead stirrer. Section 5.2.4 will further explore the relationship between nanoclay morphology and casting techniques. Although neither technique exfoliated the nanoclay platelets, the difference in cluster size could still possibly influence other membrane properties.

4.1.3.3 SEM/EDS

Figure 4-9 displays the quench contact side surface morphology of the PVDF/I30E membranes using different dispersion methods and the corresponding EDS images of silicon mapping. The surface of the both membranes appeared to be porous and the average pore size was found to be $0.96 \pm 0.21 \mu\text{m}$ and $0.82 \pm 0.25 \mu\text{m}$ for PVDF/I30E-U and PVDF/I30E-M respectively. This showed that membranes prepared following different dispersion methods could impact the pore size and the pore size distribution.

Both membranes appeared to have nanoclay agglomerates as shown in Figure 4-9, with smaller agglomerates shown on the membrane using microfluidizer as the dispersion method. Based on observation of the EDS maps, the average cluster size of PVDF/I30E-M and PVDF/I30E-U was 705 nm and 1600 nm respectively. These values were comparable to the Z-average size measured by the particle sizer (685 nm vs 1500 nm) shown in Figure 4-4(c). This shows that a high shear hydrodynamic dispersion process is able to more finely disperse the nanoclay than ultrasonication which is commonly used for dispersing nanoparticles in solvent for membrane fabrication [56, 128]. This also confirmed the result determined by the particle sizer – particles dispersed by microfluidizer had smaller size than that by ultrasonication (Section 4.1.2).

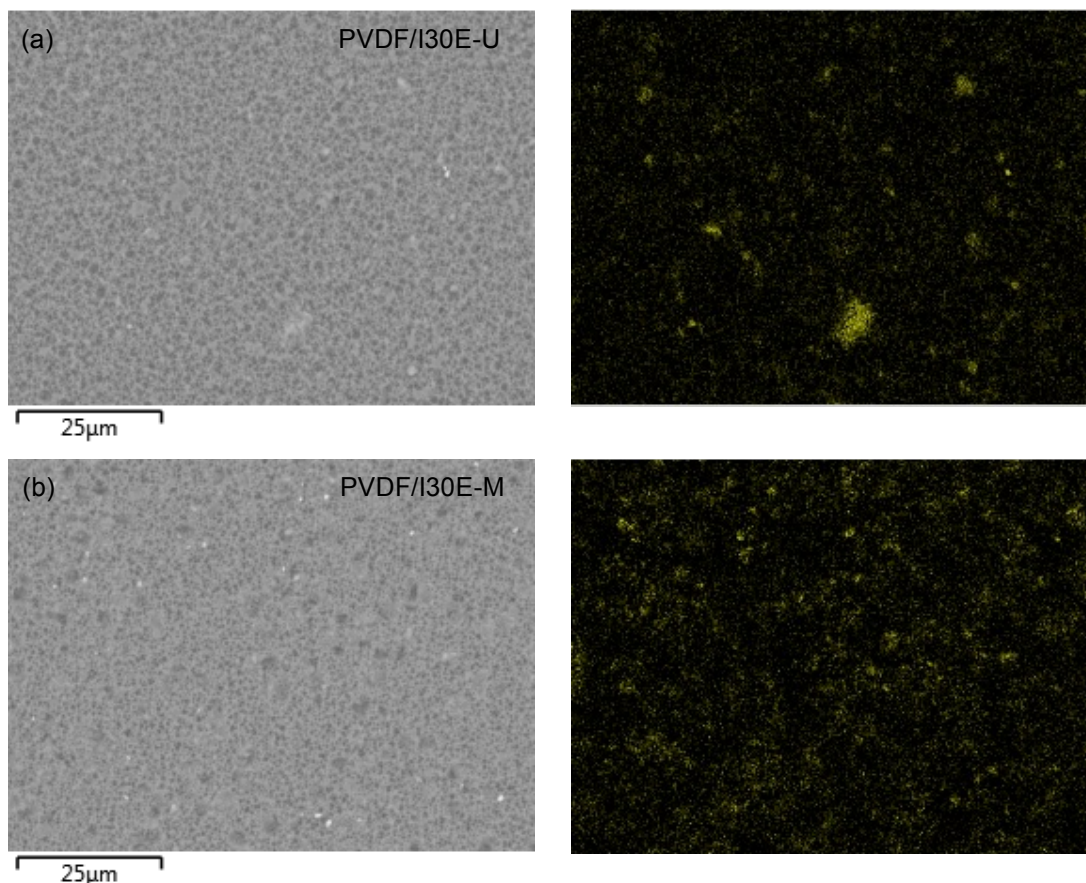


Figure 4-9. Backscattering SEM and Si mapping images using EDS of PVDF/I30E 5% membrane quench side surface dispersed by (a) ultrasonication and (b) microfluidizer.

While the micro-morphology of nanoclay as shown by SAXS was not altered by using different dispersion techniques, dispersing nanoclay with the microfluidizer brought about a more homogenous membrane which is considered valuable for enhanced membrane properties and performance [26].

4.1.3.4 Mechanical properties

The test results of mechanical properties including tensile strength, elongation at maximum load and Young's modulus are listed in Table 4-2. It was observed that the PVDF/I30E-M membrane exhibited similar tensile strength and elongation at max load to the neat PVDF membrane with an increase in Young's modulus from 46 MPa to 70 MPa. This indicated the introduction of nanoclay provided extra stiffness to the polymer matrix while maintaining tensile strength and ductility. It was noted that the Young's modulus of PVDF/I30E-U was considerably lower than the other two membranes. This was likely due to the large agglomerates present in the membrane

as shown in Figure 4-9(a), which weakened the membrane mechanical properties. With this, nanocomposite membranes prepared using novel microfluidization was justified by showing higher uniformity and improved mechanical properties than those prepared with conventional dispersion technique (ultrasonication).

Table 4-2. Mechanical properties of membranes

Membrane	Tensile strength (MPa)	Elongation at max load (%)	Young's modulus (MPa)
PVDF	3.6 ± 0.5	62 ± 7	46 ± 3
PVDF/I30E-U	3.8 ± 0.3	50 ± 6	37 ± 1
PVDF/I30E-M	3.7 ± 0.1	56 ± 9	70 ± 6

4.2. Conclusions

Cloisite[®] 30B and Nanomer[®] I.30E were dispersed in NMP with various methods including overhead mixing, ultrasonication, planetary mixing and high shear mixing. For 30B the first three techniques were tested, and ultrasonication was the fastest and most effective in dispersing the clay into the smallest particle size within the shortest mixing time given its highest operating frequency. After two hours of ultrasonication, the particle size was found to be 265 nm. Further dispersion of nanoclay using the microfluidizer, a high shear dispersion process, further reduced the particle size to 231 nm after ten cycles. Reinstating the small particle size of microfluidized dispersion after nearly two weeks of stagnation time was possible by 30 minutes of ultrasonication. While dispersing nanoclay with the microfluidizer did not exfoliate the nanoclay platelets, it formed more homogeneous membranes with improved mechanical properties compared to neat PVDF membranes and those prepared with ultrasonication. The key parameters of the membranes prepared by different dispersion methods are summarized in Table 4-3.

Although the microfluidizer has proven to be a more powerful way to disperse particles, ultrasonication still appeared to effectively disperse nanoclays to give good quality membrane films. As such, the following chapter on optimising membrane fabrication chemistry and for retention and durability studies used ultrasonication for two hours to disperse nanoclay. However, the optimal dispersion technique using combined ultrasonication and high shear mixing (microfluidizer) was used for the

optimised fabrication approach applied to hollow fibres, which are the main membrane type to be studied for enhanced durability in this work.

Table 4-3. Summary of key parameters of membranes prepared by different dispersion methods.

Membrane	Dispersion method	d_{001} spacing of I30E (nm)	Nanoclay morphology	Average nanoclay cluster size by EDS (nm)	Tensile strength (MPa)	Elongation at max load (%)	Young's modulus (MPa)
PVDF	-	-	-	-	3.6 ± 0.5	62 ± 7	46 ± 3
PVDF/I30E-U	Ultrasonication 2 hours	1.75	Phase separated	1600	3.8 ± 0.3	50 ± 6	37 ± 1
	Ultrasonication 1 hour & microfluidizer 10 cycles	1.75	Phase separated	705	3.7 ± 0.1	56 ± 9	70 ± 6
PVDF/I30E-M	microfluidizer 10 cycles				3.7 ± 0.1	56 ± 9	70 ± 6

5. Preparation and characterization of PVDF/nanoclay nanocomposite flat sheet membranes for material properties and durability assessment

In this chapter, nanocomposite PVDF/Cloisite[®] 15A flat sheet membranes were fabricated and characterized to determine the concentration of inorganic nanomaterials retained in the membrane, as well as the thermal properties, morphology, mechanical strength, abrasion resistance and water flux. Flat sheet membranes were fabricated as a preliminary study of the effect of nanoclay on abrasion resistance utilising a standard tribology technique to measure abrasive wear. Cloisite[®] 15A was chosen based on the literature review in Chapter 2.

5.1. Membrane preparation and characterization

Pure PVDF and PVDF/Cloisite[®] 15A nanocomposite membranes (1 wt%, 3wt% and 5 wt% Cloisite[®] 15A by weight of PVDF) were prepared by phase inversion with the procedures described in Section 3.3.1 using ultrasonication to disperse nanoclay. The composition of the synthesis solution is listed in Table 5-1.

Table 5-1. Composition of synthesis solutions

Membranes	PVDF (wt%)	NMP (wt%)	Cloisite [®] 15A (wt%, by weight of PVDF)
PVDF/15A-0	15	85	0
PVDF/15A-1	14.85	85	1
PVDF/15A-2	14.55	85	3
PVDF/15A-3	14.25	85	5

The fabricated membranes were characterized by TGA, FTIR, SEM/EDS, SAXS, water permeability, mechanical testing and abrasion testing with a standard tribology technique with sand paper. The detailed setup of these techniques is described in Chapter 3.

5.2. Results and Discussion

5.2.1 TGA

Figure 5-1 presents the TGA curves of Cloisite® 15A and the four various membranes. All of the membranes exhibited a two-step thermal decomposition that was attributed to break down of the polymer. The first degradation stage between 350°C to 500°C was due to chain-stripping of the polymer backbone [130]. The release of hydrogen and fluoride from the PVDF is known to lead to the formation of volatile hydrogen fluoride [131]. The second stage, which occurred after 500°C, corresponded to the burn off of the carbonaceous residue [130]. The decomposition curves would be mostly associated with the PVDF material because Cloisite® 15A cannot contribute to more than 5% of the total material mass.

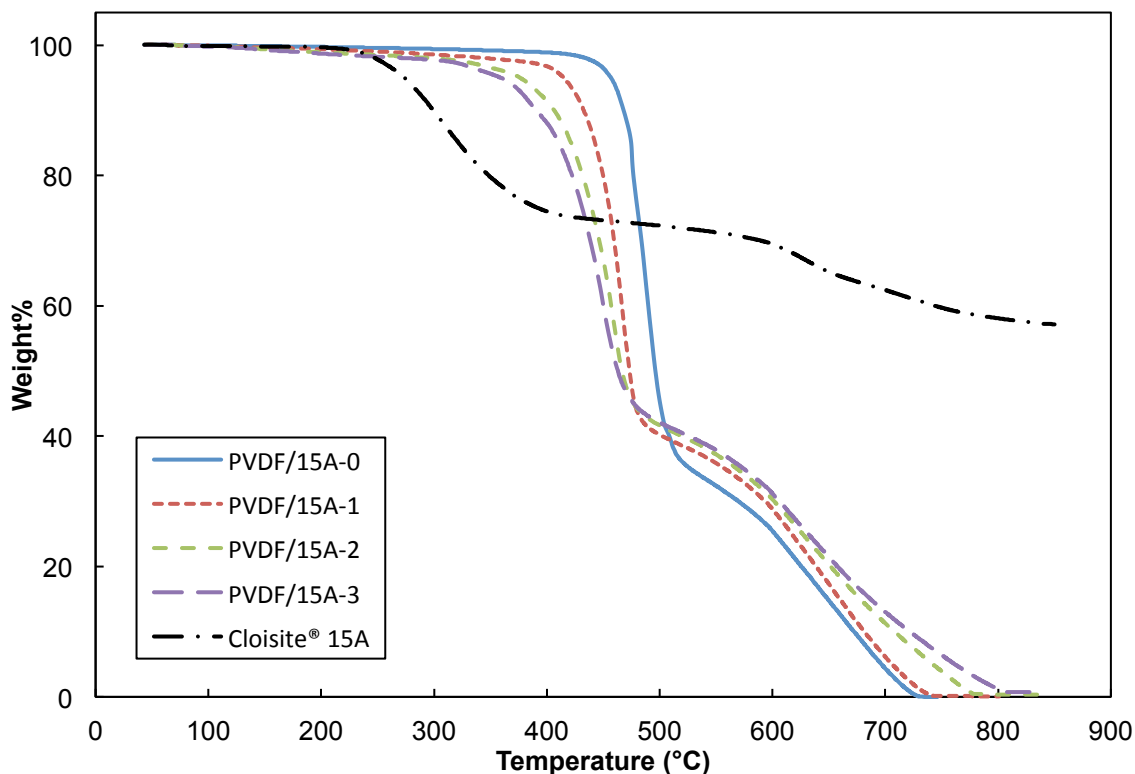


Figure 5-1. TGA thermograms of PVDF composite membranes and Cloisite® 15A

As the nanoclay loading increases, the temperature at which the first stage of decomposition commences reduces. Li and Kim [132] also noted this weakening in thermal stability in their PVDF/modified clay nanocomposite membranes which have lower activation energy compared to pure PVDF membrane. Small amounts of additives, including silicate and titanate, are able to catalyse the thermal decomposition

rate of PVDF [87]. The organic component of Cloisite® 15A started to break down at a lower temperature than pure PVDF (i.e. 250°C and 450°C respectively). Despite the small loading in the membrane, the presence of Cloisite® 15A caused the decomposition of the composite PVDF/nanoclay membrane to occur at a lower temperature. Although the composite membranes showed poorer thermal resistance, it should not impact operation adversely as UF/MF does not run at such high temperature.

The second weight loss step, starting from 450°C to 500°C and ending between 700°C and 800°C, ultimately yields the residual mass that cannot further decompose, which is interpreted as the inorganic component of the materials. It was found that 57% of Cloisite® 15A was not combusted after TGA, implying this is the inorganic component of the original nanoclay. This value matches with the weight loss on ignition stated on the supplier’s product data sheet of the nanoclay [133]. In all cases, the nanocomposite membranes contained a non-combustible residue that was attributed to the inorganic component of the added nanoclay and increased with nanoclay loading. Although it is not seen clearly on Figure 5-1, it was observed visually in the pan and measured by the TGA. The results are listed in Table 5-2 and compared against the original inorganic loading calculated based on the original nanoclay loading in the synthesis solution and the TGA data of the nanoclay.

Table 5-2. Comparison between original and actual inorganic loading

Material	Original / supplier inorganic loading %	Inorganic residue % (weight % after TGA)	% of nanoclay retained
PVDF/15A-0	0	0.0	-
PVDF/15A-1	0.6	0.1	17
PVDF/15A-2	1.7	0.3	17
PVDF/15A-3	2.9	0.7	24
Cloisite® 15A	57	57	-

Table 5-2 shows a slight increase in the residual weight percentage which corresponds to an increase in the nanoclay loading. It is observed that the nanoclay content in the final product detected by TGA was only about one fifth of the initial concentration in the dope for all three nanocomposite membranes. This implies some loss during membrane formation and it was likely to occur during the phase inversion process.

5.2.2 Effect of nanoclay on membrane crystal structure

The FTIR spectra of PVDF and the nanocomposite membranes are shown in Figure 5-2. The spectra exhibit strong peaks that are associated with different crystalline phases of PVDF. Major peaks were observed at 763 cm^{-1} and 796 cm^{-1} corresponding to the α -phase of PVDF, as well as at 840 cm^{-1} corresponding to the β -phase of PVDF [53, 122]. The α -phase peak intensity decreased in tandem with an increase in the β -phase peak for the nanocomposite membrane samples. This was attributed to a change in PVDF crystal phases during membrane formation, and previous studies have shown that the incorporation of nanoclay can stabilize the formation of β -phase PVDF [53, 90, 109, 113].

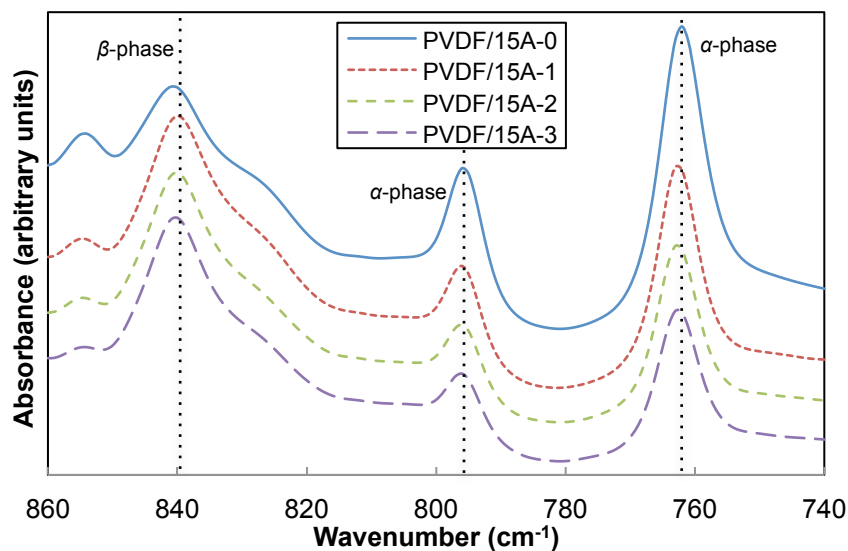


Figure 5-2. FTIR spectra of the membranes

Table 5-3 presents the beta fraction, F_{β} , of the membranes which was calculated using Equation (1) based on the peak areas of the absorption peaks of α -phase and β -phase at 763 cm^{-1} and 840 cm^{-1} respectively. It was observed that the F_{β} value of the composite membranes increased with nanoclay loading, indicating there was a higher ratio of β -phase crystalline form present in the nanocomposite membranes. This result matches previous studies [53, 90, 109, 113], and the reason for the β -phase increase is due to the similarity between the crystal lattice of nanoclay and that of PVDF β -phase [53].

Table 5-3. F_{β} of membranes

Membrane	F_{β}
PVDF/15A-0	0.17
PVDF/15A-1	0.45
PVDF/15A-2	0.49
PVDF/15A-3	0.54

Among the five phases of PVDF, namely α , β , γ , δ and ϵ [54], α - and β -phase are the most reported and identified [86]. While α -phase is kinetically favourable owing to a trans-gauche configuration, β -phase has all-trans conformation which is the most thermodynamically stable form [87]. Furthermore, previous studies [53, 90] have identified that shifting from α -phase to β -phase is related to an improvement in abrasion resistance and mechanical properties such as stiffness and toughness in nanocomposite materials.

5.2.3 Effect of nanoclay on membrane morphology

The cross-sectional morphology of PVDF and PVDF/Cloisite[®] 15A nanocomposite membranes are presented in Figure 5-3. All membranes exhibit a similar cross section morphology with a thin skin layer on top of small finger-like voids on the quench side of the membrane, graduating to the sponge layer on the other side of the membrane (glass-contact side). This asymmetric morphology is common in flat sheet membranes formed by phase inversion [22, 83, 122]. The sponge layer is necessary for membrane strength, while the skin layer performs the functional separation. With the progressive incorporation of nanoclay, gradual change in membrane morphology was observed. As the nanoclay content increased, the depth and the width of the finger-like voids increased accordingly. Macrovoid depth can either increase or decrease with surfactant addition which changes the liquid-liquid demixing rate [73]. The Cloisite[®] 15A chemistry (Table 3-2) is, therefore, important in controlling macrovoid formation. In this case, its effect might be explained by an increase in the demixing rate in the phase inversion process as the solid nanoparticles made the synthesis solution thermodynamically less stable [134]. This brought rapid nucleation from the polymer lean phase and promoted macrovoid formation [71, 135].

It was also noted that the position of the sample taken from the membrane had influence on the membrane morphology. While samples in Figure 5-3(a) to (d) were taken from the centre position of a membrane sheet, the sample used in Figure 5-3(e)

was taken from the edge of the PVDF/15A-3 membrane. By comparing Figure 5-3(d) and (e), it was observed that the macrovoids on the edge tended to collapse or had a folding effect which could be induced by the direction of the solvent as it left the membrane. This folding feature could also be due to shrinking of the membrane during the phase inversion process. The dope cast on the glass plate had an area of 25 cm x 18 cm and the resultant membrane had dimension of 21 cm x 16 cm, showing 16% and 11% reduction in length and width respectively. It seemed reasonable to assume that the material in the centre stayed still, while the sides were drawn into the centre thus making the edges more prone to being 'pulled in' on the free surface in contact with the water.

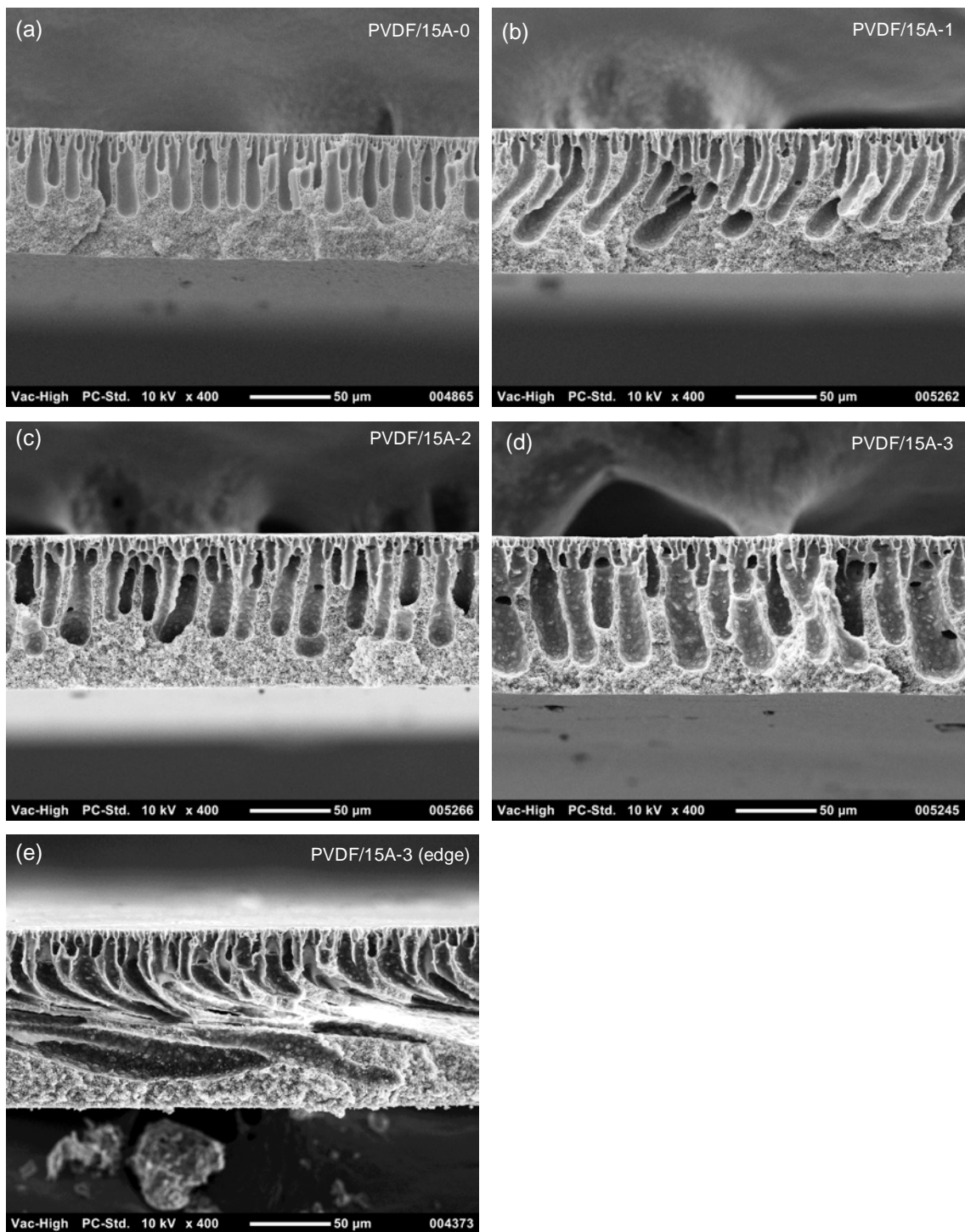


Figure 5-3. Cross-sectional morphology of (a) PVDF/15A-0, (b) PVDF/15A-1, (c) PVDF/15A-2, (d) PVDF/15A-3 and (e) PVDF/15A-3 (edge)

Figure 5-4 displays the water contact side surface morphology of the membranes and the corresponding EDS images of silicon mapping. Since silicon is the most abundant inorganic element present in the nanoclay and it is absent from the PVDF. Therefore mapping the silicon distribution in the image provides a good representation

of nanoclay dispersion throughout the membrane. The surface of the membranes appeared to be porous in general and as the nanoclay loading increases, it is seen that the intensity of silicon detection also increases. The nanoclay appears to be more finely dispersed for lower loadings and larger agglomerates emerge as the loading increases. Also, the intensity-weighted mean diameter of the Cloisite[®] 15A dispersion of 1.6% nanoparticles in NMP derived from the cumulants analysis by the particle sizer, was found to be 4969 nm. This measurement is comparable to some of the larger particle cluster sizes observed in the EDS mapping images. The size of the Cloisite[®] 15A cluster appeared to be considerably larger than that of Cloisite[®] 30B (273 nm) measured after two hours of ultrasonication as shown in Chapter 4. This showed that ultrasonication may not be able to disperse all types of nanoclay as effectively. The need for using a microfluidizer, the more effective technique for dispersion, was justified for the optimised fabrication approach applied to hollow fibres in Chapter 7.

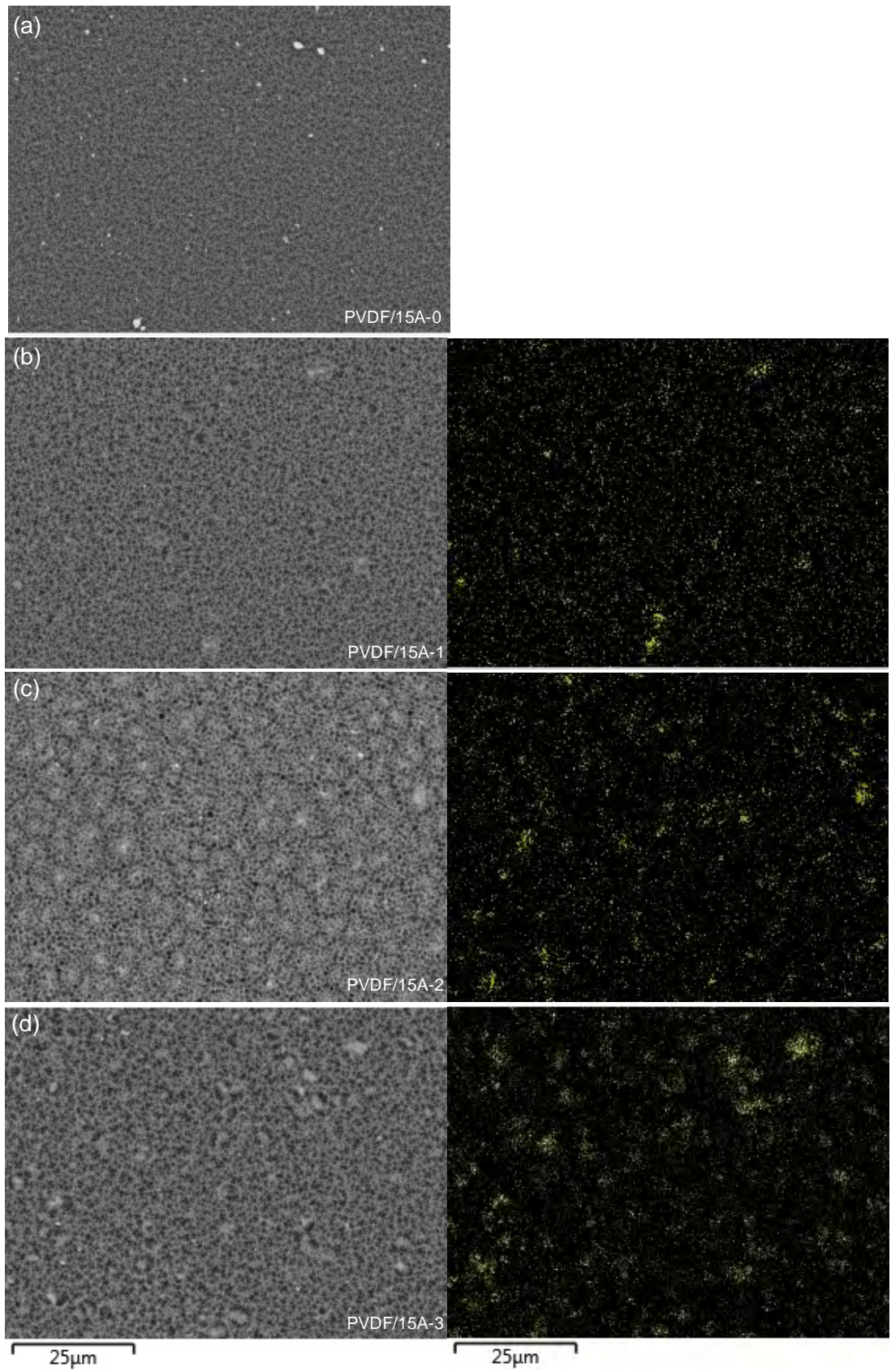


Figure 5-4. Backscattering SEM and silicon mapping images using EDS of membrane quench side surface: (a) PVDF/15A-0, (b) PVDF/15A-1, (c) PVDF/15A-2 and (d) PVDF/15A-3

Table 5-4 presents the overall thickness and the average thickness of the skin layer for each membrane measured from at least five different locations in the SEM cross-sectional images. While the overall membrane thickness increased with nanoclay loading, there was no statistically significant trend in how the addition of nanoclay impacted the skin layer thickness. Generally the skin layers were approximately 1 μm thick.

Table 5-4. Overall membrane thickness and average thickness of skin layer

Membrane	Overall Thickness (μm)	Skin layer thickness (μm)
PVDF/15A-0	84 \pm 2	1.3 \pm 0.1
PVDF/15A-1	91 \pm 1	1.5 \pm 0.3
PVDF/15A-2	96 \pm 1	1.2 \pm 0.3
PVDF/15A-3	97 \pm 3	0.8 \pm 0.1

5.2.4 Dispersion of nanoclay particles

Dispersion of nanoclay at macro-scale was studied with elemental mapping in Section 5.2.3 and this section explores the change in the nanoclay morphology at the nano-scale. The basal spacing (d_{001}) of the nanoclay and the nanocomposite membranes were measured using SAXS beamline with 0.6 m camera length in the Australian Synchrotron. From the SAXS pattern shown in Figure 5-5, Q-range for Cloisite[®] 15A had a dominant peak at 0.195 \AA^{-1} which was equivalent to nominal d_{001} spacing of 3.2 nm. This value was similar to the manufacturer's data listed in Table 3-2 which was 3.15 nm. There was no peak observed for PVDF/15A-0 and PVDF/15A-1 membranes. As nanoclay loading increased, a small peak at 0.250 \AA^{-1} (d_{001} =2.5 nm) appeared on PVDF/15A-2 and there was a more prominent peak at 0.240 \AA^{-1} (d_{001} =2.6 nm) for PVDF/15A-3.

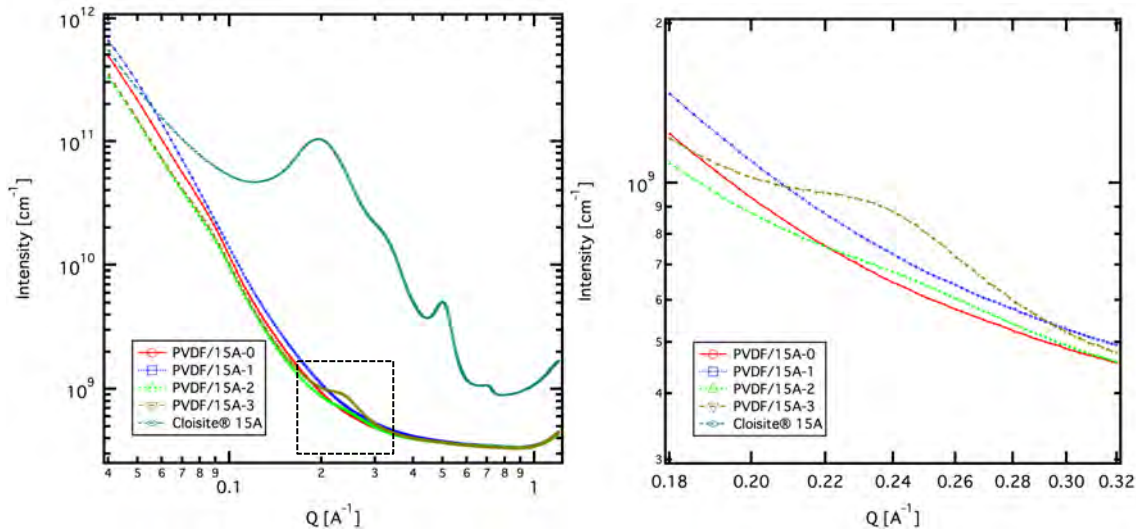


Figure 5-5. SAXS patterns of membranes and Cloisite® 15A powder.

The shift in the dominant peak reflects a decrease in the basal spacing in both PVDF/15-2 and PVDF/15A-3 due to mixing nanoclays into the PVDF. This suggested that the silicate layers of the nanoclay were not intercalated nor exfoliated but remained in phase separated morphology. In fact, the decrease could be due to changes to the conformation of the organic modifier [113] during the membrane fabrication process.

The disappearance of the nanoclay characteristic peak in the PVDF/15A-1 membrane could be due to significant increase in spacing between the silicate layers or the nanocomposite material has lost its ordering [136, 137]. This suggested the nanoclay at low loading underwent complete exfoliation in the polymer matrix, which is a common interpretation by other researchers [83, 90]. However, it is also noted the actual amount of nanoclay incorporated was rather low (0.2 wt% for PVDF/15A-1). The absence of the peak could be simply because the loading was too low to detect. Supplementary characterization technique such as TEM is necessary to confirm the SAXS results.

Literature showed that PVDF/nanoclay nanocomposite with complete exfoliation was possible with NIPS as the silicate layers of the nanoclay can be expanded with solvent dispersion followed by intercalation or exfoliation by the polymer chains [83, 113]. During the NIPS process, the solvent is removed in a rapid rate and the nanoclay morphology is fixed. By comparing the casting conditions of PVDF/Cloisite® 15A nanocomposites in the literature and this study, the casting method was largely the same except for the solvent used. In our study, NMP was used where Dillon and Hwang [83, 113] used DMF and achieved exfoliated nanocomposites determined by XRD and TEM. Ma *et al* [134] has shown that by changing the solvent from NMP to

DMAc, their PSf/nanoclay nanocomposite membrane transformed from intercalated to exfoliated morphology. This indicates that the choice of solvent is important to the exfoliation of the nanoclay. As mentioned in Section 2.2.2.2.1, the choice of solvent can change the membrane morphology. NMP was chosen based on its strong solvent power which undergoes fast demixing process in water and form porous membranes [57, 59]. While this study has not assessed the effect of using different solvents as the primary focus was to evaluate the effect of nanoclay on membrane durability, various casting parameters that may influence nanocomposite membrane properties are explored in Chapter 6.

Table 5-5. Comparison of the casting conditions of PVDF/Cloisite[®] 15A nanocomposites

	This study	Dillon <i>et al</i> [113]	Hwang <i>et al</i> [83]
Material	Membrane	Nanocomposite	Membrane
Polymer	PVDF	PVDF	PVDF
Polymer concentration (wt %)	15 wt%	5 wt%	20 wt%
Solvent	NMP	DMF	DMF
Nanoclay type	Cloisite [®] 15A	Cloisite [®] 15A	Cloisite [®] 15A
Nanoclay loading (by weight of PVDF)	1,3,5 wt%	1-6 wt%	1 wt%
Dispersion method	Ultrasonication for 2 hours	Ultrasonication for 80 min	Mixing
Non-solvent	Water	Water	Water
Non-solvent temperature	60°C	-	-
Nanocomposite morphology	1 wt% - either exfoliated or undetermined 3 and 5 wt% - phase separated	All exfoliated (determined by WAXS and TEM)	Exfoliated (determined by XRD)

5.2.5 Effect of nanoclay on water flux

Figure 5-6(a) shows water fluxes for the various membranes based on the average measurement of three samples of each type. The control PVDF membrane gave an average of 5.0 L/m²h of water flux at 175 kPa TMP. The water flux tends to decrease at low nanoclay content but increases to 7.9 L/m²h as shown by the PVDF/15A-3 membranes. To remove the variation of membrane skin thickness, the product of

permeability and skin thickness (from Table 5-4) was plotted against the nanoclay loading in Figure 5-6(b). It is shown that the addition of nanoclay, especially at lower loading, reduces specific water flux of the material itself once variations in skin layer thickness are accounted for.

The decreasing flux result suggests that the alteration of membrane formulation with various nanoclay loading alters the membrane morphology that relates to water transport. Besides membrane skin thickness, the contact angle, pore size, tortuosity and skin porosity also influence water permeability and the addition of nanoclay appears to have also influenced these properties in the prepared membranes. It was also noted that these water fluxes were much lower than conventional membranes [23]. To optimise the water flux, pore-forming agent is needed in the fabrication process. For this paper, only basic PVDF/nanoclay formulation was used so as to scrutinize the impact of the addition of the nanoparticles. The water flux testing provided a preliminary indication of the membrane hydraulic performance, which is also an important factor besides aiming to improve the mechanical strength and the abrasion resistance of the membranes. A more comprehensive study and discussion on permeability is carried out with hollow fibre membranes in Chapter 7.

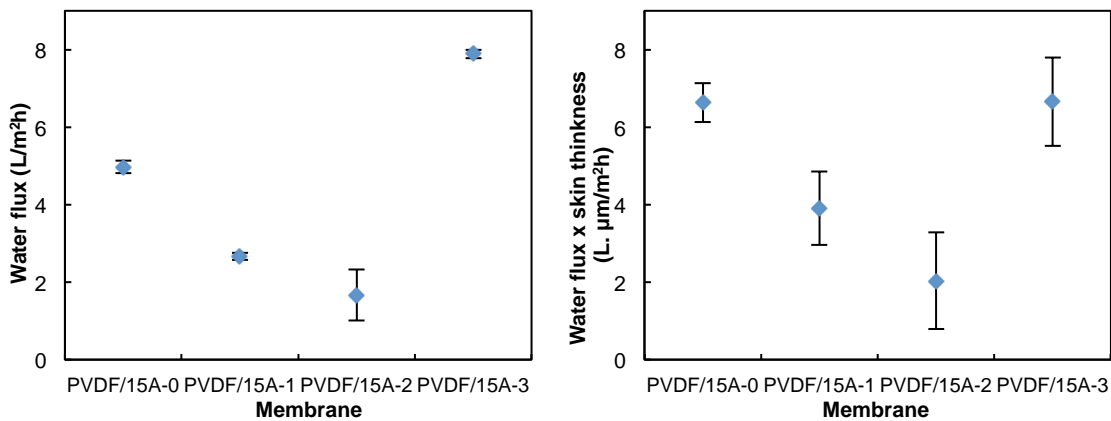


Figure 5-6. Impact of nanoclay on (a) membrane water flux (175 kPa) and (b) water flux times skin thickness (specific skin flux)

5.2.6 Effect of nanoclay on mechanical properties

The test results of mechanical properties including tensile strength and elongation at max load are listed in Table 5-6. It was observed that nanoclay tended to improve the tensile strength at lower loading and PVDF/15A-1 membrane with 1% initial loading giving the best improvement from 4.5 MPa to 4.9 MPa. Hwang *et al* [83] also observed

improved tensile strength and no apparent change in ductile strength with their PVDF/1wt% Cloisite® 15A flat sheet membrane. As the nanoclay loading increased, elongation at maximum load decreased which indicated the ductile strength of the membrane was compromised. The decrease in ductility was likely to be associated with the increased depth and width of finger-like voids as observed in other studies [138, 139].

Table 5-6. Mechanical properties of membranes

Membrane	Tensile strength (MPa)	Elongation at max load (%)
PVDF/15A-0	4.5 ± 0.1	222 ± 21
PVDF/15A-1	4.9 ± 0.1	186 ± 7
PVDF/15A-2	4.8 ± 0.1	131 ± 21
PVDF/15A-3	4.5 ± 0.2	104 ± 13

Figure 5-7 presents Young's modulus and modulus of toughness of PVDF and the composite membranes. It was observed that Young's modulus increased with the nanoclay content, especially for the membranes loaded with 3% and 5% nanoclay (PVDF/15A-2 and PVDF/15A-3) which demonstrates that the addition of nanoclay provides extra stiffness to the polymer matrix. The toughness of a material is defined as the ability of the material to absorb energy up to the point of breakage, and the modulus of toughness is obtained from the area under the stress–strain curve [140]. It was shown that the modulus of toughness reduced as the nanoclay loading increased, showing the composite membranes were less tough than the reference PVDF membrane. These trends could be related to the crystal phase change in PVDF that resulted from incorporation of nanoclay. Nucleation of the fibre-like PVDF β -phase on the faces of individual silicate layers of the nanoclay brings about a structure which is more favourable to plastic flow under applied stress. This results in a more efficient energy-dissipation mechanism in composite membranes, which has been shown in previous PVDF/nanoclay nanocomposite materials studies to delay cracking [53]. Nanoclay can also act as a temporary crosslinker to the polymer chain due to its mobility and this provides localized regions of increased strength and inhibits the development of cracks and cavities [90, 141]. These changes could cause the material to stiffen and become less tough as the nanoclay loading increases. The PVDF/15A-1 membranes demonstrated highest tensile strength while other mechanical properties, including ductility, stiffness and toughness, were either maintained or only slightly reduced when compared to all other membranes.

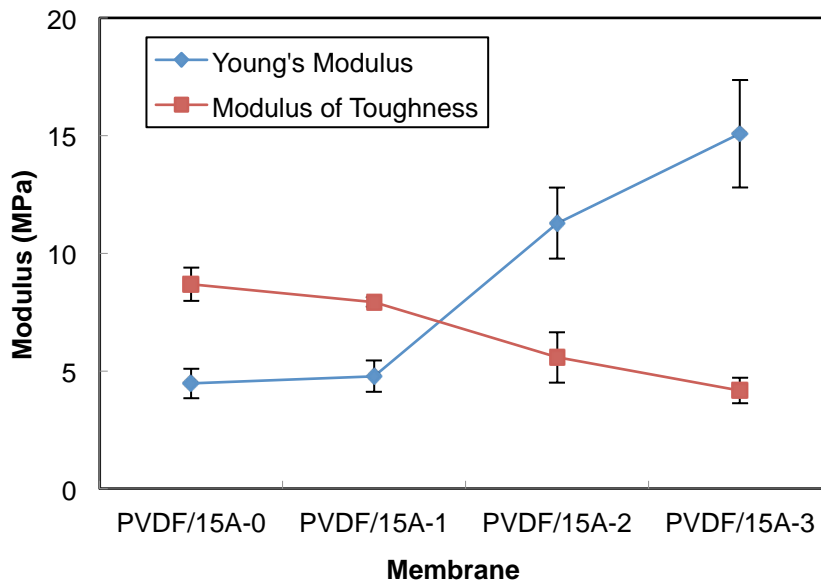


Figure 5-7. Young's modulus and modulus of toughness of PVDF composite membranes

5.2.7 Effect of nanoclay on abrasion resistance

Figure 5-8 presents the weight loss per unit area of each membrane after 200 abrasion cycles using sandpaper with P1000 and P1200 grades. All nanocomposite membranes demonstrated lower weight loss than the reference PVDF membrane in both tests. This implies that the addition of nanoclay enhanced the abrasion resistance and that the nanoparticles provide physical reinforcement to the polymer structure. The result was more sensitive to the coarser grade sandpaper, P1000. The average particle diameter of abrading materials embedded in P1000 sandpaper was 18.3 μm , compared to 15.3 μm in P1200, making it a rougher and more abrasive material. As such, the weight loss of membrane with P1000 was higher overall.

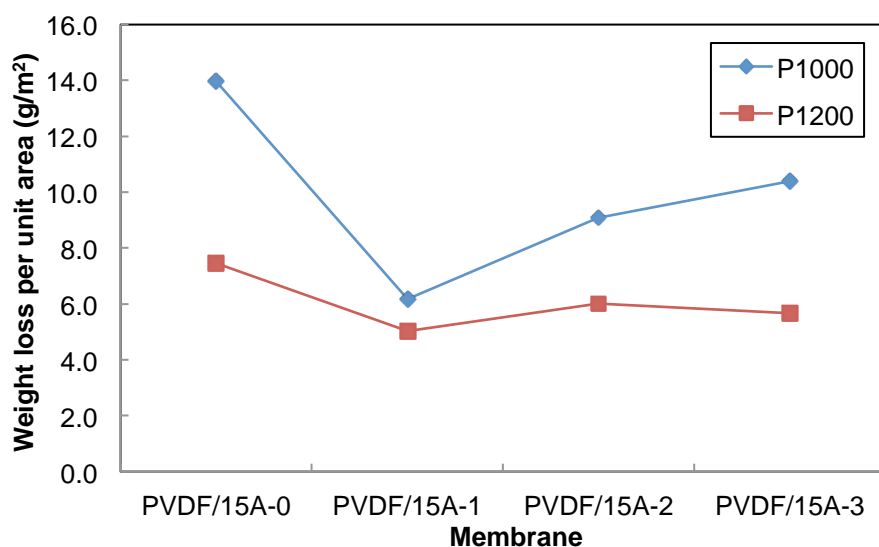


Figure 5-8. Weight loss per unit area of membrane after 200 abrasion cycles with two different grades of sand paper

The PVDF/15A-1 membrane with 1 wt% initial nanoclay loading gave the smallest weight loss per unit area among the four membranes tested. The PVDF/15A-1 membrane lost 6.2 g/m² compared to 14.0 g/m² lost by the PVDF membrane when abraded with P1000. This suggests that the nanocomposite membrane can last two times longer than a conventional unmodified membrane under the same abrasive conditions and would be a candidate material for filtration in more abrasive conditions.

SEM images of the quench side membrane surface (skin layer side) before and after abrasion testing with P1000 are shown in Figure 5-9. Before the test, all membranes appear to have smooth surfaces much like the surface images shown in Figure 5-4. After the test, the control PVDF membrane with no nanoclay (PVDF/15A-0) revealed the most worn surface of all four membranes. Nanocomposite membranes appear to be smoother with less pitting in the surface compared to the control membrane, with PVDF/15-1 the least damaged. These observations are comparable to the respective weight loss of the membranes (Figure 5-8).

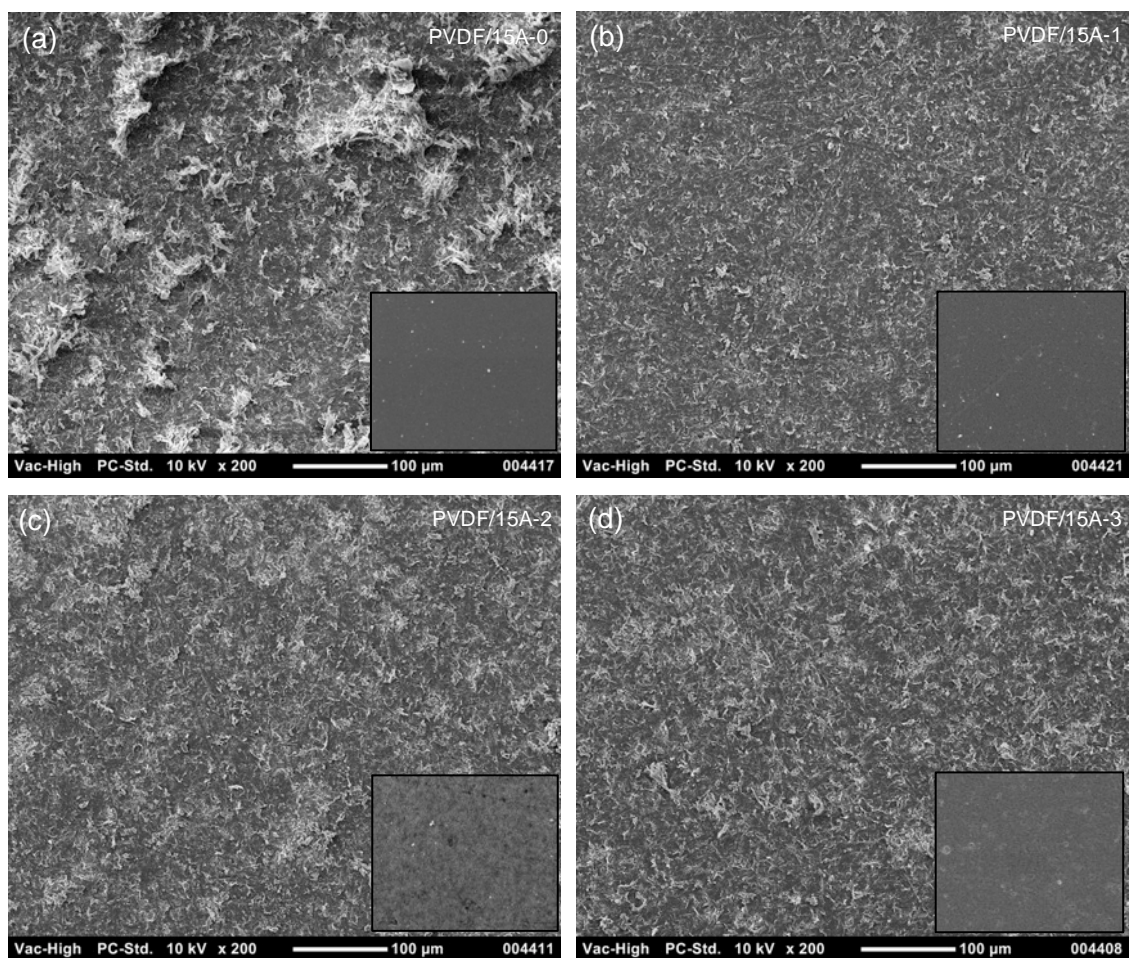


Figure 5-9. SEM images of membrane surface after abrasion testing: (a) PVDF/15A-0, (b) PVDF/15A-1, (c) PVDF/15A-2 and (d) PVDF/15A-3. Original surface is shown as inset in each image.

The improvement of abrasion resistance observed for the nanocomposite membranes could be related to the increased F_{β} as shown in Table 5-3. The more abundant β -phase PVDF increases the binding energy between macromolecule chains and improves abrasion resistance as the surface is less likely to peel off, which has been observed in studies of PVDF/clay nanocomposites [90]. However, it was noted that although PVDF/15-2 and PVDF/15-3 membranes had even higher F_{β} , they showed greater amounts of weight loss which implies reduced abrasion resistance compared to the PVDF/15A-1 membrane. This weakening could be due to the reduced ductility and toughness as observed earlier (Table 5-6 and Figure 5-7) but also owing to increasing size (up to 5 μm for sample PVDF/15A-3 as shown in Figure 5-4(d)) and amount of agglomeration as the nanoclay loading increases. Nanoclay agglomeration tends to cause the material to be more readily peeled off during the abrasion process [90, 142].

Nevertheless, our work has indicated that both overall membrane mechanical properties and the physical/chemical behaviour of the nanoclays within the PVDF matrix are tied to the improvement in the abrasion resistance of membranes. This appears to function best at low nanoclay concentration. It is also important to note that even though complete exfoliation is often the preferred morphology, which brings about significant mechanical improvement with very low nanoparticle loading needed [103, 111, 112], notable improvement in mechanical properties and abrasion resistance was still observed for PVDF/15A membranes with possible phase separated morphology determined by SAXS. While it may be possible to further enhance these properties with complete exfoliation, the addition of nanoclay for improved abrasion resistance has been justified. Using a better dispersion technique such as microfluidizer, as noted in Chapter 4, may allow high nanoclay content materials to exhibit better physical durability due to reduced agglomeration. Thus hollow fibre membranes to be made in Chapter 7 will feature the more superior dispersion technique.

5.3. Conclusions

PVDF/Cloisite[®] 15A nanocomposite flat sheet membranes were fabricated using phase inversion. The key parameters of these membranes are summarized in Table 5-7. SEM and EDS images show that the nanoclay was dispersed throughout the membrane and the membrane structure appeared to be altered by the addition of nanoparticles. Nanoclay also promoted a change of the PVDF crystalline phase from α - to β -phase and appeared to reduce water flux at lower loadings. Nanocomposite membranes exhibited higher tensile strength and stiffness, but lower ductility and toughness. Despite phase separated morphology at high loading indicated by SAXS, all nanocomposite membranes showed increased resistance to abrasion compared to the reference PVDF material in a simple abrasion testing setup. The PVDF/15A membrane with 1 wt% initial loading demonstrated the highest tensile strength and the strongest abrasion resistance despite the slightly lower toughness compared to reference PVDF material. Better mixing may reduce agglomeration enabling more durable materials at higher loadings. Nanocomposite PVDF/nanoclay membranes are therefore suitable for improved abrasion resistance in water treatment applications such as desalination pretreatment.

Table 5-7. Summary of key parameters of PVDF/15A membranes.

Membrane	% of nanoclay in dope by weight of PVDF	% of nanoclay retained	F_{β}	Overall Thickness (μm)	Skin layer thickness (μm)	Specific water flux (L. $\mu\text{m}/\text{m}^2\text{h}$)	Elongation at max load (%)	Young's modulus (MPa)	Modulus of toughness (Mpa)	Weight loss per area (g/m^2)
PVDF/15A-0	0	-	0.17	84 ± 2	1.3 ± 0.1	6.6 ± 0.5	222 ± 21	5.9 ± 0.8	8.7 ± 0.7	14.0
PVDF/15A-1	1	17	0.45	91 ± 1	1.5 ± 0.3	3.9 ± 0.9	186 ± 7	4.7 ± 0.7	7.9 ± 0.2	6.2
PVDF/15A-2	3	17	0.49	96 ± 1	1.2 ± 0.3	2.0 ± 1.3	131 ± 21	11.2 ± 1.5	5.6 ± 1.1	9.1
PVDF/15A-3	5	24	0.54	97 ± 3	0.8 ± 0.1	6.7 ± 1.1	104 ± 13	14.6 ± 2.2	4.2 ± 0.5	10.4

6. Impact of casting conditions on membrane properties

The preliminary study with PVDF/Cloisite[®] 15A membrane in Chapter 5 has shown that incorporation of nanoclay has successfully improved the membrane mechanical properties and abrasion resistance. However, as shown in the TGA result in Section 5.2.1, no more than 24% of the initial nanoclay loading was retained in the membrane and the rest was likely lost in the coagulation bath. Despite the improved mechanical properties achieved, it is preferable from an economic standpoint to retain as much of the nanoclay as possible within the membrane. With this in mind, it is important to select a procedure to improve nanoclay retention.

This study explores the various conditions that can be changed during fabrication and how they influence the incorporation of nanoparticles within the membrane material. While observing conditions that minimise nanoparticle loss, another goal was to also observe changes in membrane crystal phase and physical structure studied with FTIR and SEM respectively. Mechanical properties of the membranes were measured using an Instron tensile testing instrument. Modified nanoclays were dispersed into membranes made from PVDF. The conditions that have been investigated include the retention time of casting dope in air, temperature and composition of the quench bath, the PVDF/NMP ratio of the dope as well as the humidity of the casting environment. The effect of nanoclays with different organic modifiers and PVDF with various molecular weights was also studied. The inorganic content of the membranes was measured with both TGA and LOI.

6.1. Results and discussion

6.1.1 Effect of various nanoclays

6.1.1.1 *Nanoclay retention*

Eight PVDF/nanoclay nanocomposite flat sheet membranes were prepared according to Section 3.3.1 each using different commercially available nanoclay as filler. The synthesis dope contained 5 wt% of nanoclay and the percentage of nanoclay retained in the membrane was determined by both TGA and LOI and presented in Table 6-1.

Table 6-1. Percentage of nanoclay retained in membranes using different types of nanoclays and F_{β} of the membranes. High F_{β} (>0.90) highlighted in light grey, and high % retention (>40%) highlighted in dark grey.

Membrane	% of nanoclay retained		F_{β}
	TGA*	LOI [^]	
PVDF	-	-	0.20 ± 0.01
PVDF/10A 5%	36%	32%	0.94 ± 0.01
PVDF/15A 5%	25%	32%	0.53 ± 0.02
PVDF/30B 5%	31%	36%	0.97 ± 0.01
PVDF/I28E 5%	26%	36%	0.55 ± 0.01
PVDF/I30E 5%	45%	43%	0.52 ± 0.03
PVDF/I31PS 5%	34%	38%	0.42 ± 0.01
PVDF/I34TCN 5%	35%	37%	0.93 ± 0.04
PVDF/I44P 5%	32%	38%	0.45 ± 0.01

* The average error for the TGA results was +/- 4%.

[^] The average error for the LOI results was +/- 2%.

It is shown that the PVDF/I30E membrane had the highest percentage of nanoclay retained as determined by both methods. All eight nanoclays have different organic modifiers and it is possible that Nanomer[®] I.30E with a single tallow arrangement has the best compatibility with PVDF matrix giving the best retention. It was noted that in most cases, LOI gave a larger % of nanoclay retained than TGA (apart from PVDF/10A 5% and PVDF/I30E 5%). The difference could be because the weight % determined by TGA was in fact smaller than the actual value. This was evident when neat PVDF membrane was tested with TGA for which the final weight % was expected to be 0% as the membrane contained no inorganic content. However, this test resulted in negative values at times (up to -0.7%) which skewed down the % of nanoclay retained values in other cases. The error was likely due to the small amount of sample used which brought about large variability. As such, nanoclay retention determined by LOI was more reliable and this method was adopted for further testing in Section 6.1.3 and Section 7.2.1.

6.1.1.2 Membrane crystalline phase

The beta fraction, F_{β} , of the membranes shown in Table 6-1, was calculated using Equation (3) based on the peak areas of the absorption peaks of PVDF α -phase and β -phase at 763 cm^{-1} and 840 cm^{-1} respectively. It was observed that all composite

membranes had higher F_{β} than neat PVDF membrane, indicating part of the PVDF crystalline phase was shifted from α -phase to β -phase when nanoclay was incorporated. It was also noted that three membranes, namely PVDF/10A 5%, PVDF/30B 5% and PVDF/I34TCN 5%, had particularly high F_{β} (> 0.90), while the rest were ~ 0.50 . It appeared that the higher F_{β} was not related to the % of nanoclay retained in membrane, but rather to the organic modifier of the cation in the nanoclay. While nanoclays showing lower F_{β} (15A, I28E, I31PS and I44P) only contained tallow and/or methyl groups on the quaternary ammonium, 30B and I34TCN have dihydroxyethyl groups and 10A had a benzyl group attached (Table 3-2). These additional functional groups appeared to be highly effective for inducing the formation of PVDF β -phase, and it was potentially significant for membrane fabrication as β -phase was related to improvement in abrasion resistance, mechanical properties and fouling resistance (Chapter 2).

6.1.1.3 Membrane morphology

Figure 6-1 presents the cross-sectional images of original PVDF and the nanocomposite membranes modified by eight different nanoclays. Similar to the unmodified membrane, all nanocomposite membranes had an asymmetric structure with skin layer extending to finger-like voids sitting on top of a sponge-like layer (Figure 2-3). The main difference observed in the morphology of the nanocomposite membranes was the depth of the macrovoids. Membranes modified with Cloisite[®] 10A (b), Cloisite[®] 30B (d) and Nanomer[®] I.34TCN (h) had the biggest magnitude of macrovoids and the organic modifiers on these three nanoclays were the most hydrophilic among all [143]. Wang *et al* [73] found the formation of macrovoids in the asymmetric membrane can be either enhanced or suppressed with the addition of surfactants in the casting dope, depending on the miscibility between the surfactant and the coagulant. The nanoclay that has been incorporated may act in a similar role to that of the surfactant. Cloisite[®] 10A, Cloisite[®] 30B and Nanomer[®] I.34TCN being hydrophilic had high miscibility with water and hence induced the liquid-liquid demixing process which enhanced macrovoid formation. Despite the high F_{β} and the potential desirable properties shown in Section 6.1.1.2 by these three membranes, the poor membrane structure (as indicated from the large macrovoids in PVDF/10A, PVDF/30B and PVDF/I34TCN) was a major drawback as it would not provide enough mechanical support for rigorous filtration applications.

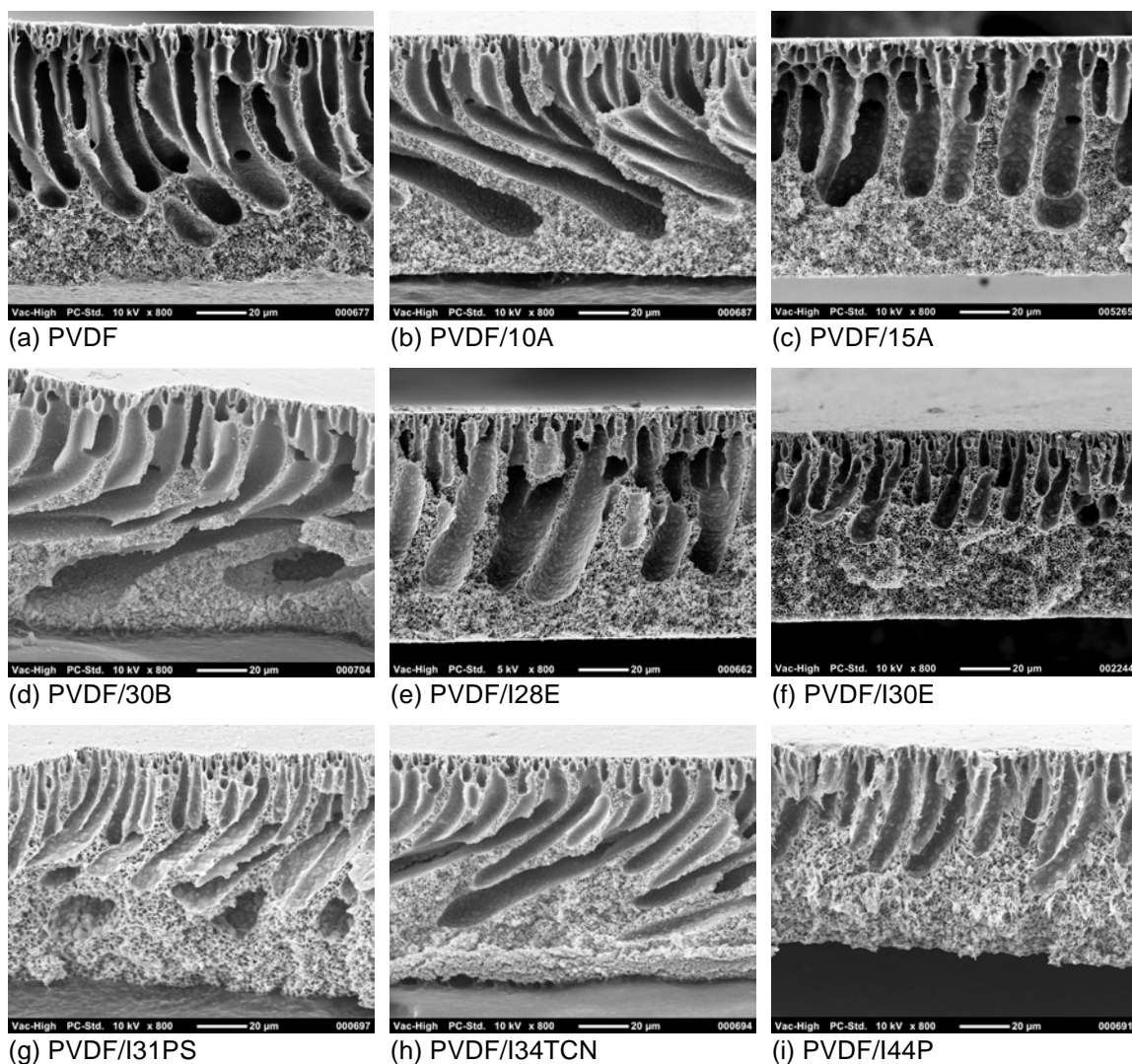


Figure 6-1. Cross-section morphology of (a) PVDF, (b) PVDF/10A, (c) PVDF/15A, (d) PVDF/30B, (e) PVDF/I28E, (f) PVDF/I30E, (g) PVDF/I31PS, (h) PVDF/I34TCN and (i) PVDF/I44P membranes.

Among other types of nanocomposite membranes that had good membrane structure, including PVDF/15A, PVDF/128E, PVDF/I30E, PVDF/I31PS and PVDF/I44P, all possessed F_{β} range between 0.42 and 0.55, which was considerably higher than neat PVDF (0.20). However, PVDF/I30E had noticeably higher percentage of nanoclay retained (at least 5% greater) than the other four membranes. As a result, Nanomer[®] I.30E was selected for use in the subsequent experiments investigating changes in casting conditions as it had the highest retained percentage, 43% as determined by LOI, in the membrane (Table 6-1) and one of the better membrane structures among the nanocomposite membranes. However other nanoparticles were retained by only a slightly lower amount, for example the lowest were 10A, 15A and I28E, being 32%,

32% and 36% respectively. Further work could consider other organic functional group types on the nanoclay as they might offer different retention characteristics and properties to the membrane. It was worthwhile to note that I30E with the highest retention uniquely had the simplest modifier, having a single alkyl group on the ammonium while all other modifiers had four alkyl or tallow groups attached to the ammonium. Therefore exploring similar modifier chemistries, such as varied alkyl chain lengths on single alkyl group ammonium modifiers, may be a good next step to see if there is a link between the simple linear alkyl groups and retention of the nanoclays.

6.1.2 Effect of casting conditions on membrane morphology

6.1.2.1 *Air retention time*

Air retention time refers to the time between spreading the dope with a doctor blade and immersing the cast dope into the quench bath. Figure 6-2 presents the cross-sectional images of PVDF/I30E membrane fabricated with immediate immersion (a) and exposure in air for one (b), five (c) and ten (d) minutes. It was observed that membranes with immediate immersion and one minute retention time had similar structure. As NMP is a relatively non-volatile solvent, solvent evaporation was not significant within this short period of time so thus the membrane structure was not altered. As the air retention time increased, thicker membranes were formed and the depth and width of finger-like macrovoids increased which was similar to the study by Hwang *et al* [83], who observed that PVDF/nanoclay membranes exposed in air for 60 s had larger macrovoids than those exposed for 30 s when using DMF as solvent. With longer air retention time, the extent of solvent evaporation increased and larger macrovoids were evidence of the evaporated solvents being trapped at the upper side of the membrane [144]. Furthermore, water vapour (non-solvent) in the air absorbed into the dope during air retention, changing the thermodynamic characteristics of the dope. VIPS then took place and induced early precipitation. For flat sheet membranes fabricated in Chapter 4 and 5, they were immersed in the water bath immediately after casting. Therefore, the original procedure to make membranes is suitable, but if slightly longer air retention times are used, it will not lead to major changes to the structure.

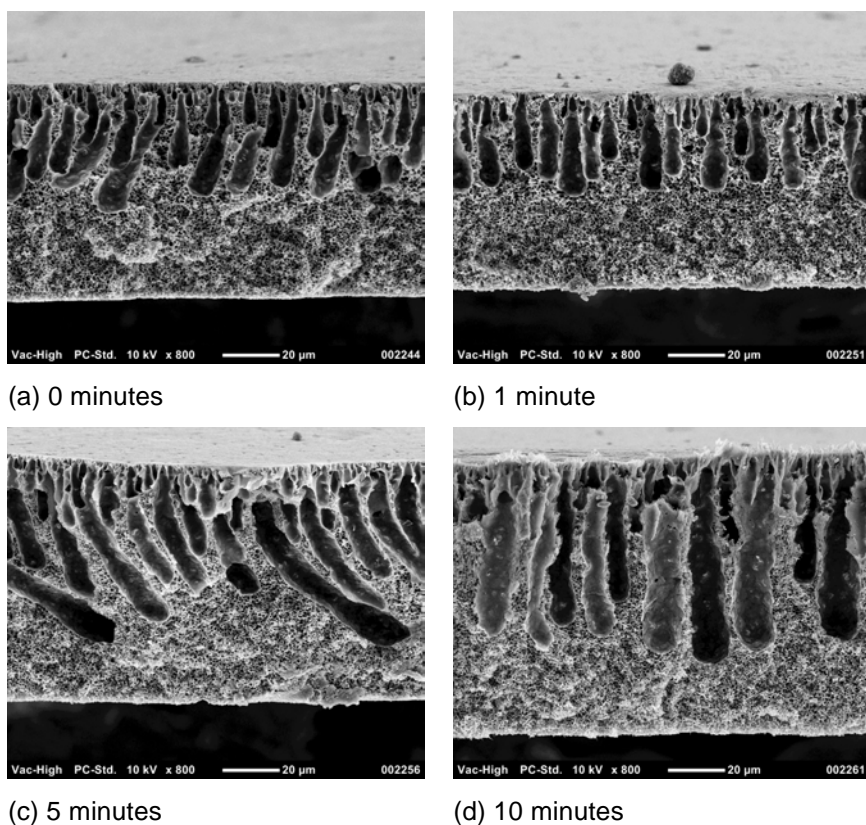


Figure 6-2. Cross-section morphology of PVDF/I30E membranes prepared with retention time of (a) 0 minutes, (b) 1 minute, (c) 5 minutes and (d) 10 minutes.

6.1.2.2 Quench bath temperature

PVDF/I30E 5% membranes were fabricated using a water bath at three different temperatures and the cross-sectional morphology is shown in Figure 6-3. As the bath temperature increased from 20°C to 60°C, improved membrane structure was observed with less interconnected hollow space. Although previous literature [78-80] has reported that PVDF membranes undergo crystallisation-dominated precipitation at low temperature (15-20°C), which brings about symmetric structure with spherical crystallites, it is interesting to note the nanocomposite membrane fabricated at 20°C (Figure 6-3(a)) showed a typical asymmetric structure with skin layer and underlying sponge layer despite its distorted fashion. This could be due to the presence of nanoclay keeping liquid-liquid demixing as the primary mechanism during phase inversion rather than crystallisation. Given the best membrane structure resulted from the 60°C water bath, this justified the same condition chosen for membranes cast in Chapter 4 and 5. Following on from this finding, hollow fibres in Chapter 7 were also cast using a 60°C water bath.

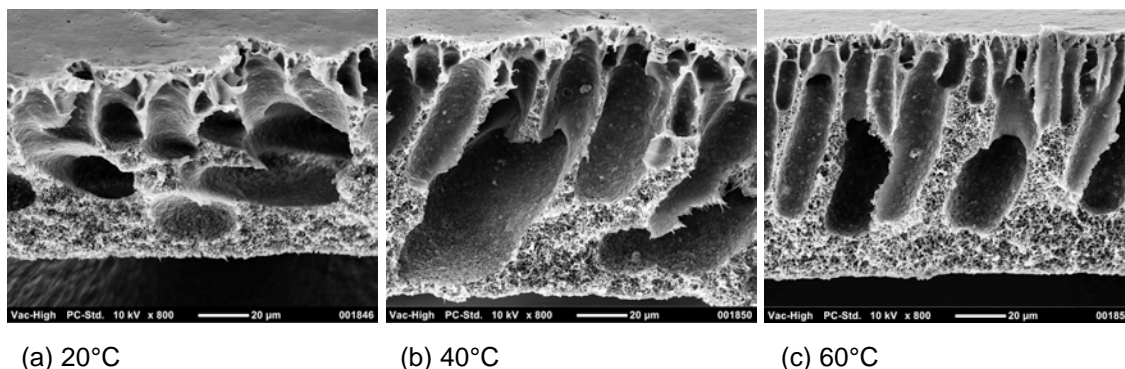


Figure 6-3. Cross-section morphology of PVDF/I30E membranes prepared with quench bath temperature at (a) 20°C, (b) 40°C and (c) 60°C.

6.1.2.3 Quench bath medium

PVDF/I30E 5% membranes were fabricated using four different quench baths with pure water and three additives – 10 wt% NaCl, 10 wt% NMP and 10 wt% glycerol respectively. The cross-sectional images of these membranes are presented in Figure 6-4. The addition of NaCl, NMP and glycerol represented the role of inorganic salt, solvent and weak non-solvent additives respectively. With the addition of NaCl, the resultant membrane appeared narrower with shorter macrovoids than the one made with pure water. The presence of NaCl decreased the activity of the aqueous coagulation bath by lowering the chemical potential (μ) of water and thus weakened the driving force for transportation at the film interface [76, 77, 145]. This was inline with the increased gelation time from 10 s to 25 s when NaCl concentration increased from 1 wt% to 20 wt% in Yang *et al's* study [77] on polyacrylonitrile membranes. With this the rate of flow of water into the dope was reduced while the solvent exchange rate became slow and inhibited macrovoid formation. As water is a strong non-solvent, adding either NMP or glycerol will slow the liquid-liquid demixing process [59]. These additives reduced the PVDF concentration in the film at the interface and resulted in slow precipitation and less macrovoids were formed in the membranes as shown in Figure 6-4(c) and (d) [50, 57]. Although additives to the quench bath could potentially improve the membrane structure, increases in production cost and environmental impact (from the disposal of the spent bath) may not justify the improvement. As such, water remained as the quench bath medium used for flat sheet membranes in Chapter 4 and 5 and hollow fibres in Chapter 7.

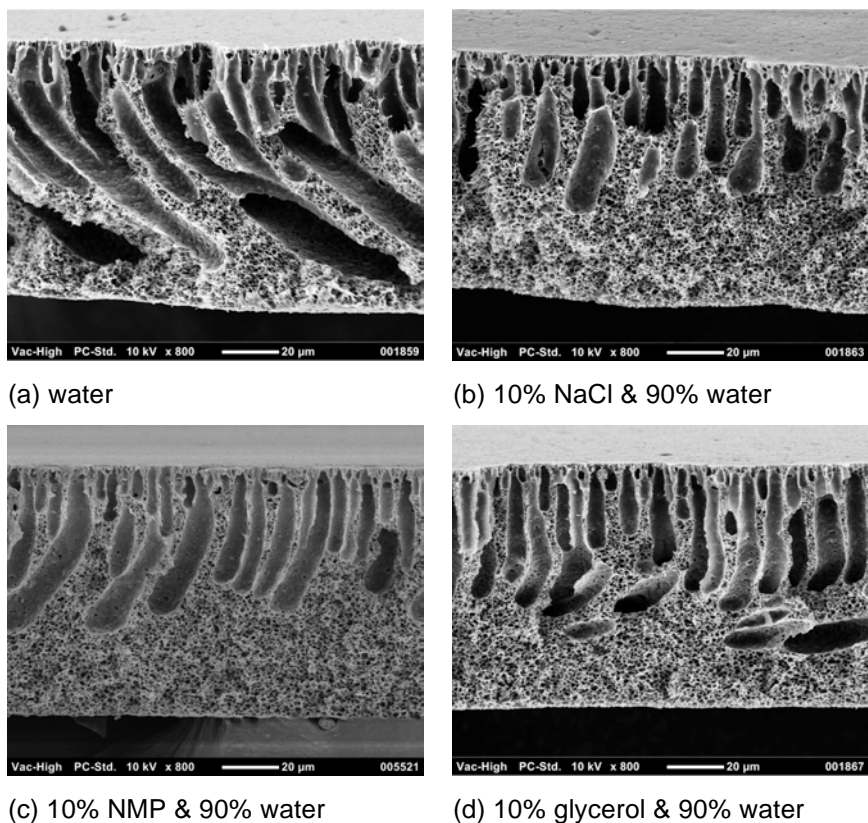
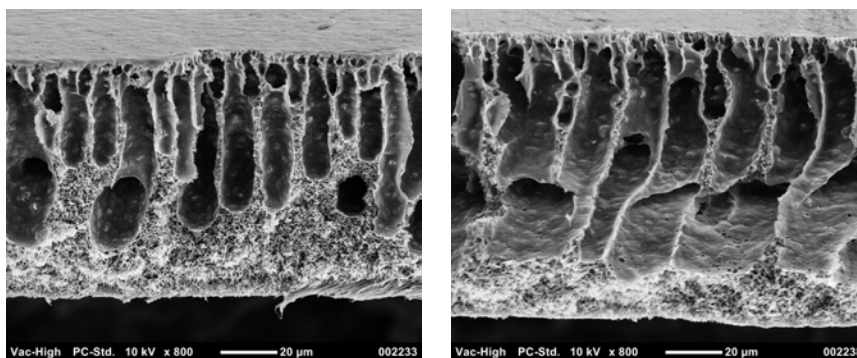


Figure 6-4. Cross-section morphology of PVDF/I30E membranes prepared with (a) water, (b) 10% NaCl & 90% water, (c) 10% NMP & 90% water and (d) 10% glycerol & 90% water as the quench bath medium.

6.1.2.4 Humidity of the casting environment

Humidity of the casting environment impacts the rate of VIPS as the amount of water vapour present in air changes. Cast dope exposed at 30%RH represented a low humidity environment and that at 90%RH represented high humidity. As shown in Figure 6-5, the membrane fabricated under high humidity was thicker with a denser skin layer. This is consistent with Chung *et al's* [81] observation with polyimide membranes, as high humidity enhances the VIPS process and induces early precipitation. Given that larger macrovoids appeared in the membrane cast at 90%RH, it seemed that structure-wise it was not beneficial to cast film under high humidity. For flat sheet membranes fabricated in Chapter 4 and 5, they were cast at room temperature with humidity varying between 40-50%RH.



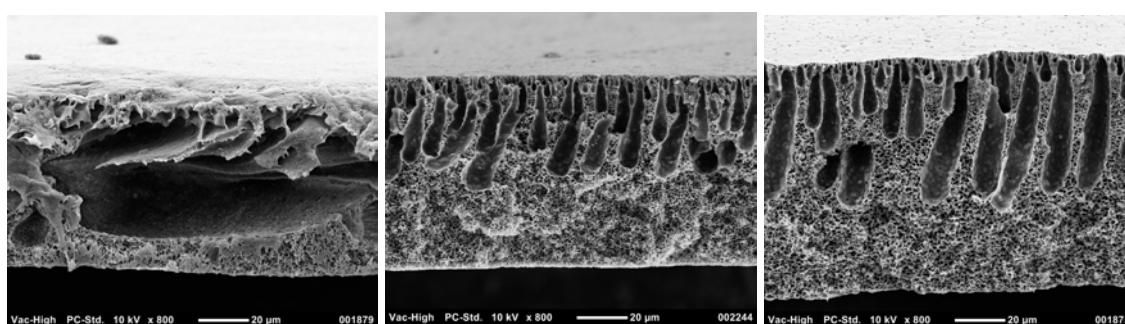
(a) 30%RH

(b) 90%RH

Figure 6-5. Cross-section morphology of PVDF/I30E membranes prepared at (a) 30%RH and (b) 90%RH.

6.1.2.5 Polymer concentration (ratio of PVDF/Nanoclay to NMP)

By increasing polymer concentration in the dope, the viscosity of the dope also increased [146]. As seen from Figure 6-6(a), the low viscosity of the weakest PVDF dope, 10:90 (PVDF/nanoclay:NMP), resulted in poor membrane structure and as such typical polymer/nanoparticle:solvent ratio for UF membranes is usually 15:85 to 20:80 [57]. As PVDF loading increased, Figure 6-6 shows membranes with thicker skin layers and increased overall thickness were formed. The higher initial polymer loading resulted in higher polymer concentration at the film interface and increased the volume fraction of polymer [50]. For flat sheet membranes fabricated in Chapter 4 and 5, the ratio of PVDF/Nanoclay to NMP was 15:85.



(a) 10:90

(b) 15:85

(c) 20:80

Figure 6-6. Cross-section morphology of PVDF/I30E membranes prepared with ratio of PVDF/nanoclay to NMP at (a) 10:90, (b) 15:85 and (c) 20:80.

6.1.2.6 Molecular weight of PVDF

Varying the molecular weight of PVDF can control the viscosity of the casting dope as the viscosity of dope increases with molecular weight of PVDF. Similar to Section 6.1.2.5, the dope with low viscosity resulted in poor membrane structure as shown in Figure 6-7(a). Comparing Figure 6-7(b) and (c), the membrane overall thickness and the skin layer thickness increased as the molecular weight of PVDF increased. This could be attributed to a similar explanation of increased viscosity as discussed in Section 6.1.2.5, as high molecular weight polymers are known to lead to higher viscosity solutions than low molecular weight polymers [147]. Solef[®] 1015 (573 kDa) was chosen as the PVDF for flat sheet membranes fabricated in Chapter 4 and 5 and hollow fibres in Chapter 7.

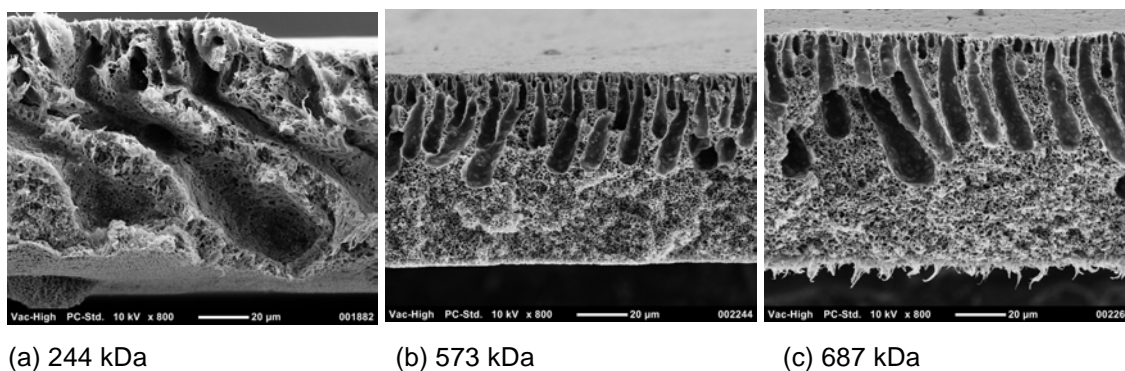


Figure 6-7. Cross-section morphology of PVDF/I30E membranes prepared with PVDF molecular weight of (a) 244 kDa (Solef[®] 6008), (b) 573 kDa (Solef[®] 1015) and (c) 687 kDa (Solef[®] 6020).

6.1.3 Effect of casting conditions on nanoclay retention

The percentage of nanoclay retained in each of the above membranes was determined by LOI and are listed in Table 6-2. While some conditions such as quench bath temperature and humidity did not significantly impact nanoclay retention, other casting conditions did. With increasing air retention time, percentage of nanoclay retained decreased indicating solvent evaporation process and/or VIPS had a negative impact on retaining the nanoparticles. It is possible that as solvent evaporated away the membrane surface, the nanoclay particles were subsequently closer to the film surface and as the dope was immersed into the quench bath, the particles were more ready to leach out. Also, if water vapour was absorbed during air exposure, it might migrate to the hydrophilic nanoparticle surfaces rendering them coated in non-solvent

and facilitating their transport in to the non-solvent bath. Use of additives in the water bath tended to improve nanoclay retention, with the best increased retention from 43% to 48% achieved by adding 10 wt% NaCl. The presence of additives possibly alters the physicochemical properties of the quench medium and changes the solvent – non-solvent interaction preserving more nanoclay during the solvent exchange process. As for the impact of polymer concentration and PVDF molecular weight, it is evident that there were optimal values (15:85 and 573 kDa) for the best retention, which was about 7% more than the other conditions investigated.

Table 6-2. Percentage of nanoclay retained in membranes, F_{β} and mechanical properties of membranes prepared with various casting conditions. Conditions highlighted in grey denote good membrane structure determined by SEM.

Condition	% of nanoclay retained	F_{β}	Tensile strength (MPa)	Elongation at break (%)	Young's modulus (MPa)
Neat PVDF	-	0.20 ± 0.01	3.7 ± 0.5	62 ± 7	47 ± 3
<u>Air retention time</u>					
Immediate ^	43%	0.52 ± 0.03	4.0 ± 0.1	124 ± 10	83 ± 3
1 min air exposure	40%	0.52 ± 0.01	5.5 ± 0.2	132 ± 2	71 ± 4
5 min air exposure	37%	0.57 ± 0.02	3.8 ± 0.1	95 ± 5	40 ± 9
10 min air exposure	38%	0.72 ± 0.02	3.4 ± 0.1	87 ± 6	38 ± 9
<u>Quench bath temperature</u>					
20°C	43%	0.92 ± 0.01	2.7 ± 0.1	28 ± 4	25 ± 5
40°C	40%	0.64 ± 0.00	2.9 ± 0.2	59 ± 4	38 ± 5
60°C ^	43%	0.51 ± 0.01	3.8 ± 0.1	72 ± 4	49 ± 8
<u>Quench bath medium</u>					
Water ^	41%	0.60 ± 0.02	3.6 ± 0.1	79 ± 13	48 ± 5
10 wt% NaCl	48%	0.99 ± 0.01	4.9 ± 0.1	55 ± 8	52 ± 2
10 wt% NMP	44%	0.62 ± 0.03	4.6 ± 0.1	60 ± 8	59 ± 5
10 wt% Glycerol	46%	0.57 ± 0.01	4.8 ± 0.4	106 ± 8	63 ± 5
<u>Humidity</u>					
30%RH	45%	0.47 ± 0.02	4.0 ± 0.1	66 ± 3	51 ± 5
90%RH	46%	0.60 ± 0.08	2.9 ± 0.2	39 ± 3	31 ± 1

<u>Polymer concentration</u>					
10:90	37%	0.68 ± 0.02	2.5 ± 0.1	48 ± 2	30 ± 5
15:85 *	43%	0.52 ± 0.03	3.8 ± 0.1	92 ± 25	60 ± 17
20:80	36%	0.41 ± 0.01	5.0 ± 0.3	70 ± 9	61 ± 5
<u>PVDF molecular weight</u>					
244 kDa	34%	0.52 ± 0.02	2.9 ± 0.1	34 ± 3	40 ± 4
573 kDa *	43%	0.52 ± 0.03	3.8 ± 0.1	92 ± 25	60 ± 17
687 kDa	36%	0.51 ± 0.01	3.7 ± 0.1	88 ± 6	48 ± 9

* Values averaged from membranes cast with default conditions^ (Table 3-3).

6.1.4 Effect of casting conditions on membrane crystal phase

F_{β} of the membranes cast under different conditions are also shown in Table 6-2. It was confirmed that all PVDF/I30E membranes, regardless of difference in casting conditions, had higher F_{β} than the neat PVDF membrane (0.20). Apart from changing the PVDF molecular weight, altering other casting conditions appeared to impact the degree of PVDF β -phase formation. Increasing the air retention time and the air humidity of the casting environment resulted in increasing F_{β} . This suggested that solvent evaporation and VIPS could possibly enhance PVDF shifting from α -phase to β -phase. Similar to observations in pure PVDF material [91], decreasing the quench bath temperature to 20°C almost eliminated the PVDF α -phase peak at 763 cm^{-1} in the nanocomposite membrane, as shown by the high F_{β} (0.92). However the membrane morphology appeared unsuitable for filtration. While adding NMP or glycerol to the quench bath had no observable effect on the membrane crystal phase, 10% of NaCl in the water bath significantly induced β -phase formation. Further, the structure appeared well suited to membrane filtration, so further exploring membranes produced under this condition is recommended. Finally, increasing the polymer concentration appeared to inhibit the shifting from α -phase to β -phase.

Figure 6-8 presents graphically the correlation between F_{β} and the % of nanoclay retained in the PVDF/I30E membranes prepared with various casting conditions. There seemed no strong correlation between the two parameters. Most membranes with good morphology (absence of large macrovoids) had F_{β} values ranging from 0.5 to 0.6 with 36-46% of nanoclay retained, and these may be the limiting values even for changing casting conditions. The exception was the membrane prepared with 10%

NaCl solution, again supporting the earlier recommendation to explore this condition in more detail.

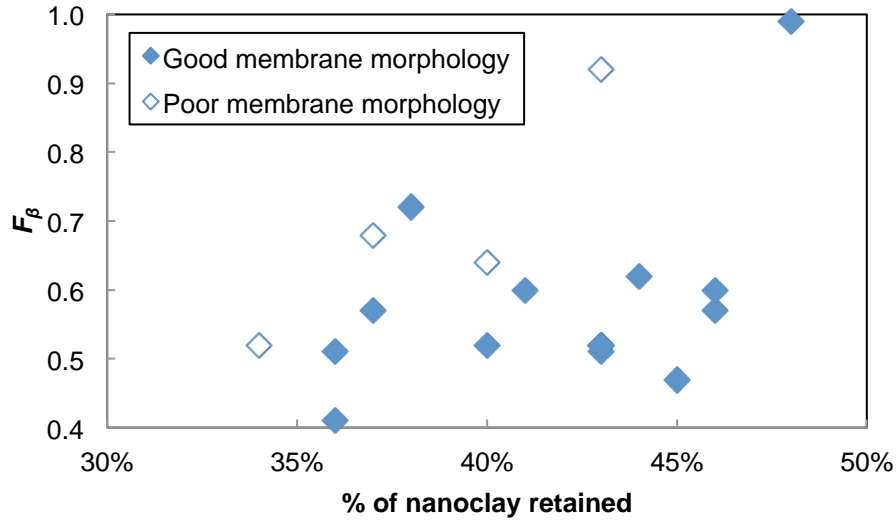


Figure 6-8. F_{β} vs percentage of nanoclay retained in PVDF/I30E membranes prepared with various casting conditions.

6.1.5 Effect of casting conditions on mechanical properties

The testing results of mechanical properties including tensile strength, elongation at break and Young's modulus are listed in Table 6-2. In general, the mechanical properties of the membranes were associated with their membrane morphology. From the SEM cross section images in Section 6.1.2, membranes cast at 20°C and 40°C, with 10% PVDF concentration and with PVDF molecular weight of 244 kDa showed poor membrane structure with large macrovoids. These membranes also had significantly lower tensile strength, elongation and modulus compared to others. Generally, membranes with small macrovoid morphology (highlighted in grey in Table 6-2) had tensile strength > 3.5 MPa. This showed the importance of the overall structure on determining the mechanical strength, thus abrasion theory using mechanical properties of the bulk material may not be relevant to porous membranes. Section 7.2.7 will further explore this. Other than having the highest tensile strength with 1 min air exposure time, other mechanical properties including ductility and stiffness declined as the air retention time increased along with longer macrovoids formed in the membranes (Figure 6-2). This was also true for membrane cast under a high humidity environment. All mechanical properties of the membrane cast at 90%RH

were lower than those for the membrane cast at 30%RH, as seen from the wider and deeper macrovoids in Figure 6-5(b). It was noted that although PVDF β -phase was related to improved mechanical properties [53, 90], there may be a limit for the amount of β -phase to be effective. The membrane cast with a 10 wt% NaCl quench bath had the highest F_{β} and high tensile strength, but it did not lead to the strongest mechanical properties in terms of ductility and stiffness. The membrane fabricated using a 10 wt% glycerol quench bath showed considerably higher ductility than the other quench bath media. It was possibly that some glycerol remained in the membrane which helped preserve the porous structure and enhanced the mechanical properties.

It was noted that there was some variability between different batches of membranes despite the same casting conditions. Membranes marked with ^ in Table 6-2 were cast in a 60°C water bath with no air retention time. The inconsistency could be because the membranes were cast by hand and under different room conditions. To eliminate human error, hollow fibres in Chapter 7 were cast using an automated extruder with fixed air gap and extrusion speed. Nevertheless, the trends observed for each casting parameter are expected to be reliable, as the membranes were fabricating from the same dope and within the same period of time thus minimising any errors associated with reproducibility of the dope. The study provided some insight to balance various properties that were important for membrane fabrication.

6.2. Conclusions

The impact on nanoclay retention, membrane morphology, crystal structure and mechanical properties has been studied using different nanoclays and various casting conditions. Although the study did not reflect a clear trend in all cases, it is still important to understand both sensitive and insensitive parameters of the casting conditions in order to have better control of the membrane properties. Nanoclays with hydrophilic modifiers tended to form membranes with larger macrovoids and higher F_{β} . Out of eight types of nanocomposite membranes, PVDF/I30E membrane had the highest nanoclay retention. Long air retention time had a negative impact on nanoclay retention and additives to the quench bath helped retain nanoclay in the membrane. Despite the slight changes, retentions of nanoparticles within the membrane were in the order of 34% to 48%. Mechanical strength of the membranes was associated with membrane morphology, which was controlled by various casting conditions. Increases

in air retention time, decreases in quench bath temperature and casting at high humidity increased the demixing rate which resulted in membranes with large macrovoids and weak mechanical properties. Addition of 10 wt% of NaCl to the quench bath formed a membrane predominately in PVDF β -phase with high tensile strength but lower ductility and stiffness. It was noted that membranes with poor structure had low values for all measured mechanical properties including tensile strength, ductility and stiffness. For membranes with good structure, depending on the casting conditions, there could be tradeoffs between the mechanical properties. For instance, using higher polymer concentration brought about higher tensile strength but lower ductility. This indicated that casting conditions impacted on particular membrane features. As such, casting conditions should be chosen according to the needs of the application while the desired membrane properties should also be achieved.

7. Enhanced abrasion resistant PVDF/nanoclay hollow fibre composite membranes for water treatment

In this chapter, we proceed to hollow fibre geometry with the knowledge gained from studies on flat sheet membranes in previous chapters. Chapter 6 revealed several conditions for optimal nanoclay retention, such as additives to quench bath and short air retention, which can be applied to the commercial hollow fibre extrusion rig. To add to this, control of the nanoclay dispersion and the composition of the synthesis solution were also established for flat sheets thus leading into hollow fibre fabrication. In Chapter 5, the abrasion resistance of the flat sheet membranes was measured by a standard tribology technique. However, since hollow fibres represent the common membrane format used in water treatment, a more realistic condition abrasion test was developed. This in-house setup involved shaking hollow fibres in an abrasive slurry and periodically measuring bubble point for skin layer breakthrough as described in Section 3.4.8.2. Study on fouling resistance also gave insight on the membrane hydraulic and fouling performance.

7.1. Membrane preparation and characterization

Membranes with various loadings of Cloisite[®] 30B and Nanomer[®] I.44P, and a control membrane which contained 0 wt% nanoclay, were prepared. The membrane composition is listed in Table 3-6 and the detailed fabrication process is described in Section 3.3.3.

The fabricated membranes were characterized by LOI, FTIR, SEM/EDS, water permeability, fouling tests, mechanical testing and abrasion testing with abrasive slurry and bubble point determination. Porosity and average pore size were measured as well. Detailed descriptions of these techniques are described in Chapter 3.

7.2. Results and Discussion

7.2.1 Nanoclay retention by LOI

Table 7-1 shows the fraction of inorganic component of the nanoparticles and nanocomposite membrane as determined by LOI. In all cases, the nanocomposite membranes contained a non-combustible residue that was attributed to the inorganic

component of the added nanoclay and increased with clay loading. As for the nanoclays themselves, 68% of Cloisite[®] 30B and 60% of Nanomer[®] I.44P was not combusted, implying this was the inorganic component of the original nanoclays. These figures match with the weight loss on ignition stated on the supplier's product data sheet for both clays. For the membranes, the original inorganic loading was calculated based on the original nanoclay loading in the dope and the LOI data for the nanoclay that it was made from. Other than the control membrane, all other membranes left a measurable residue after LOI which confirmed the presence of nanoclay in the composite membranes. However, the inorganic amount added to the dope did not match the residual amount measured after LOI for the membranes implying some loss of inorganic particles during membrane formation.

Table 7-1. Comparison between dope and membrane inorganic loading

Name	Dope / supplier inorganic loading %	Inorganic residue %	Standard error of mean
<i>Nanoclays</i>			
Cloisite [®] 30B	70	68	0.5%
Nanomer [®] I.44P	55-65	60	0.5%
<i>Membranes</i>			
0% Nanoclay	0	<0.01	0%
30B 0.88	0.60	0.39	28%
30B 2.61	1.77	0.60	13%
30B 5.08	3.45	0.93	9%
I44P 0.88	0.53	0.30	33%
I44P 2.61	1.56	0.48	14%
I44P 5.08	3.04	0.72	18%

Figure 7-1 presents the retention percentage of nanoclay that has been successfully incorporated into the membranes. It is observed that as the initial clay loading increases, a lower percentage of nanoclay was successfully retained in the formed membrane. This pattern was consistent for both types of nanoclay. However, it is noted that lower loadings yielded larger errors in the analysis. Despite this, there is a statistically significant trend of reduced retention of the nanoclay with increased loading. This may suggest that nanoclay content was approaching a threshold of what

the PVDF matrix could retain. The trend observed here was different from that of PVDF/15A flat sheet membranes in Section 5.2.1. For the flat sheet membranes, all nanoclay retentions were below 24% regardless of the initial loading in the dope. These results showed that hollow fibres in this chapter improved the retention of nanoclay at lower loadings. This could be due to difference in the mixing techniques and the fabrication process. For instance, nanoclays were dispersed by ultrasonication for flat sheets whereas a microfluidizer was used for hollow fibres. Also, flat sheet membranes were hand cast while hollow fibres were fabricated by a spinning machine. The change in observation could also be due to the chemistries of the nanoclays attributed to different organic modifiers.

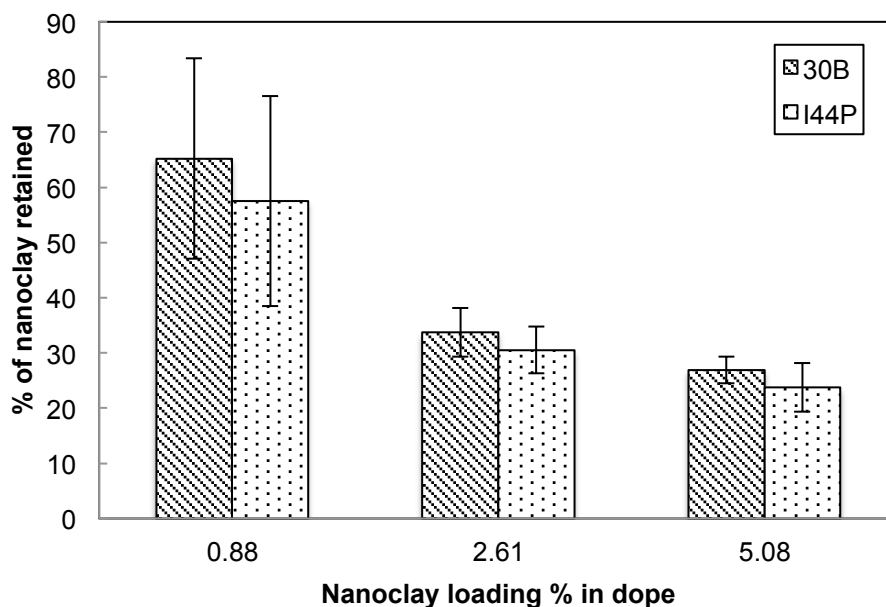


Figure 7-1. Percentage of nanoclay from the NMP solution retained in the membranes

7.2.2 Effect of nanoclay on membrane material crystal structure

The FTIR spectra of 0% Nanoclay and composite membranes are shown in Figure 7-2(a) and Figure 7-2(b) for 30B and I44P respectively. Our results showed strong peaks at 763 cm^{-1} and 796 cm^{-1} corresponding to the α -phase of PVDF, as well as at 840 cm^{-1} corresponding to the β -phase of PVDF [53, 122]. The α -phase peak intensity decreased alongside an increase in the β -phase peak for the nanocomposite membrane samples. This was attributed to the change in PVDF crystal phases during membrane formation and was similar to observations in Chapters 5 and 6 when nanoclay was incorporated into flat sheet membranes.

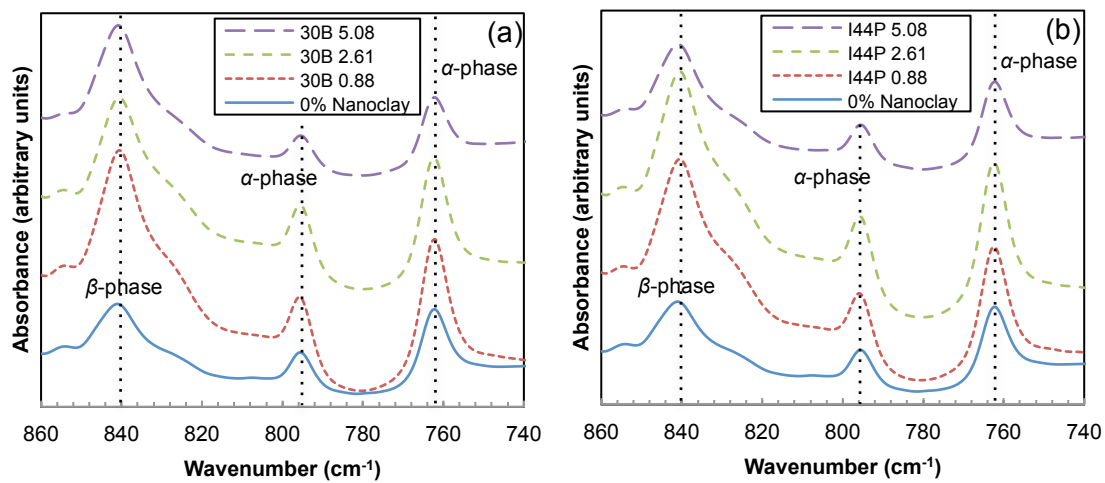


Figure 7-2. FTIR spectra of membranes incorporated with Cloisite® 30B (a) and Nanomer® I.44P (b)

Table 7-2 presents the beta fraction, F_{β} , of the membranes which was calculated using Equation (3) based on the peak areas of the absorption peaks of α -phase and β -phase at 763 cm^{-1} and 840 cm^{-1} respectively. It was observed that the composite membranes have higher F_{β} values than the control membrane, indicating there is a higher ratio of the β crystalline form present in the composite membranes. This result matches those in the literature [53, 90, 109, 113]. It was also noted that despite similar initial nanoclay loading, flat sheet membrane with 5 wt% of nanoclay in Chapter 6 showed different F_{β} values. F_{β} of flat sheet membranes PVDF/30B 5% and PVDF/I44P 5% was 0.97 and 0.45 respectively. The difference in F_{β} between hollow fibre and flat sheet was likely due to the difference in the fabrication process.

Table 7-2. F_{β} of membranes

Membrane	F_{β}
0% Nanoclay	0.39
30B 0.88	0.48
30B 2.61	0.47
30B 5.08	0.64
I44P 0.88	0.50
I44P 2.61	0.48
I44P 5.08	0.51

Figure 7-3 shows the plot of actual nanoclay loading determined by LOI in Section 7.2.1 against F_{β} of the membranes. It appeared that Cloisite® 30B had a stronger linear correlation than Nanomer® I.44P in promoting F_{β} by increasing its loading. Membranes incorporated with I.44P seemed to have a limit of maximum F_{β} that could be achieved. This may be important if PVDF β -phase is the key property to durability enhancement.

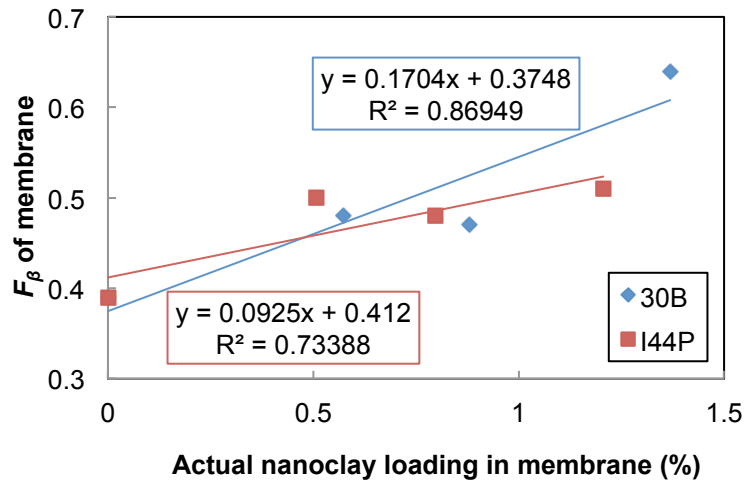


Figure 7-3. Actual nanoclay loading vs F_{β} of membranes.

7.2.3 Effect of nanoclay on membrane morphology

Membrane morphological analyses by SEM and EDS were carried out to study the membrane structure and to determine the extent of the nanoclay dispersion. Images of the cross-section and the membrane outer surface are shown in Figure 7-4 and Figure 7-5 respectively. The images show typical asymmetric structures with sponge layer together with finger-like voids supporting a thin skin layer on the outer surface. The skin layer is for the functional separation process of the membrane. It was observed in the overall membrane cross-sectional images that as the nanoclay content increased, the length of finger-like voids reduced and the membrane structure appeared to be more uniform. This is opposite to the observation with the PVDF/15A flat sheet membranes in Chapter 5. Apart from different techniques to disperse nanoclay (ultrasonication for flat sheet and microfluidizer for hollow fibres), the change in morphology could be due to the different types of nanoclay used in both studies and/or that the difference between hollow fibre extrusion and flat sheet casting has changed

the nanoclay interaction with the PVDF. Here, the nanoclays may slow down the liquid-liquid demixing process and suppress macrovoid formation.

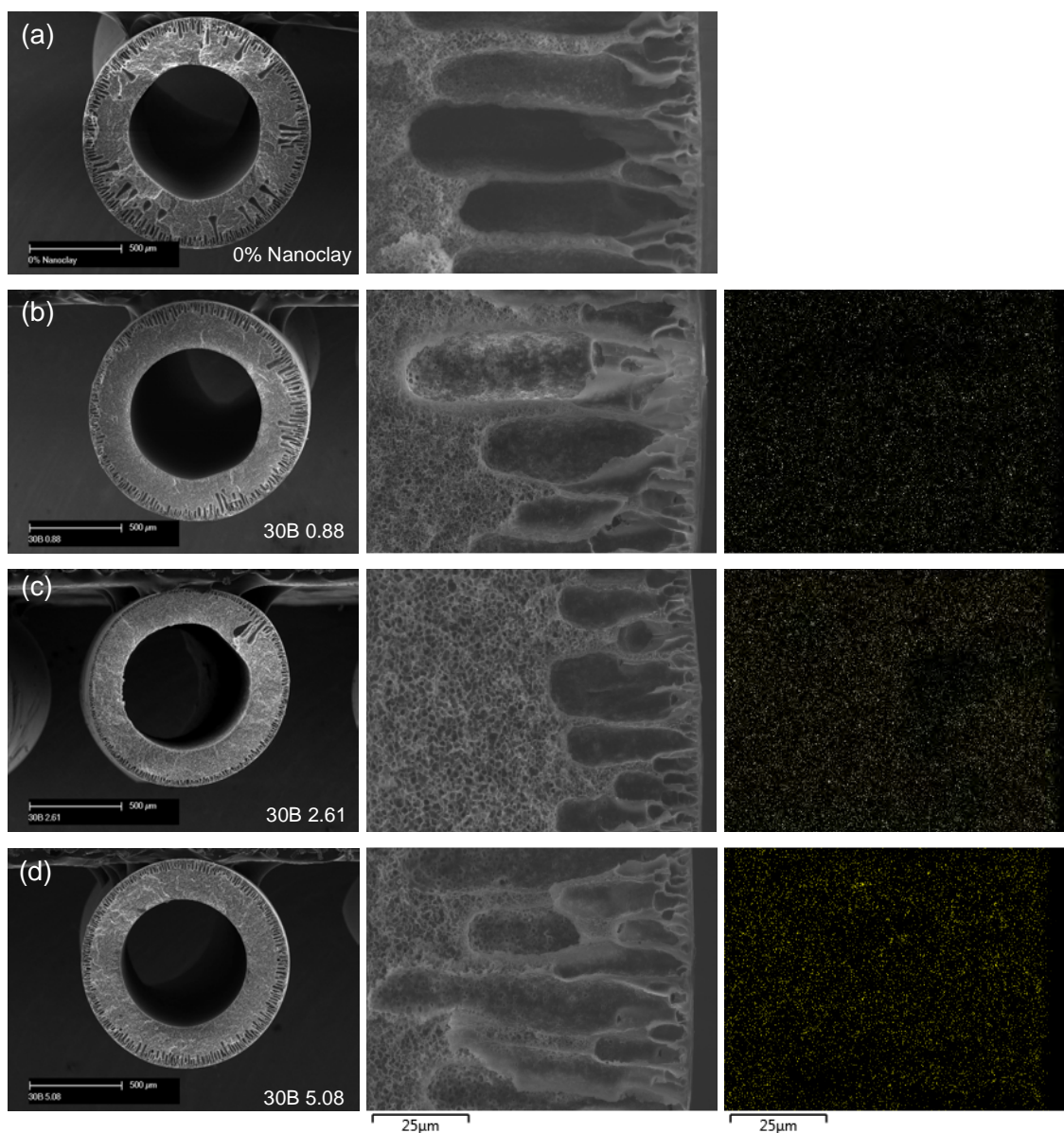


Figure 7-4. SEM and X-ray Si mapping images using EDS of membrane cross-section: (a) 0% Nanoclay, (b) 30B 0.88, (c) 30B 2.61, (d) 30B 5.08, (e) I44P 0.88, (f) I44P 2.61 and (g) I44P 5.08

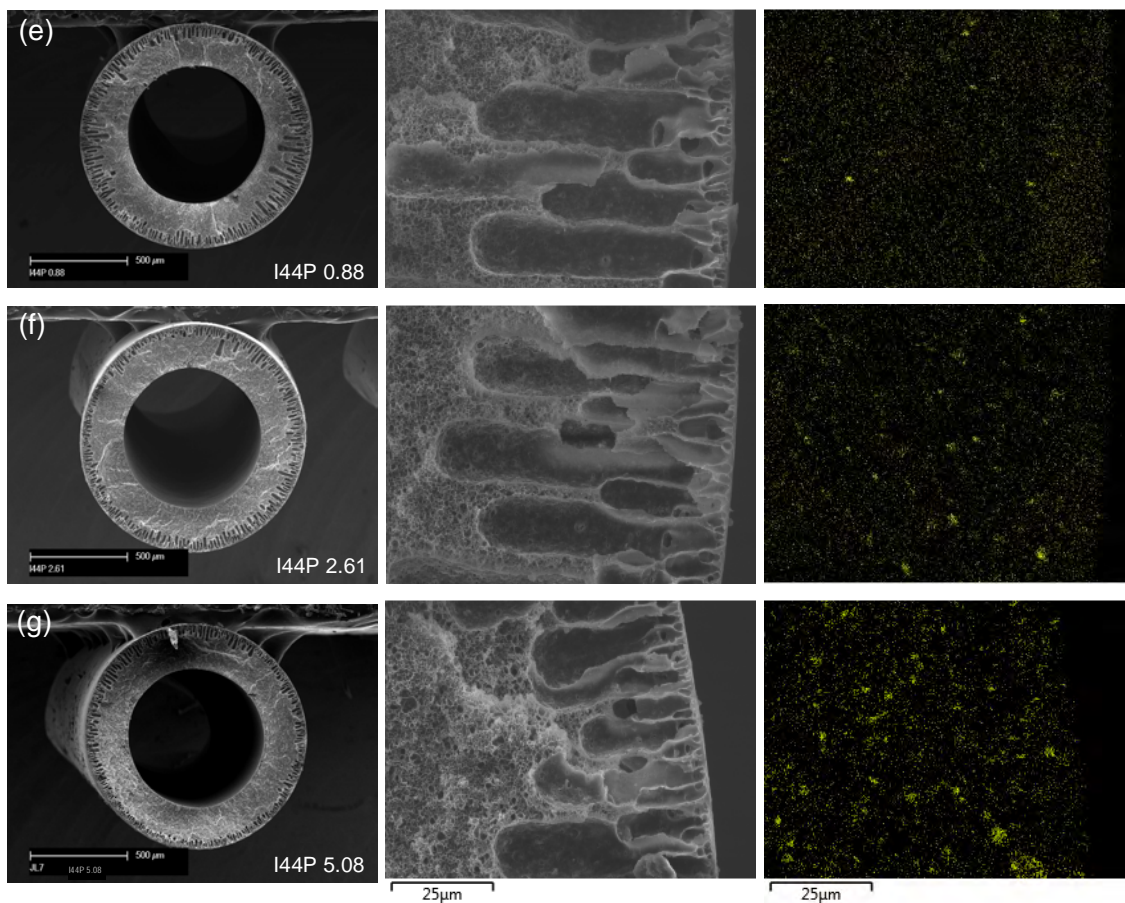


Figure 7-4. SEM and X-ray Si mapping images using EDS of membrane cross-section: (a) 0% Nanoclay, (b) 30B 0.88, (c) 30B 2.61, (d) 30B 5.08, (e) I44P 0.88, (f) I44P 2.61 and (g) I44P 5.08

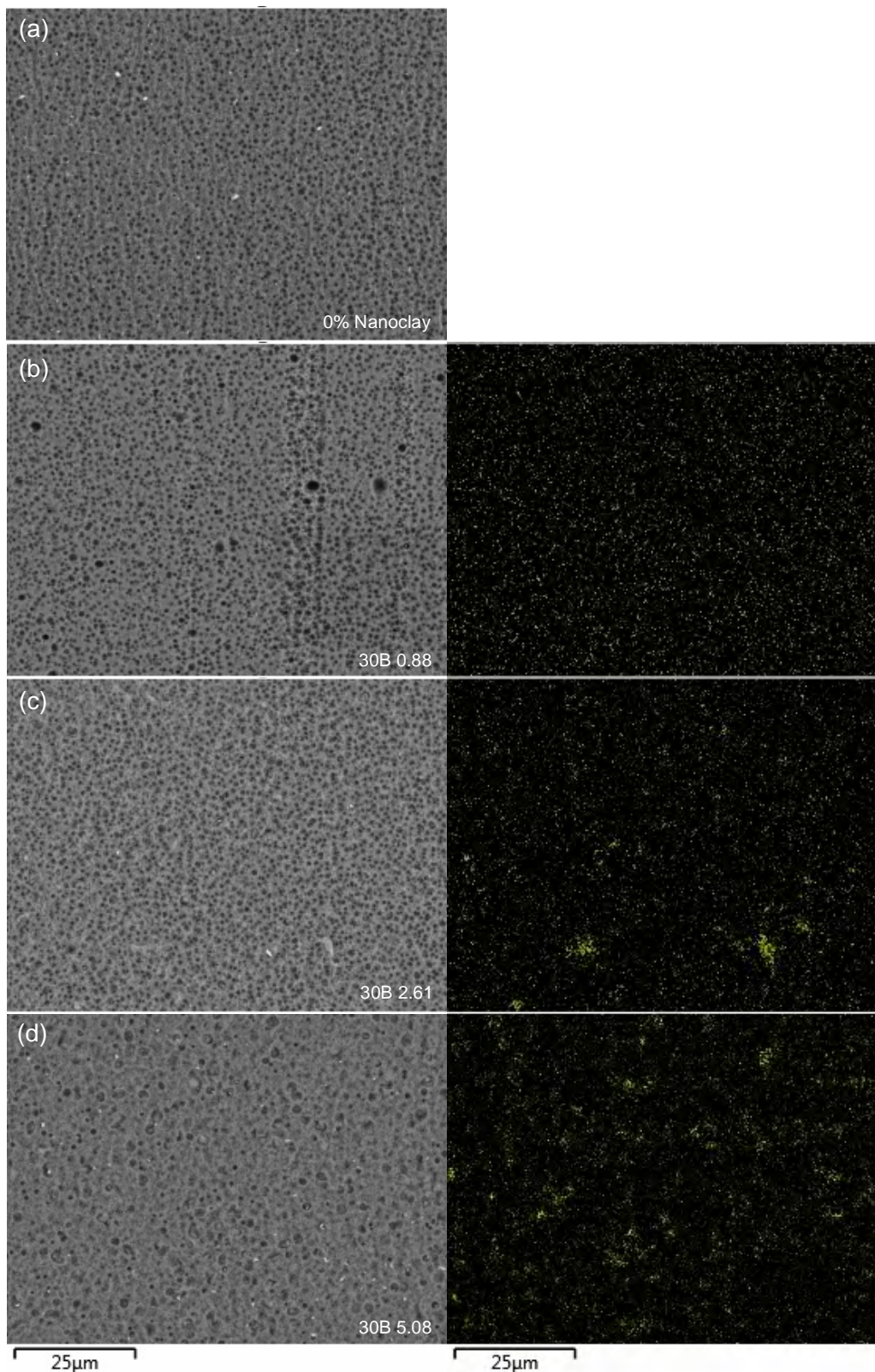


Figure 7-5. Backscattering SEM and X-ray Si mapping images using EDS of membrane outer surface: (a) 0% Nanoclay, (b) 30B 0.88, (c) 30B 2.61, (d) 30B 5.08, (e) I44P 0.88, (f) I44P 2.61 and (g) I44P 5.08

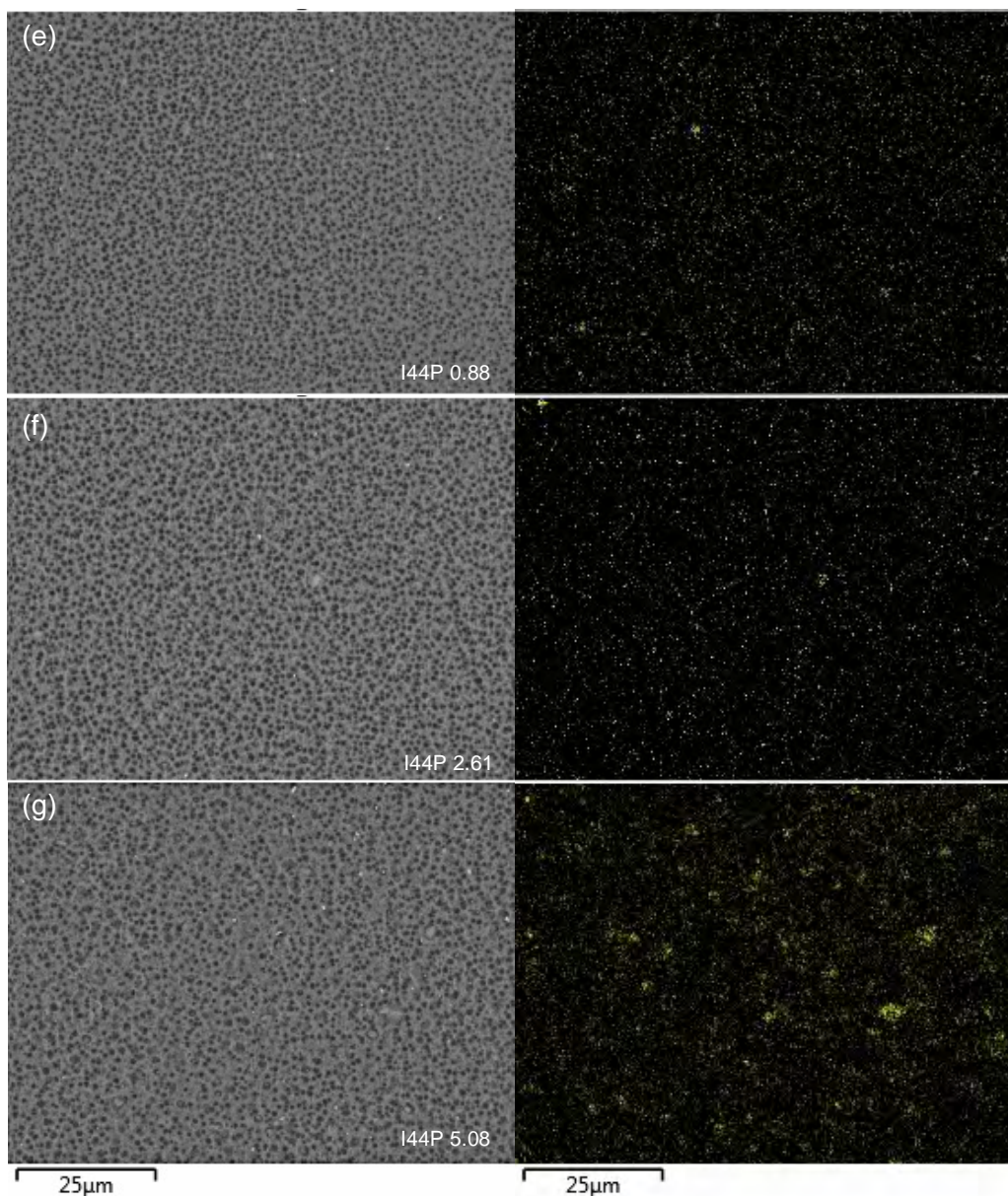


Figure 7-5. Backscattering SEM and X-ray Si mapping images using EDS of membrane outer surface: (a) 0% Nanoclay, (b) 30B 0.88, (c) 30B 2.61, (d) 30B 5.08, (e) I44P 0.88, (f) I44P 2.61 and (g) I44P 5.08

Silicon mapping with EDS was used to show the nanoclay distribution in membrane surface and cross section. As the nanoclay loading increases, it is seen in Figure 7-4 and Figure 7-5 that the intensity of silicon detection also increases. Cloisite[®] 30B appears to be more finely dispersed than Nanomer[®] I.44P as evidenced by larger agglomerates being present in the I.44P membranes. This could be attributed to the presence of OH group in the organic modifier of Cloisite[®] 30B (Table 3-2) which improves its dispersion in NMP because it is a polar solvent. Also, the Z-average size

of the Cloisite[®] 30B and Nanomer[®] I.44P dispersions, which is the intensity-weighted mean diameter derived from the cumulants analysis by the particle sizer, was found to be 231 nm and 867 nm respectively. These measurements are comparable to the larger particle cluster size observed in the EDS mapping images (271 nm for 30B and 802 nm for I.44P), which confirmed that Cloisite[®] 30B was more finely dispersed. This may be the reason why I.44P was less able to form β -phase PVDF at high nanoclay loading as there was less effective surface area for I.44P added compared to 30B.

Table 7-3 presents the membrane porosity, the average outer surface pore size, the overall membrane thickness and the skin layer thickness. Overall, the porosity of the membranes was about 80% and the addition of nanoclay appeared to have no significant impact. For the average pore size measured from SEM images of the outer membrane surface, the membranes had pores ranging from 0.61 μm to 0.68 μm . Once again the nanoclay did not appear to alter the average surface pore size. The overall membrane thickness and the thickness of the skin layer of the membranes were average values taken from at least five measurements using the SEM cross-sectional images. The membranes had an overall thickness of 210 μm on average. It was observed that 0% nanoclay membranes had a thicker skin layer than the nanocomposites at lower nanoparticle loadings, but the skin layer thickness increased to similar values as the 0% nanoclay loading at the highest nanoclay loadings.

Table 7-3. Membrane porosity, overall and skin thickness determined by SEM cross section measurement and average pore size determined by SEM surface measurement.

Membrane	Porosity (%)	Average pore size (μm)	Overall thickness (μm)	Skin layer thickness (μm)
0% Nanoclay	80 \pm 2	0.66 \pm 0.09	204 \pm 16	0.81 \pm 0.12
30B 0.88	81 \pm 3	0.66 \pm 0.11	214 \pm 19	0.47 \pm 0.07
30B 2.61	80 \pm 3	0.63 \pm 0.09	218 \pm 31	0.45 \pm 0.05
30B 5.08	77 \pm 2	0.68 \pm 0.08	197 \pm 9	0.93 \pm 0.09
I44P 0.88	80 \pm 3	0.64 \pm 0.10	226 \pm 30	0.41 \pm 0.05
I44P 2.61	82 \pm 2	0.66 \pm 0.10	218 \pm 26	0.54 \pm 0.08
I44P 5.08	81 \pm 2	0.61 \pm 0.08	217 \pm 9	0.62 \pm 0.03

7.2.4 Pure water permeability

The impact of Cloisite® 30B and Nanomer® I.44P loading on water permeability was investigated and the results are presented in Figure 7-6.

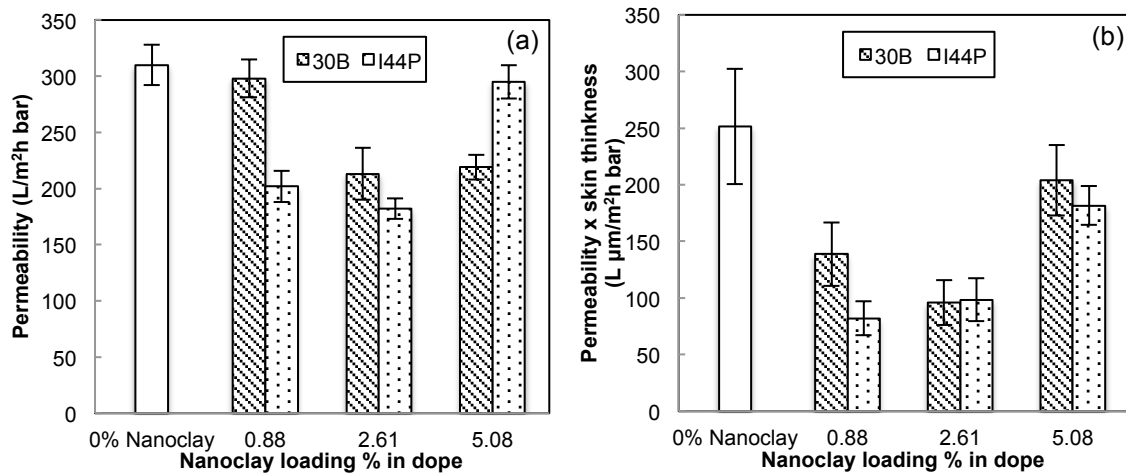


Figure 7-6. Impact of nanoclay on (a) overall water permeability and (b) permeability times skin thickness (material permeability)

From Figure 7-6(a), nanoclay tends to reduce the membrane permeability in general compared to membranes with no nanoclay, but the trend with nanoclay concentration varies. The exceptions to the reduced permeability trend are the 30B 0.88 and I44P 5.08. To account for the variation of membrane skin thickness, which is assumed to be the highest resistance layer of the membrane, the product of permeability and skin thickness was plotted against the nanoclay loading in Figure 7-6(b). It was shown that the addition of nanoclay, especially at lower loadings, reduced the water permeability of the membranes once variations in skin layer thickness were accounted for. This observation is opposed to the increased water flux achieved when TiO₂ or a combination of TiO₂, SiO₂ and Al₂O₃ was incorporated into PVDF UF hollow fibre membranes [26, 94, 95] although the variations in skin thickness were not accounted for in these studies. It is possible that these nanoparticles have higher hydrophilicity than the nanoclay used in this study, so that water was able to wet the membrane and flow through the membrane more easily than when nanoclay was present. Also, the nanoparticles used in the previous studies were spherical and much smaller than the membrane pore size. For instance, the size of TiO₂ particles in the PVDF/TiO₂ 1 wt% membrane was 25 nm and the average pore size was 0.18 µm [26]. In this study, the average pore size of the membranes was about 0.65 µm where the length of the

nanoclay platelets was up to few hundreds nm. The larger size of the nanoclay clusters was also evident from the EDS images in Figure 7-5. The reduced flux could be because some of the nanoclay particles were blocking the pores.

Alternatively, the decreasing permeation values with addition of nanoclay suggest that alteration of the membrane formulation with various nanoclay loadings alters the membrane morphology that relates to water transport. Besides membrane skin thickness, the contact angle, pore size, tortuosity and skin porosity also influence water permeability and the addition of nanoclay appears to have also influenced some of these features. In our work, permeability testing provided an indication of the membrane hydraulic performance, which is also an important factor besides aiming to improve the mechanical strength and the abrasion resistance of the membranes.

7.2.5 Membrane fouling studies

Filtration with BSA and sodium alginate solutions was carried out to study membrane fouling. Figure 7-7 shows the change of TMP of the 0% Nanoclay membrane during BSA filtration. In each filtration cycle lasting 30 minutes, it was observed that the TMP gradually increased as foulant built up on the membrane surface and blocked water transport. The sharp drop in TMP represents the commencement of backwashing which flushed off foulant from the membrane surface. At the beginning of the experiment, backwashing was effective to restore the TMP to the original level. However, as the filtration progressed, TMP increased despite the same backwashing frequency indicating irreversible fouling took place.

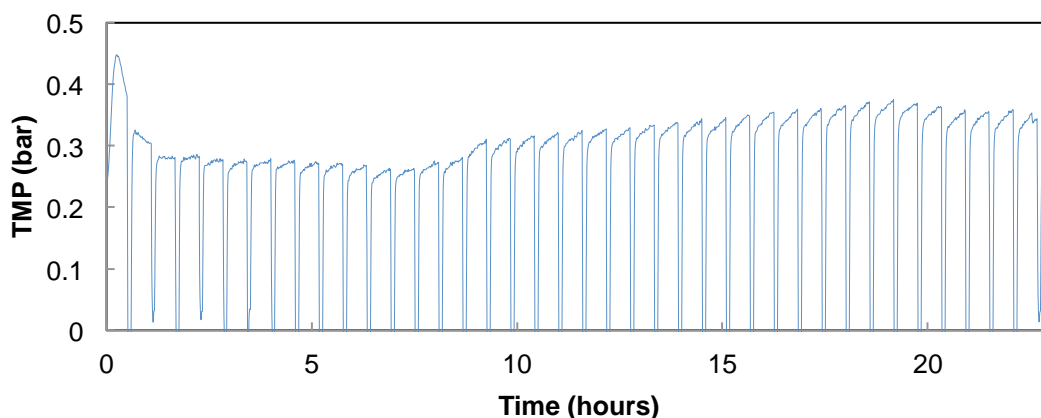


Figure 7-7. TMP of 0% Nanoclay membrane during BSA filtration using 100 ppm BSA, 450 ppm NaCl, 50 ppm CaCl₂ at 50 L/m²h, 20°C.

Figure 7-8 shows the TMP profiles of the membranes immediately after backwashing during BSA filtration. It was noticed that the membranes had different starting TMP and it was likely attributed to varying membrane surface properties. The initial decrease in TMP (from 0 to 5 hours) could be due to insufficient wetting of the membranes. As time progressed, it was observed that the membranes had relatively small change in absolute TMP, indicating the nanocomposite membranes were not more prone to fouling than the unmodified membrane.

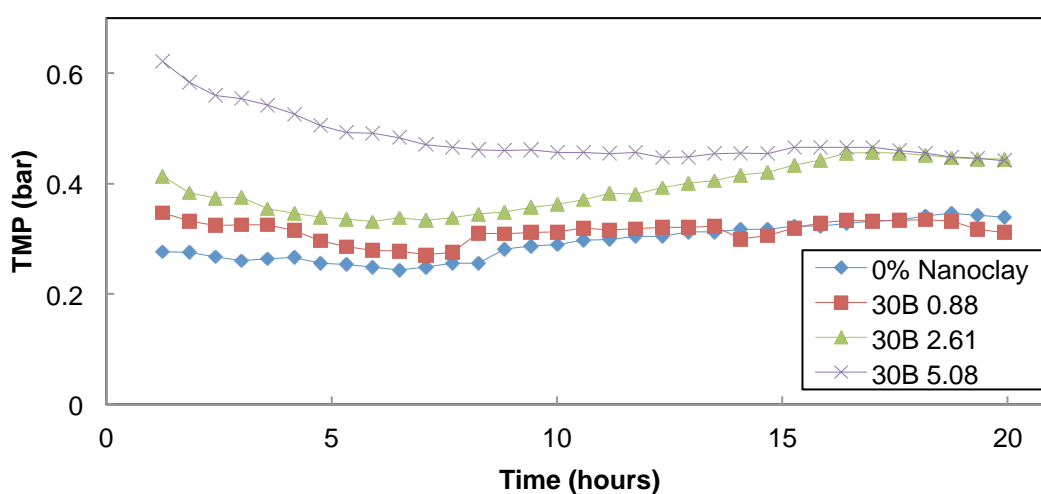


Figure 7-8. TMP after backwashing during BSA filtration using 100 ppm BSA, 450 ppm NaCl, 50 ppm CaCl₂ at 50 L/m²h, 20°C.

As the membranes had different initial TMP, relative TMP was also used to compare the fouling rate of the membranes. Relative TMP of the 0% Nanoclay and Cloisite® 30B nanocomposite membranes after backwashing during BSA and alginate filtrations are presented in Figure 7-9. Data points immediately after backwashing were used to represent the degree of irreversible fouling. As it took time for the membrane filtration to run consistently, the reference TMP was taken after several hours (5.75 hours for BSA and 7.5 hours for alginate) into filtration.

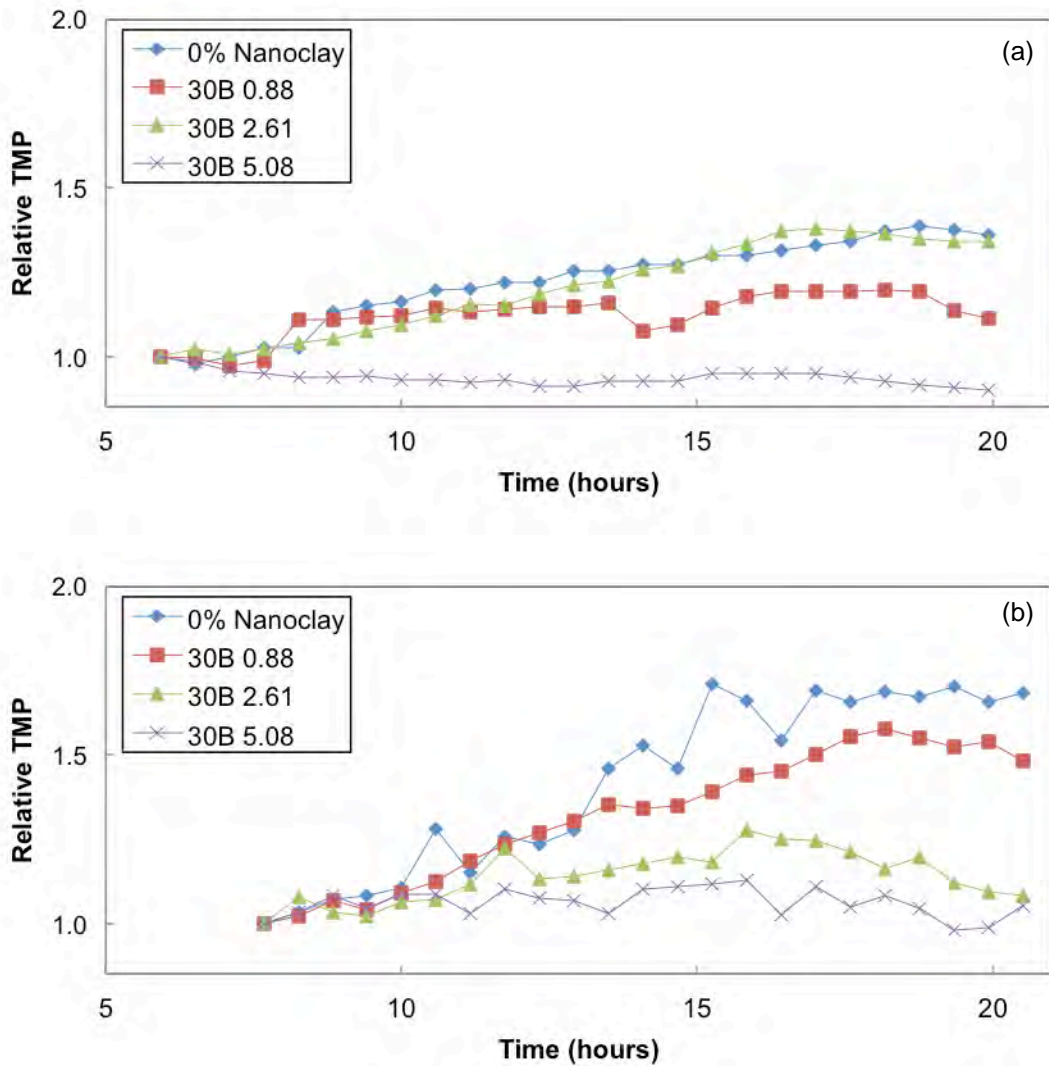


Figure 7-9. Relative TMP of membranes after backwashing during (a) BSA filtration using 100 ppm BSA, 450 ppm NaCl, 50 ppm CaCl₂ at 50 L/m²h, 20°C and (b) alginate filtration using 100 ppm sodium alginate, 450 ppm NaCl, 50 ppm CaCl₂ at 50 L/m²h, 20°C.

In general, membranes were more susceptible to alginate fouling than BSA as shown by the faster rate of pressure increase. With BSA as the foulant (Figure 7-9(a)), 30B 0.88 and 30B 5.08 had lower relative TMP than 0% Nanoclay and 30B 2.66 membranes which showed a similar rate of fouling to the 0% membrane. Although the difference in change in absolute TMP (Figure 7-8) among the membranes was less significant, this at least inferred that nanocomposite membranes were not more prone to fouling and may be more fouling resistant as suggested by the relative TMP. For the case of alginate fouling (Figure 7-9(b)), it was clear that the unmodified membrane had the highest rise of relative TMP and the rate decreased as the nanoclay loading

increased, indicating the antifouling performance was enhanced. Overall, 30B 5.08 was the best performing membrane, showing little change in relative TMP during filtration with both foulants. The fouling results did not appear to associate with the physical changes observed by SEM in Section 7.2.3. It was likely that the incorporation of nanoclay has changed the surface chemistry of the membrane and hence the interaction with the foulants. PVDF/SiO₂ hollow fibre membranes prepared by Yu *et al* [25] showed the PVDF β -phase crystallinity was directly proportional to the membrane hydrophilicity as measured by XRD and contact angle respectively. Higher hydrophilicity is often linked to improved anti-fouling properties as it affects the surface energy and affinity properties of the membranes and minimises the interaction between the foulant and the membrane surface [148]. This may explain the best anti-fouling performance of 30B 5.08 given it had the highest F_{β} shown in Table 7-2.

While other researchers improved membrane anti-fouling properties by incorporating nanoparticles such as SBA-15, TiO₂ and Al₂O₃ [22-24], this study has shown that commercial nanoclay can also enhance this property. Also, those previous studies measured flux reduction under constant pressure and did not incorporate backwashing in their fouling testing. Although the flux declined as the fouling material built up on the membrane surface, it did not necessarily represent the degree of irreversible fouling without backwashing. This study made use of filtration under constant flux with automated backwashing which resembled a more realistic filtration setup. However based on the results presented here, the test would need to be conducted for a sufficiently long time (days or longer) to clearly see any antifouling properties.

While nanoclay could possibly bring a positive impact to mechanical properties and abrasion resistance, this study has confirmed that the nanocomposite membranes were not more prone to fouling, in fact the nanoclay may enhance the membrane antifouling performance especially at high nanoclay loading.

7.2.6 Mechanical properties

The testing results of mechanical properties including tensile strength, elongation at maximum load and Young's modulus are listed in Table 3-5. In general, small amounts of nanoclay tended to weaken the mechanical performance but improvement in mechanical properties was observed for membranes with higher nanoclay loading. The 30B 5.08 membrane demonstrated increased tensile strength and Young's modulus from 3.8 MPa to 4.3 MPa and from 63 MPa to 84 MPa respectively. This

indicated that the introduction of Cloisite® 30B provided extra stiffness to the polymer matrix. Hwang *et al* [83] also observed improved tensile strength (15 MPa to 24 MPa) and Young's modulus (22 MPa to 42 MPa) with their PVDF/1wt% Cloisite® 30B flat sheet membrane. Furthermore, the I44P 5.08 membrane resulted in improved break extension from 175% to 229%, indicating the composite membrane had extra ductile strength. It was interesting to note that the membranes with I44P exhibited increased ductility while 30B exhibited increased stiffness.

Table 7-4. Mechanical properties of membranes

Membrane	Tensile strength, σ (MPa)	Elongation at max load, ϵ (%)	Young's modulus (MPa)	$\sigma\epsilon$ (MPa)
0% Nanoclay	3.78 \pm 0.19	175 \pm 15	63 \pm 6	6.62 \pm 0.90
30B 0.88	3.46 \pm 0.14	165 \pm 23	60 \pm 4	5.71 \pm 1.03
30B 2.61	4.06 \pm 0.11	186 \pm 7	73 \pm 3	7.55 \pm 0.49
30B 5.08	4.30 \pm 0.28	161 \pm 28	84 \pm 10	6.92 \pm 1.65
I44P 0.88	3.16 \pm 0.12	171 \pm 12	55 \pm 2	5.40 \pm 0.58
I44P 2.61	3.48 \pm 0.11	157 \pm 7	61 \pm 2	5.46 \pm 0.42
I44P 5.08	3.84 \pm 0.12	229 \pm 13	65 \pm 3	8.79 \pm 0.77

It appears that by using different types of nanoclay, different aspects of the mechanical properties can be altered. This is similar to the investigation in Chapter 6, whereas variation in casting conditions could bring about change in mechanical properties. One reason for the improved mechanical properties can be attributed to the suppression of the macrovoids in the membranes with higher nanoclay loading. Also, nucleation of the fibre-like PVDF β -phase on the faces of individual silicate layers of the nanoclay brings about a structure which is more favourable to plastic flow under applied stress. This results in a more efficient energy-dissipation mechanism in the composite membrane as illustrated in Figure 7-14, which has been shown in previous PVDF/nanoclay nanocomposite material studies to delay cracking [53]. In addition, nanoclay can act as a temporary crosslinker to the polymer chain given their size and mobility are comparable. This provides localized regions of increased strength and inhibits the development of cracks and cavities [90].

7.2.7 Abrasion resistance

Abrasion testing utilised bubble point measurements (Section 3.4.8.2) to determine membrane degradation. The initial bubble points for the nanocomposite membranes are shown in Table 7-5. We see that initially the bubble points varied in the range of 275 kPa to 487 kPa, corresponding to membranes having a largest pore size in the range of 1.0 μm to 0.6 μm respectively determined by Equation (5). Comparing these values with the average pore size in Table 7-3, most of them match with the upper range of error showing that the assumptions of the contact angle and the pore shape correction factor for Equation (5) were valid. There may be an overestimation for the maximum pore size of 30B 2.61, as the most conservative conditions were used for the maximum pore size calculation. Overall, it appears that maximum pore size and bubble points were not significantly altered due to nanoclay addition (bubble point \sim 390 kPa) except for 30B 2.61 being the lowest (275 kPa) and I44P 5.08 being the highest (487 kPa). Figure 7-6(b) shows that the permeability of the material decreased with nanoclay addition due to some added resistance of the material. It is interesting to note that despite this increased resistance, 30B 2.61 had the largest maximum pore size. On the other hand, I44P 5.08 had the smallest maximum pore size but a lower reduction to material permeability (water resistance). While this implies 30B 2.61 broadened pore size distribution and I44P 5.08 narrowed, such a conclusion is not firm considering other material parameters are likely to change due to nanoparticle addition (e.g. hydrophobicity, tortuosity and pore geometry), and must be known to relate permeation results to the maximum pore size. In any case, the results in Table 7-5 indicate the initial maximum pore size prior to observing changes in the material as a result of abrasion.

Table 7-5. Initial bubble point and corresponding maximum pore size of membranes

Membrane	Bubble point (kPa)	Maximum pore size (μm)
0% Nanoclay	378 \pm 6	0.8
30B 0.88	393 \pm 25	0.7
30B 2.61	275 \pm 28	1.0
30B 5.08	385 \pm 21	0.8
I44P 0.88	390 \pm 13	0.8
I44P 2.61	398 \pm 32	0.7
I44P 5.08	487 \pm 32	0.6

The relative bubble point and maximum pore size calculated according to Equation (5) during the abrasion period is presented in Figure 7-10(a) and (b) respectively.

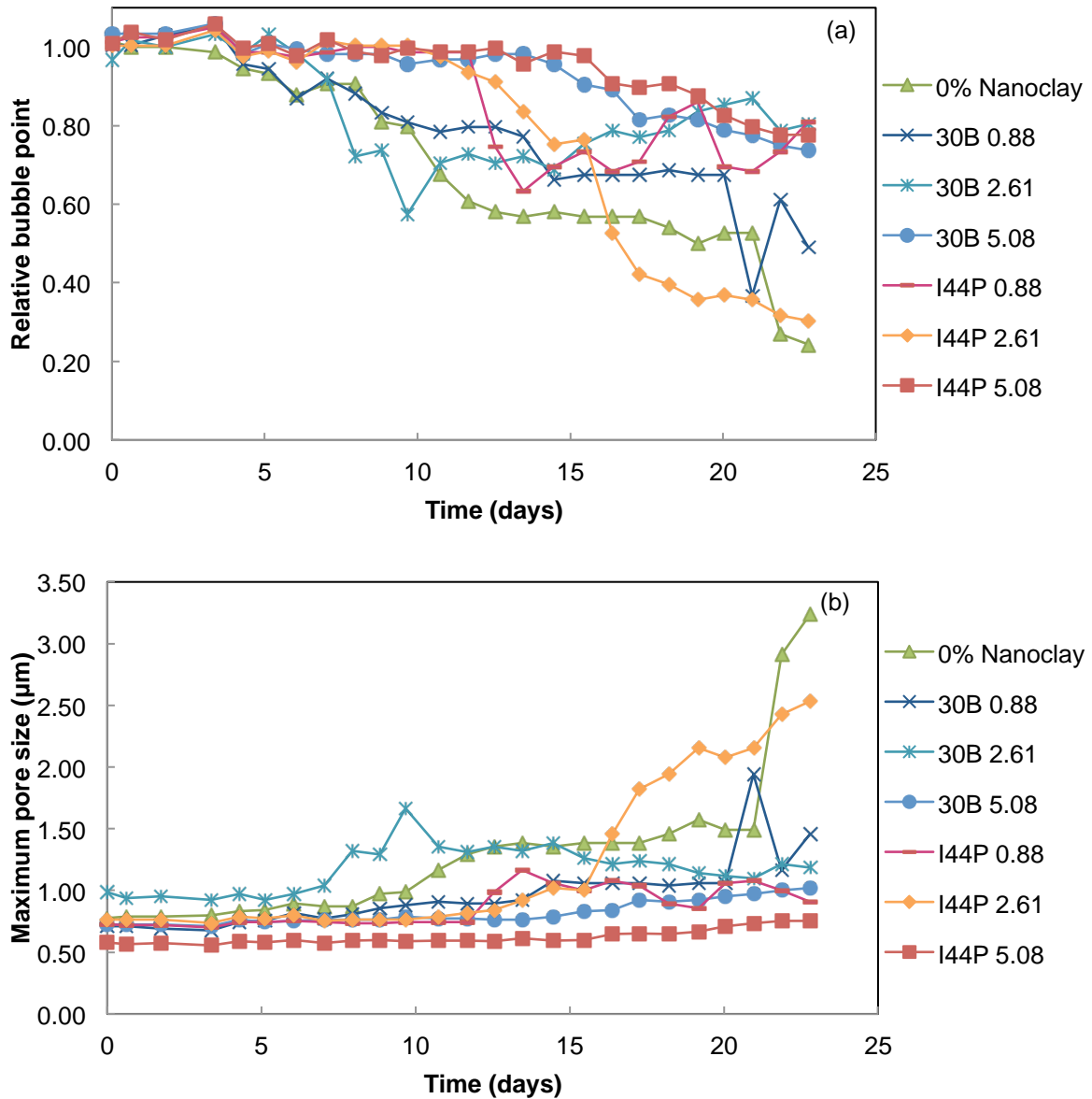


Figure 7-10. Relative bubble point (a) and maximum pore size (b) of the membranes during the abrasion test

From Figure 7-10(a), it was observed that the bubble point of the nanocomposite membranes progressively decreased and reached a plateau while that of the 0% Nanoclay membrane continued to drop to a second plateau after 21 days. As the bubble point is directly related to the maximum pore size of the membrane, it can be interpreted that the first step refers to the maximum pore size on the skin surface. As

the skin surface becomes abraded, the underlying sponge layer becomes exposed and pore size suddenly increases once it has been penetrated as indicated by the step-wise drop in bubble point. The decrease is flattened at the second step which refers to the larger pore size of the supporting sponge layer of the membrane. Figure 7-10(b) shows the calculated maximum pore size based on an ideally hydrophilic membrane with perfectly cylindrical pores. Although it may not reflect the actual pore size, it provides an indication of how the maximum pore size changed under abrasive wear. As mentioned above, the two-step graph is attributed to the different pore size of the skin layer and the more open sponge layer. In general, we see that maximum pore sizes between 0.6 and 1.0 μm increase to 1.5 μm at the first plateau. The 0% and 2.6% I.44P nanoclay membrane subsequently increased in maximum pore size ($> 2.5 \mu\text{m}$) towards the end of the experiment indicating larger pores in the supporting layer were starting to become exposed. Overall, the decreasing bubble point represents the gradual wear of the skin layer of the membrane.

A 10% decrease from its initial bubble point has been considered as an indication of significant abrasive wearing. It is shown in Figure 7-11 that the bubble point of control membrane (0% Nanoclay) dropped at least 10% after 6 days of abrasive wear while it took a longer abrasion period (more than 12 days) for the majority of nanocomposite membranes to exhibit the same drop in bubble point. The maintenance of the initial bubble point suggests the maximum pore size of the membrane remained unchanged. This infers a stronger abrasion resistance demonstrated by nanocomposite membranes.

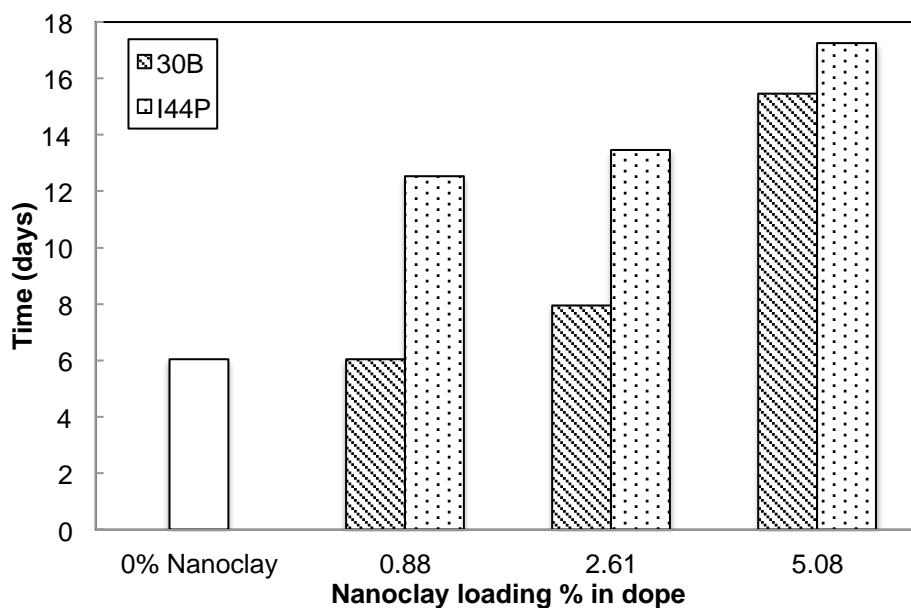


Figure 7-11. Time taken for 10% decrease in bubble point on abraded membranes

Of all membranes, I44P 5.08 had the strongest abrasion resistance which took more than 17 days for 10% decrease from its initial bubble point. This suggests that the nanocomposite membrane can last three times longer than a conventional unmodified membrane under the same abrasive conditions and would be a candidate material for filtration in more abrasive conditions. In the previous study on flat sheet membrane (Chapter 5), the best performing nanocomposite membrane lasted two times longer than unmodified membrane. The similar results in both studies infer that the in-house abrasive slurry test is a reasonable method to test materials for improved abrasion resistance.

It is also noted that the membranes become more abrasion resistant as the nanoclay loading increases, regardless of the type of nanoclay being incorporated. Membranes with Nanomer[®] I.44P appear to have stronger abrasion resistance compared to those with Cloisite[®] 30B, even at lower loadings.

SEM images of the abraded 0% nanoclay and I44P 5.08 membranes are shown in Figure 7-12. The abraded I44P 5.08 membrane appears to be smoother with less pitting in the surface compared to the control membrane after the completion of the 23-day abrasion test.

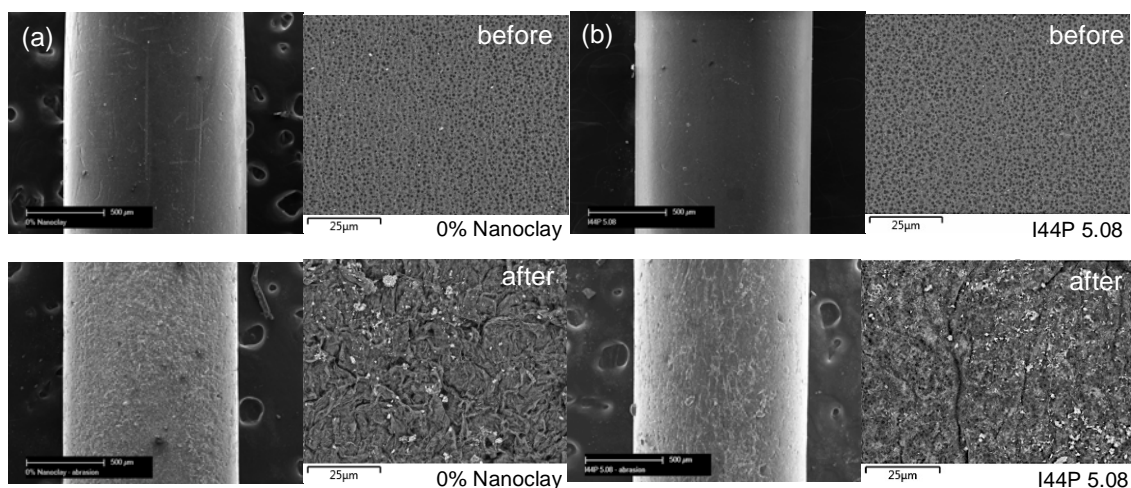


Figure 7-12. SEM images of membrane surface before and after the abrasion test: (a) 0% Nanoclay and (b) I44P 5.08

Figure 7-13 presents the abrasion rate of the skin layer. The time taken for the abrasion of the entire skin layer was assumed to be the time taken to reach the second plateau in Figure 7-10(a) from the start of abrasion. Taking the skin layer thickness determined by SEM (Table 7-3) into account, it is confirmed that the nanocomposite membranes (except 30B 2.61 and 30B 5.08) have stronger abrasion resistance as they showed a slower abrasion rate than the control membrane. The membrane with Nanomer[®] I.44P was also proven to be the stronger material to withstand abrasive wear. Interestingly, the rate of abrasion was constant for this material indicating the improvement with increased loading was related to the increased thickness of the membrane skin layer. The I44P 0.88 membrane appeared to be the most efficient given the high nanoclay retention and also the strong abrasion resistance. In the case of Cloisite[®] 30B, abrasion resistance appeared to decrease with increased nanoclay loading. This is an interesting result, as it shows that the reason why 30B improved abrasion resistance at higher loading (Figure 7-11) was because its addition only increased the skin layer thickness (Table 7-3). It was possible that the material's wear resistance was higher at the 0.88 lower loading (Figure 7-13), but this was compromised by thinner skin layers. Therefore, the Cloisite[®] 30B material itself imparted no practical improved abrasion resistance as the nanoclay loading increased.

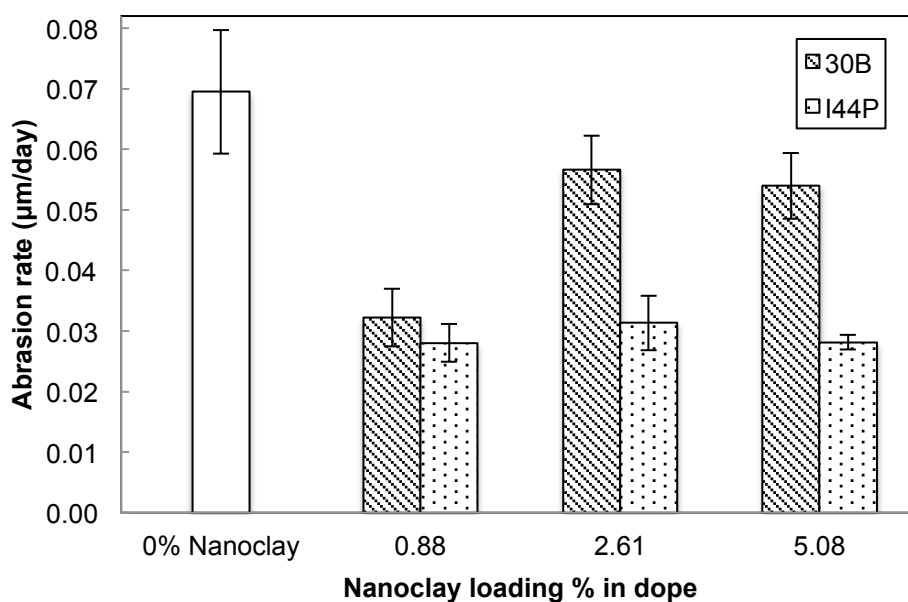


Figure 7-13. Abrasion rate normalised by membrane thickness

It was shown from mechanical testing (Table 3-5) that I44P 5.08 had the longest elongation at max load, which suggests its ductile strength helps to resist the damage from the abrasive particles. Also, the polymer phase trends in Table 7-2 suggest that I44P's increased abrasion resistance could be due to more β -phase PVDF. As the nanoclay enhances the PVDF phase change from α to β -phase, the material changes from less polar to more polar [90]. This increases the binding energy between macromolecule chains and improves abrasion resistance as the membrane surface is less likely to peel off [90]. However, this conclusion is weakened on comparing results between nanoclays, since the material with the higher β -phase contribution (Cloisite[®] 30B) was not the material with the highest abrasion resistance. As such, materials that achieve higher proportions of β -phase must also have the required physical properties (e.g. 30B membranes had lower ductile strength). Also, although Cloisite[®] 30B appears to be more well dispersed within the membrane, the abrasion testing has shown that the membranes modified with Nanomer[®] I.44P, which was less homogeneously dispersed, had stronger abrasion resistance. This may be explained by the different organic functionalization of the nanoclay playing a more significant role to the polymer matrix than the actual dispersion in maintaining the abrasion resistance of the membrane.

According to the abrasion theory proposed by Ratner *et al* [116], it is necessary to have both high tensile strength and high ductile strength (elongation) in order to achieve a low abrasion rate based on Equation (1). From the product of tensile

strength and elongation at max load ($\sigma\varepsilon$) values listed in Table 3-5, membrane I44P 5.08 has the highest value which affirms its strongest abrasion resistance. However, not all the values, especially those with low nanoclay loading, fit this correlation. One possible explanation for this discrepancy is that the abrasion theory was developed based on uniform bulk material performance, while the membranes have porous and asymmetric morphology. While only the surface properties account for the abrasion resistance, the entire membrane structure contributes to tensile strength and ductile strength. As such, it may not be entirely accurate to relate these properties directly. Also, the abrasion theory was based on pure polymer which may not completely match the wear mechanism for nanocomposite materials.

A model of abrasion resistance based on our findings is proposed in Figure 7-14. This incorporates both the energy dissipation mechanism due to PVDF phase change, as well as the presence of nanoclay which acts as a “harder” phase within the PVDF matrix which is now less impacted by abrasive wearing as the nanoclay resists the wear with its higher mechanical strength [118]. However, Cloisite® 30B showed that the inclusion of nanomaterials does not always lead to improvement, and this must be balanced with other key properties, especially membrane morphology.

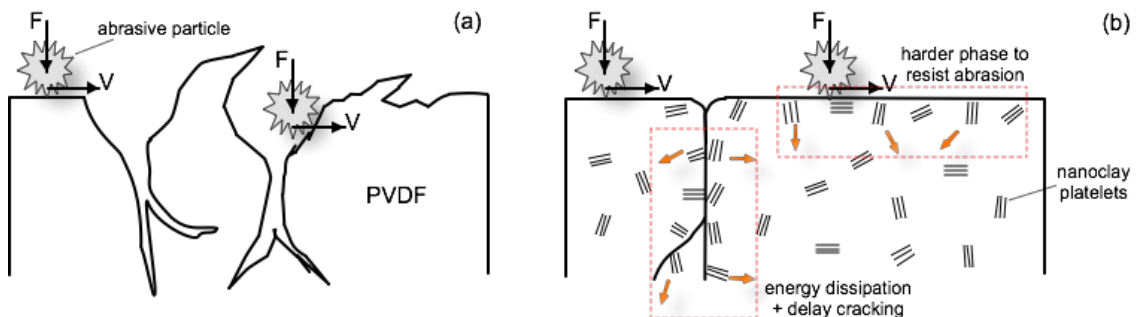


Figure 7-14. Proposed model for abrasion of (a) unmodified membrane and (b) the mechanically stabilized PVDF/nanoclay membrane

7.3. Conclusions

Nanoclay modified hollow fibre membranes were fabricated by phase inversion and high nanoclay retention was achieved at low initial nanoclay loading. The incorporation of nanoclay improved the membrane structure by suppressing finger-like void formation. Nanoclay also promoted a change of the PVDF crystalline phase from α - to β -phase, which increased polarity and brought about a more efficient energy-

dissipation mechanism in the nanocomposite membrane. Despite showing lower pure water permeability, nanocomposite membranes demonstrated stronger antifouling performance, mechanical strength and abrasion resistance with the Nanomer[®] I.44P 5.08 membrane lasting three times longer than the control membrane.

8. Conclusions and recommendations

As stated in Chapter 1, the aim of this thesis was to develop novel nanocomposite membrane materials that would improve on the durability and performance of polymeric hollow fibre membranes in water treatment, especially enhancing the membrane abrasion resistance to abrasive particles in feeds such as seawater. To realize this, a series of experiments and trials have been conducted to develop a new type of membrane via NIPS using inorganic/organic hybrid materials based on PVDF and modified montmorillonite nanoclays with NMP as the solvent. The specific objectives of this work were to:

1. explore the ability of different dispersion techniques to disperse nanoclays and propose theories as to how the techniques affect the membrane properties;
2. understand how nanoclay impacts the membrane properties including thermal properties, crystal structure, membrane morphology, water permeability, mechanical strength and abrasion resistance;
3. study the effect of casting conditions on flat sheet membrane properties including nanoclay retention, crystal structure, membrane morphology and mechanical strength;
4. demonstrate the performance of hollow fibre membrane, which is the more industrially applicable format, with the knowledge gained from objectives 1-3.

8.1. Conclusions

In this study, PVDF/nanoclay nanocomposite membranes demonstrated improved mechanical strength and abrasion resistance and were evaluated with water permeability and fouling tests for potential water treatment applications.

To produce uniform membranes, three conventional methods including overhead mixing, ultrasonication and planetary mixing were examined for their ability to disperse nanoclay in the solvent (NMP) along with a novel dispersion method using high shear mixing (microfluidizer). Among the three conventional methods, ultrasonication was the fastest and most effective in dispersing the clay into the smallest particle size within the shortest mixing time. The microfluidizer had the ability to further reduce the particle cluster size and to produce a stable dispersion in which the small particle size could be reinstated with ultrasonication after a period of stagnancy. While neither ultrasonication nor microfluidization exfoliated the nanoclay at a molecular level,

dispersing nanoclay with a microfluidizer formed more homogeneous nanocomposite membranes with superior mechanical properties. As such, the dispersion technique using combined ultrasonication and high shear mixing (microfluidizer) was used for the optimised fabrication approach applied to hollow fibres; which were the main membrane type to be studied for enhanced durability in this work.

While the employed technique did not exfoliate the nanoclay, as investigated using TEM and SAXS, complete exfoliation of clay was not necessary for enhanced mechanical strength and increased abrasion resistance in both flat sheet and hollow fibre membranes. In spite of phase separated morphology at high loading shown by SAXS, all nanocomposite PVDF/15A flat sheet membranes exhibited increased resistance to abrasion compared to the neat PVDF material tested with a standard tribology technique. For hollow fibre membranes examined using the abrasion slurry test, also, they all exhibited stronger abrasion resistance. For example, the Nanomer[®] I.44P 5.08 membrane lasted three times longer than the control membrane. Other than having the nanoclay particles act as a harder phase to resist abrasion on the membrane surface, it was proposed the improvement in mechanical strength and abrasion resistance was due to the shifting of PVDF crystalline phase from α - to β -phase with the incorporation of nanoclay, which increased polarity and brought about a more efficient energy-dissipation mechanism in the nanocomposite membranes. This crystalline phase change in PVDF was observed in both formats of membranes (flat sheet and hollow fibre).

The incorporation of nanoclay also impacted the membrane morphology, normally attributed to the membrane format and the casting conditions. Flat sheet membranes appeared to have deeper macrovoids as the Cloisite[®] 15A loading increased but for hollow fibre membranes the incorporation of nanoclay (Cloisite[®] 30B or Nanomer[®] I.44P) improved the membrane structure by reducing finger-like void formation. The difference in morphology could be due to the different types of nanoclay used in both studies and/or that the difference between flat sheet casting and hollow fibre extrusion has changed the nanoclay interaction with the PVDF. Changes in casting conditions also affected the morphology of nanocomposite membranes. Increases in air retention time, decreases in quench bath temperature and casting at high humidity increased the demixing rate which resulted in membranes with larger macrovoids and subsequently brought about weaker mechanical properties. Other than membrane morphology, casting conditions had an influence on nanoclay retention and the PVDF crystalline phase. Controlling morphology is a key priority in membrane

fabrication to meet the needs of the application, but nanoclay retention was found to be around 34%-48% in most conditions.

Both flat sheet and hollow fibre nanocomposite membranes had lower water permeability than the control membrane. This is most likely due to alteration of the membrane morphology related to water transport by the nanoparticles. Despite this drawback, fouling testing with automated backwashing using BSA and sodium alginate as model foulants, showed that the hollow fibre nanocomposite membranes were not more prone to fouling and had the potential to improve the membrane fouling performance at high nanoclay loading.

In conclusion, the incorporation of nanoclay into PVDF hollow fibre membranes was demonstrated for improving durability properties of value for the water treatment industry.

8.2. Recommendations for future work

The progress of this thesis showed the durability of PVDF membranes was enhanced with nanoclay incorporation but several opportunities for future work were also found. With the improvement observed in mechanical strength and abrasion resistance, the nanoclay reinforced PVDF membranes may also be suitable for improving other durability issues including fibre breakage as mentioned in the literature review. Pilot test with the more durable nanocomposite membranes along with statistical studies on membrane failure will be useful to evaluate this aspect.

This study examined the membrane abrasion resistance through a standard tribological technique and an in-house testing method using abrasive slurry and bubble point measurement. While the idea of using the abrasive slurry was to resemble more realistic conditions in water treatment applications, the abrasion test could be extended by preparing a pilot module with the nanocomposite membranes and running a real filtration test with feeds containing elevated levels of abrasive particles. Trans-membrane pressure is monitor across the module to give an indication of membrane performance and any defects that may have occurred. Also, membrane autopsy will identify which part of the membrane module experiences the greatest extent of abrasive wear. This further study will give a more practical insight of how nanocomposite membranes would perform in realistic aggressive water filtration conditions.

As observed in Section 4.1.3 and Section 5.2.4, the nanoclay appeared to have a phase separated morphology in the composite membranes. Although improved durability was demonstrated in those membranes, exfoliating the clay may potentially further enhance the membrane properties. This may be achieved by using a different solvent or dispersing the nanoclay with high shear force in the presence of polymer to avoid re-agglomeration and fully exfoliate the nanoclays. While these techniques may change nanoclay dispersion, other properties such as membrane morphology and polymer crystal structure may be affected as a result. As such, careful consideration has to be taken so that the desirable membrane properties can be maintained.

Also in Chapter 6, a series of casting conditions have been investigated for optimizing nanoclay retention in membranes. Although nanoclay retention was improved up to 48% by selecting the appropriate type of nanoclay and adding additives to quench bath, there is certainly room for further improvement. Since adding salt to the quench bath has improved nanoclay retention, procedures to increase nanoclay inclusion, such as the effect of stabilizing the charge of nanoclay by adding salt into the casting solution, could be investigated. Moreover, whether nanoclay leaching occurs during membrane filtration during long term operation should be examined and if so, its impact on membrane performance should be evaluated as well.

In addition, fouling tests with extended operating time (several days and beyond) is recommended for evaluating the behaviour of the abrasion resistant nanocomposite membrane as the test in this study was not sufficiently long enough to observe long term fouling behaviour. As the mode of fouling can change after extended filtration, from initial pore constriction to the build up of filter cake [149], a longer fouling test is needed to explore the membrane behaviour. Real water is also to be tested on top of model foulants to provide better understanding of the antifouling properties of the nanocomposite membranes in real conditions.

Finally, a decrease in water flux was observed in nanocomposite membranes in general although the trend was not conclusive. To improve filtration performance, more work on the fabrication process to establish better morphological control of nanocomposite membrane is needed. Procedures to produce consistent membrane properties such as membrane skin thickness, the contact angle, pore size, tortuosity and skin porosity are essential for reliable water permeation. Understanding the thermodynamics and kinetic effects of the addition of nanoparticles to the membrane system will be important for controlling these properties in order to produce durable and functional membranes.

Reference

- [1] H. Strathmann, L. Giorno, and E. Drioli, *An Introduction to Membrane Science and Technology*. 2011, Rome: Wiley.
- [2] T. Graham, On the law of the diffusion of gases, *Journal of Membrane Science*, 100 (1995) 17-21.
- [3] T. Graham, Notice of the singular inflation of a bladder, *Journal of Membrane Science*, 100 (1995) 9-9.
- [4] C.E. Reid and E.J. Breton, Water and ion flow across cellulosic membranes, *Journal of Applied Polymer Science*, 1 (1959) 133-143.
- [5] S. Loeb and S. Sourirajan, In: *Saline Water Conversion?II*, American Chemical Society, Ottawa, Canada, 1963, pp. 117-132.
- [6] M. Kurihara, Himeshima, Y., and Uemura, T. in *Preprints of ICOM*. 1987. Tokyo: The Aseanian Membrane Society.
- [7] A.W.W. Association, *Microfiltration and Ultrafiltration Membranes for Drinking Water (M53)*. 2011: American Water Works Association.
- [8] M.J. Hammer, *Water and wastewater technology*. Vol. 5th ,International. 2004, Upper Saddle River, N.J.; Great Britain: Prentice Hall/Pearson Education International. 540.
- [9] J.P. Chen, H. Mou, L.K. Wang, and T. Matsuura, In: L.K. Wang, Y.-T. Hung, and N.K. Shamas, *Advanced Physicochemical Treatment Processes*, Humana Press Inc., Totowa, NJ, 2006, pp. 203-259.
- [10] M. Ulbricht, Advanced functional polymer membranes, *Polymer*, 47 (2006) 2217-2262.
- [11] K. Li, *Ceramic membranes for separation and reaction*. 2007, Chichester, England: John Wiley & Sons, Ltd. 306.
- [12] R. Weber, H. Chmiel, and V. Mavrov, Characteristics and application of new ceramic nanofiltration membranes, *Desalination*, 157 (2003) 113.
- [13] C.V. Funk and D.R. Lloyd, Zeolite-filled microporous mixed matrix (ZeoTIPS) membranes: Prediction of gas separation performance, *Journal of Membrane Science*, 313 (2008) 224-231.
- [14] G.E. Wetterau, M.M. Clark, and C. Anselme, A dynamic model for predicting fouling effects during the ultrafiltration of a groundwater, *Journal of Membrane Science*, 109 (1996) 185-204.
- [15] M.D. Kennedy, J. Kamanyi, S.G.S. Rodríguez, N.H. Lee, J.C. Schippers, and G. Amy, In: *Advanced Membrane Technology and Applications*, John Wiley & Sons, Inc., Hoboken, NJ, USA, 2008, pp. 131-170.
- [16] J.S. Baker and L.Y. Dudley, Biofouling in membrane systems — A review, *Desalination*, 118 (1998) 81-89.
- [17] E.M. Vrijenhoek, S. Hong, and M. Elimelech, Influence of membrane surface properties on initial rate of colloidal fouling of reverse osmosis and nanofiltration membranes, *Journal of Membrane Science*, 188 (2001) 115-128.
- [18] V. Parida and H.Y. Ng, Forward osmosis organic fouling: Effects of organic loading, calcium and membrane orientation, *Desalination*, 312 (2013) 88-98.
- [19] C. Boo, M. Elimelech, and S. Hong, Fouling control in a forward osmosis process integrating seawater desalination and wastewater reclamation, *Journal of Membrane Science*, 444 (2013) 148-156.
- [20] M. Herzberg and M. Elimelech, Biofouling of reverse osmosis membranes: Role of biofilm-enhanced osmotic pressure, *Journal of Membrane Science*, 295 (2007) 11-20.
- [21] A.E. Contreras, Z. Steiner, J. Miao, R. Kasher, and Q. Li, Studying the Role of Common Membrane Surface Functionalities on Adsorption and Cleaning of

- Organic Foulants Using QCM-D, *Environmental Science & Technology*, 45 (2011) 6309-6315.
- [22] C. Liao, J. Zhao, P. Yu, H. Tong, and Y. Luo, Synthesis and characterization of SBA-15/poly (vinylidene fluoride) (PVDF) hybrid membrane, *Desalination*, 260 (2010) 147-152.
- [23] S.J. Oh, N. Kim, and Y.T. Lee, Preparation and characterization of PVDF/TiO₂ organic-inorganic composite membranes for fouling resistance improvement, *Journal of Membrane Science*, 345 (2009) 13-20.
- [24] L. Yan, Y.S. Li, and C.B. Xiang, Preparation of poly(vinylidene fluoride)(pvdf) ultrafiltration membrane modified by nano-sized alumina (Al₂O₃) and its antifouling research, *Polymer*, 46 (2005) 7701-7706.
- [25] L.-Y. Yu, Z.-L. Xu, H.-M. Shen, and H. Yang, Preparation and characterization of PVDF–SiO₂ composite hollow fiber UF membrane by sol–gel method, *Journal of Membrane Science*, 337 (2009) 257-265.
- [26] L.-Y. Yu, H.-M. Shen, and Z.-L. Xu, PVDF–TiO₂ composite hollow fiber ultrafiltration membranes prepared by TiO₂ sol–gel method and blending method, *Journal of Applied Polymer Science*, 113 (2009) 1763-1772.
- [27] P. Wang, J. Ma, Z. Wang, F. Shi, and Q. Liu, Enhanced Separation Performance of PVDF/PVP-g-MMT Nanocomposite Ultrafiltration Membrane Based on the NVP-Grafted Polymerization Modification of Montmorillonite (MMT), *Langmuir*, 28 (2012) 4776-4786.
- [28] S.R. Gray, R. Semiat, M. Duke, A. Rahardianto, and Y. Cohen, In: P. Wilderer, *Treatise on Water Science*, Academic Press, Oxford, 2011, pp. 73-109.
- [29] N. Voutchkov, *Pretreatment Technologies for Membrane Seawater Desalination*. 2008: Australian Water Association.
- [30] F. Knops, S. van Hoof, H. Futselaar, and L. Broens, Economic evaluation of a new ultrafiltration membrane for pretreatment of seawater reverse osmosis, *Desalination*, 203 (2007) 300-306.
- [31] M. Busch, R. Chu, and S. Rosenberg, Novel Trends in Dual Membrane Systems for Seawater Desalination: Minimum Primary Pretreatment and Low Environmental Impact Treatment Schemes, *IDA Journal of Desalination and Water Reuse*, 2 (2010) 56-71.
- [32] Evaluation of Membrane Pretreatment for Seawater Reverse Osmosis Desalination, B.o.R. U.S. Department of the Interior, 2007
- [33] E. Gasia-Bruch, P. Sehn, V. Garcia-Molina, M. Busch, O. Raize, and M. Negrin, Field experience with a 20,000 m³/d integrated membrane seawater desalination plant in Cyprus, *Desalination and Water Treatment*, 31 (2011) 178-189.
- [34] Conventional or Membrane Filtration for Seawater RO?, S.M.S. Bhd., 2008
- [35] *Membrane Filtration (MF/UF)*. 2007, American Membrane Technology Association: Stuart, Florida.
- [36] R.M. Stear, J. Parr, and M.D. Smith. *Decreasing freshwater demand: dual supplies*. in *23rd WEDC Conference, Water and Sanitation for All*. 1997. Durban, South Africa.
- [37] S.P. Chesters, N. Pena, S. Gallego, M. Fazel, M.W. Armstrong, and F. del Vigo. *Results from 99 seawater RO membrane autopsies*. in *IDA World Congress*. 2011. Perth, Western Australia.
- [38] N. Voutchkov, Considerations for selection of seawater filtration pretreatment system, *Desalination*, 261 (2010) 354-364.
- [39] R.W. Sheldon, A. Praksh, and J. W. H. Sutcliffe, The size distribution of particles in the ocean, *Limnology and oceanography*, 17 (1972) 327-340.

- [40] I.N. McCave, Size spectra and aggregation of suspended particles in the deep ocean, *Deep Sea Research Part A. Oceanographic Research Papers*, 31 (1984) 329-352.
- [41] H. Guo, Y. Wyart, J. Perot, F. Nauleau, and P. Moulin, Low-pressure membrane integrity tests for drinking water treatment: A review, *Water Research*, 44 (2010) 41-57.
- [42] A.J. Gijsbertsen-Abrahamse, E.R. Cornelissen, and J.A.M.H. Hofman, Fiber failure frequency and causes of hollow fiber integrity loss, *Desalination*, 194 (2006) 251-258.
- [43] A.E. Childress, P. Le-Clech, J.L. Daugherty, C. Chen, and G.L. Leslie, Mechanical analysis of hollow fiber membrane integrity in water reuse applications, *Desalination*, 180 (2005) 5-14.
- [44] K.V. Pochiraju, G.P. Tandon, and G.A. Schoeppner, *Long-Term Durability of Polymeric Matrix Composites*. 2011, New York, NY, USA: Springer.
- [45] S.C. Tjong, Structural and mechanical properties of polymer nanocomposites, *Materials Science and Engineering: R: Reports*, 53 (2006) 73-197.
- [46] A. Takahara, T. Magnome, and T. Kajiyama, Effect of glass fiber-matrix polymer interaction on fatigue characteristics of short glass fiber-reinforced poly(butylene terephthalate) based on dynamic viscoelastic measurement during the fatigue process, *Journal of Polymer Science, Part B: Polymer Physics*, 32 (1994) 839-849.
- [47] H. Unal, A. Mimaroglu, and M. Alkan, Mechanical properties and morphology of nylon-6 hybrid composites, *Polymer International*, 53 (2004) 56-60.
- [48] W. Li, X. Sun, C. Wen, H. Lu, and Z. Wang, Preparation and characterization of poly (vinylidene fluoride)/TiO₂ hybrid membranes, *Frontiers of Environmental Science & Engineering*, 7 (2013) 492-502.
- [49] S.Y. Lee, H.J. Kim, R. Patel, S.J. Im, J.H. Kim, and B.R. Min, Silver nanoparticles immobilized on thin film composite polyamide membrane: characterization, nanofiltration, antifouling properties, *Polymers for Advanced Technologies*, 18 (2007) 562-568.
- [50] M. Mulder, *Basic principles of membrane technology*. 2nd ed. 1996, Dordrecht ; Boston: Kluwer Academic.
- [51] N. Kubota, T. Hashimoto, and Y. Mori, In: *Advanced Membrane Technology and Applications*, John Wiley & Sons, Inc., 2008, pp. 101-129.
- [52] M. Pilutti and J.E. Nemeth, *Technical and cost review of commercially available MF/UF membrane products*. 2003, International Desalination Association.
- [53] D. Shah, P. Maiti, E. Gunn, D.F. Schmidt, D.D. Jiang, C.A. Batt, and E.P. Giannelis, Dramatic Enhancements in Toughness of Polyvinylidene Fluoride Nanocomposites via Nanoclay-Directed Crystal Structure and Morphology, *Advanced Materials*, 16 (2004) 1173-1177.
- [54] A.J. Lovinger, In: D.C. Bassett, *Development in Crystalline Polymers*, Applied Science Publishers, London, 1982, pp.
- [55] J. Sa-nguanrukksa, R. Rujiravanit, P. Supaphol, and S. Tokura, Porous polyethylene membranes by template-leaching technique: preparation and characterization, *Polymer Testing*, 23 (2004) 91.
- [56] G. Mago, D.M. Kalyon, and F.T. Fisher, Membranes of polyvinylidene fluoride and PVDF nanocomposites with carbon nanotubes via immersion precipitation, *Journal of Nanomaterials*, 2008 (2008).
- [57] R.W. Baker, *Membrane technology and applications*. 2nd ed. 2004, Chichester, UK: J. Wiley.
- [58] C. Hiatt W, H. Vitzthum G, B. Wagener K, K. Gerlach, and C. Josefiak, In: *Materials Science of Synthetic Membranes*, American Chemical Society, 1985, pp. 229-244.

- [59] F. Liu, N.A. Hashim, Y. Liu, M.R.M. Abed, and K. Li, Progress in the production and modification of PVDF membranes, *Journal of Membrane Science*, 375 (2011) 1-27.
- [60] M. Khayet, In: *Advanced Membrane Technology and Applications*, John Wiley & Sons, Inc., 2008, pp. 297-369.
- [61] Y. Su, C.X. Chen, Y.G. Li, and J.D. Li, PVDF membrane formation via thermally induced phase separation, *Journal of Macromolecular Science Part a-Pure and Applied Chemistry*, 44 (2007) 99-104.
- [62] D.R. Lloyd, K.E. Kinzer, and H.S. Tseng, Microporous membrane formation via thermally induced phase separation. I. Solid-liquid phase separation, *Journal of Membrane Science*, 52 (1990) 239-261.
- [63] M. Gu, J. Zhang, X. Wang, H. Tao, and L. Ge, Formation of poly(vinylidene fluoride) (PVDF) membranes via thermally induced phase separation, *Desalination*, 192 (2006) 160-167.
- [64] Z.-Y. Cui, C.-H. Du, Y.-Y. Xu, G.-L. Ji, and B.-K. Zhu, Preparation of porous PVdF membrane via thermally induced phase separation using sulfolane, *Journal of Applied Polymer Science*, 108 (2008) 272-280.
- [65] J.D. Ferry, Ultrafilter Membranes and Ultrafiltration, *Chemical Reviews*, 18 (1936) 373-455.
- [66] K. Nakagawa, H. Matsuyama, T. Maki, M. Teramoto, and N. Kubota, Preparation of mesoporous silica membrane by solvent evaporation method for filtration application, *Separation and Purification Technology*, 44 (2005) 145-151.
- [67] R. Zsigmondy and W. Bachmann, Über neue Filter, *Zeitschrift für anorganische und allgemeine Chemie*, 103 (1918) 119-128.
- [68] Y.S. Su, C.Y. Kuo, D.M. Wang, J.Y. Lai, A. Deratani, C. Pochat, and D. Bouyer, Interplay of mass transfer, phase separation, and membrane morphology in vapor-induced phase separation, *Journal of Membrane Science*, 338 (2009) 17-28.
- [69] C.-L. Li, D.-M. Wang, A. Deratani, D. Quemener, D. Bouyer, and J.-Y. Lai, Insight into the preparation of poly(vinylidene fluoride) membranes by vapor-induced phase separation, *Journal of Membrane Science*, 361 (2010) 154-166.
- [70] R.W. Baker, *Membrane Technology and Applications*. 3rd ed. 2012, Chichester, UK: John Wiley and Sons.
- [71] P. Sukitpaneenit and T.-S. Chung, Molecular elucidation of morphology and mechanical properties of PVDF hollow fiber membranes from aspects of phase inversion, crystallization and rheology, *Journal of Membrane Science*, 340 (2009) 192-205.
- [72] T.-S. Chung, E.R. Kafchinski, and R. Vora, Development of a defect-free 6FDA-durene asymmetric hollow fiber and its composite hollow fibers, *Journal of Membrane Science*, 88 (1994) 21-36.
- [73] D.-M. Wang, F.-C. Lin, T.-T. Wu, and J.-Y. Lai, Formation mechanism of the macrovoids induced by surfactant additives, *Journal of Membrane Science*, 142 (1998) 191-204.
- [74] T.-H. Young, L.-P. Cheng, D.-J. Lin, L. Fane, and W.-Y. Chuang, Mechanisms of PVDF membrane formation by immersion-precipitation in soft (1-octanol) and harsh (water) nonsolvents, *Polymer*, 40 (1999) 5315-5323.
- [75] C.-Y. Kuo, H.-N. Lin, H.-A. Tsai, D.-M. Wang, and J.-Y. Lai, Fabrication of a high hydrophobic PVDF membrane via nonsolvent induced phase separation, *Desalination*, 233 (2008) 40-47.
- [76] J.F. Hester and A.M. Mayes, Design and performance of foul-resistant poly(vinylidene fluoride) membranes prepared in a single-step by surface segregation, *Journal of Membrane Science*, 202 (2002) 119-135.

- [77] S. Yang and Z. Liu, Preparation and characterization of polyacrylonitrile ultrafiltration membranes, *Journal of Membrane Science*, 222 (2003) 87-98.
- [78] X. Wang, L. Zhang, D. Sun, Q. An, and H. Chen, Effect of coagulation bath temperature on formation mechanism of poly(vinylidene fluoride) membrane, *Journal of Applied Polymer Science*, 110 (2008) 1656-1663.
- [79] M.L. Yeow, Y.T. Liu, and K. Li, Morphological study of poly(vinylidene fluoride) asymmetric membranes: Effects of the solvent, additive, and dope temperature, *Journal of Applied Polymer Science*, 92 (2004) 1782-1789.
- [80] L.-P. Cheng, Effect of Temperature on the Formation of Microporous PVDF Membranes by Precipitation from 1-Octanol/DMF/PVDF and Water/DMF/PVDF Systems, *Macromolecules*, 32 (1999) 6668-6674.
- [81] T.-S. Chung, E.R. Kafchinski, and P. Foley, Development of asymmetric hollow fibers from polyimides for air separation, *Journal of Membrane Science*, 75 (1992) 181-195.
- [82] I.M. Wienk, F.H.A. Olde Scholtenhuis, T. van den Boomgaard, and C.A. Smolders, Spinning of hollow fiber ultrafiltration membranes from a polymer blend, *Journal of Membrane Science*, 106 (1995) 233-243.
- [83] H.-Y. Hwang, D.-J. Kim, H.-J. Kim, Y.-T. Hong, and S.-Y. Nam, Effect of nanoclay on properties of porous PVdF membranes, *Transactions of Nonferrous Metals Society of China*, 21 (2011) 141-147.
- [84] M. Khayet, The effects of air gap length on the internal and external morphology of hollow fiber membranes, *Chemical Engineering Science*, 58 (2003) 3091-3104.
- [85] D. Wang, K. Li, and W.K. Teo, Preparation and characterization of polyvinylidene fluoride (PVDF) hollow fiber membranes, *Journal of Membrane Science*, 163 (1999) 211-220.
- [86] M.G. Buonomenna, P. Macchi, M. Davoli, and E. Drioli, Poly(vinylidene fluoride) membranes by phase inversion: the role the casting and coagulation conditions play in their morphology, crystalline structure and properties, *European Polymer Journal*, 43 (2007) 1557-1572.
- [87] B. Ameduri, From Vinylidene Fluoride (VDF) to the Applications of VDF-Containing Polymers and Copolymers: Recent Developments and Future Trends, *Chemical Reviews*, 109 (2009) 6632-6686.
- [88] H. Kawai, The Piezoelectricity of Poly (vinylidene Fluoride), *Japanese Journal of Applied Physics*, 8 (1969) 975-976.
- [89] Q.M. Zhang, V. Bharti, and X. Zhao, Giant Electrostriction and Relaxor Ferroelectric Behavior in Electron-Irradiated Poly(vinylidene fluoride-trifluoroethylene) Copolymer, *Science*, 280 (1998) 2101-2104.
- [90] Q.-Y. Peng, P.-H. Cong, X.-J. Liu, T.-X. Liu, S. Huang, and T.-S. Li, The preparation of PVDF/clay nanocomposites and the investigation of their tribological properties, *Wear*, 266 (2009) 713-720.
- [91] M. Gu, J. Zhang, X. Wang, and W. Ma, Crystallization behavior of PVDF in PVDF-DMP system via thermally induced phase separation, *Journal of Applied Polymer Science*, 102 (2006) 3714-3719.
- [92] R. Belouadah, D. Kendil, E. Bousbiat, D. Guyomar, and B. Guiffard, Electrical properties of two-dimensional thin films of the ferroelectric material Polyvinylidene Fluoride as a function of electric field, *Physica B: Condensed Matter*, 404 (2009) 1746-1751.
- [93] K. Ebert, D. Fritsch, J. Koll, and C. Tjahjawiguna, Influence of inorganic fillers on the compaction behaviour of porous polymer based membranes, *Journal of Membrane Science*, 233 (2004) 71-78.

- [94] L.F. Han, Z.L. Xu, L.Y. Yu, Y.M. Wei, and Y. Cao, Performance of PVDF/Multi-nanoparticles composite hollow fibre ultrafiltration membranes, *Iranian Polymer Journal (English Edition)*, 19 (2010) 553-565.
- [95] E. Yuliwati, A.F. Ismail, T. Matsuura, M.A. Kassim, and M.S. Abdullah, Effect of modified PVDF hollow fiber submerged ultrafiltration membrane for refinery wastewater treatment, *Desalination*, 283 (2011) 214-220.
- [96] A. Bottino, G. Capannelli, V. D'Asti, and P. Piaggio, Preparation and properties of novel organic-inorganic porous membranes, *Separation and Purification Technology*, 22-23 (2001) 269-275.
- [97] C. Ribeiro, J.A. Panadero, V. Sencadas, S. Lanceros-Méndez, M.N. Tamaño, D. Moratal, M. Salmerón-Sánchez, and J.L.G. Ribelles, Fibronectin adsorption and cell response on electroactive poly(vinylidene fluoride) films, *Biomedical Materials*, 7 (2012) 035004:1–035004:10.
- [98] W. Huang, K. Edenzon, L. Fernandez, S. Razmpour, J. Woodburn, and P. Cebe, Nanocomposites of poly(vinylidene fluoride) with multiwalled carbon nanotubes, *Journal of Applied Polymer Science*, 115 (2010) 3238-3248.
- [99] Y. Xu, W.-T. Zheng, W.-X. Yu, L.-G. Hua, Y.-J. Zhang, and Z.-D. Zhao, Crystallization behavior and mechanical properties of poly (vinylidene fluoride)/multi-walled carbon nanotube nanocomposites, *Chem Res Chinese Universities*, 26 (2010) 491.
- [100] V. Causin, M.L. Carraro, C. Marega, R. Saini, S. Campestrini, and A. Marigo, Structure and morphology of solution blended poly(vinylidene fluoride)/montmorillonite nanocomposites, *Journal of Applied Polymer Science*, 109 (2008) 2354-2361.
- [101] T.U. Patro, M.V. Mhalgi, D.V. Khakhar, and A. Misra, Studies on poly(vinylidene fluoride)-clay nanocomposites: Effect of different clay modifiers, *Polymer*, 49 (2008) 3486-3499.
- [102] M. Alexandre and P. Dubois, Polymer-layered silicate nanocomposites: preparation, properties and uses of a new class of materials, *Materials Science and Engineering: R: Reports*, 28 (2000) 1-63.
- [103] S. Pavlidou and C.D. Papaspyrides, A review on polymer-layered silicate nanocomposites, *Progress in Polymer Science*, 33 (2008) 1119-1198.
- [104] N. Dayma, B.K. Satapathy, and A. Patnaik, Structural correlations to sliding wear performance of PA-6/PP-g-MA/nanoclay ternary nanocomposites, *Wear*, 271 (2011) 827-836.
- [105] B. Pan, Y. Xing, C. Zhang, and Y. Zhang, Study on erosion wear behavior of PDCPD/MMT nanocomposite, *Advanced Materials Research*, 123-125 (2010) 231-234.
- [106] G. Beyer, Nanocomposites: a new class of flame retardants for polymers, *Plastics, Additives and Compounding*, 4 (2002) 22-28.
- [107] W. Yu, Z. Zhao, W. Zheng, B. Long, Q. Jiang, G. Li, and X. Ji, Crystallization behavior of poly(vinylidene fluoride)/montmorillonite nanocomposite, *Polymer Engineering & Science*, 49 (2009) 491-498.
- [108] K.Y. Wang, S.W. Foo, and T.S. Chung, Mixed matrix PVDF hollow fiber membranes with nanoscale pores for desalination through direct contact membrane distillation, *Industrial and Engineering Chemistry Research*, 48 (2009) 4474-4483.
- [109] L. Priya and J.P. Jog, Polymorphism in intercalated poly(vinylidene fluoride)/clay nanocomposites, *Journal of Applied Polymer Science*, 89 (2003) 2036-2040.
- [110] J. Liu, W.-J. Boo, A. Clearfield, and H.-J. Sue, Intercalation and Exfoliation: A Review on Morphology of Polymer Nanocomposites Reinforced by Inorganic Layer Structures, *Materials and Manufacturing Processes*, 21 (2006) 143 - 151.

- [111] Q.T. Nguyen and D.G. Baird, An improved technique for exfoliating and dispersing nanoclay particles into polymer matrices using supercritical carbon dioxide, *Polymer*, 48 (2007) 6923-6933.
- [112] T.D. Fornes and D.R. Paul, Modeling properties of nylon 6/clay nanocomposites using composite theories, *Polymer*, 44 (2003) 4993-5013.
- [113] D.R. Dillon, K.K. Tenneti, C.Y. Li, F.K. Ko, I. Sics, and B.S. Hsiao, On the structure and morphology of polyvinylidene fluoride-nanoclay nanocomposites, *Polymer*, 47 (2006) 1678-1688.
- [114] T. Panagiotou, J.M. Bernard, and S.V. Mesite. *Deagglomeration and dispersion of carbon nanotubes using microfluidizer high shear fluid processors*. in *Nano Science and Technology Institute (NSTI) Conference and Expo Proceedings*. 2008.
- [115] S. Mahdi Jafari, Y. He, and B. Bhandari, Nano-Emulsion Production by Sonication and Microfluidization—A Comparison, *International Journal of Food Properties*, 9 (2006) 475-485.
- [116] S.N. Ratner, I.I. Farberoua, O.V. Radyukeich, and E.G. Lure, Connection between the wear resistance of plastics and other mechanical properties, *Soviet Plastics*, (1964).
- [117] J.K. Lancaster, Relationships between the Wear of Polymers and their Mechanical Properties, *Proceedings of the Institution of Mechanical Engineers, Conference Proceedings*, 183 (1968) 98-106.
- [118] S.K. Sinha and B.J. Briscoe, In: *Encyclopedia of Polymer Science and Technology, Concise*, John Wiley & Sons, Inc., Hoboken, NJ, USA, 2006, pp.
- [119] H.-J. Lee, M.K. Cho, Y.Y. Jo, K.-S. Lee, H.-J. Kim, E. Cho, S.-K. Kim, D. Henkensmeier, T.-H. Lim, and J.H. Jang, Application of TGA techniques to analyze the compositional and structural degradation of PEMFC MEAs, *Polymer Degradation and Stability*, 97 (2012) 1010-1016.
- [120] Methods of test for supplementary cementitious materials for use with portland cement - Determination of loss on ignition. AS 3583.3-1991. Standards Australia.
- [121] B. Mohammadi, A.A. Yousefi, and S.M. Bellah, Effect of tensile strain rate and elongation on crystalline structure and piezoelectric properties of PVDF thin films, *Polymer Testing*, 26 (2007) 42-50.
- [122] M. Zhang, A.-Q. Zhang, B.-K. Zhu, C.-H. Du, and Y.-Y. Xu, Polymorphism in porous poly(vinylidene fluoride) membranes formed via immersion precipitation process, *Journal of Membrane Science*, 319 (2008) 169-175.
- [123] K. Sutherland, *Filters and Filtration Handbook*. 5th ed. 2008, Oxford: Elsevier.
- [124] *Membrane filtration guidance manual*. 2005, United States Environmental Protection Agency.
- [125] D.T. Myat, M. Mergen, O. Zhao, M.B. Stewart, J.D. Orbell, and S. Gray, Characterisation of organic matter in IX and PACl treated wastewater in relation to the fouling of a hydrophobic polypropylene membrane, *Water Research*, 46 (2012) 5151-5164.
- [126] A.I. Schäfer, A.G. Fane, and T.D. Waite, Fouling effects on rejection in the membrane filtration of natural waters, *Desalination*, 131 (2000) 215-224.
- [127] *Cloisite® 30B Typical Physical Properties Bulletin*. 2008, Southern Clay Products: Gonzales, Texas.
- [128] A. Bottino, G. Capannelli, and A. Comite, Preparation and characterization of novel porous PVDF-ZrO₂ composite membranes, *Desalination*, 146 (2002) 35-40.
- [129] V.S. Nguyen, D. Rouxel, R. Hadji, B. Vincent, and Y. Fort, Effect of ultrasonication and dispersion stability on the cluster size of alumina nanoscale particles in aqueous solutions, *Ultrasonics Sonochemistry*, 18 (2011) 382-388.

- [130] M.M. Hirschler, Effect of oxygen on the thermal decomposition of poly(vinylidene fluoride), *European Polymer Journal*, 18 (1982) 463-467.
- [131] G. Botelho, S. Lanceros-Mendez, A.M. Goncalves, V. Sencadas, and J.G. Rocha, Relationship between processing conditions, defects and thermal degradation of poly(vinylidene fluoride) in the β -phase, *Journal of Non-Crystalline Solids*, 354 (2008) 72-78.
- [132] H. Li and H. Kim, Thermal degradation and kinetic analysis of PVDF/modified MMT nanocomposite membranes, *Desalination*, 234 (2008) 9-15.
- [133] *Cloisite® 15A Typical Physical Properties Bulletin*. 2008, Southern Clay Products: Gonzales, Texas.
- [134] Y. Ma, F. Shi, Z. Wang, M. Wu, J. Ma, and C. Gao, Preparation and characterization of PSf/clay nanocomposite membranes with PEG 400 as a pore forming additive, *Desalination*, 286 (2012) 131-137.
- [135] C.A. Smolders, A.J. Reuvers, R.M. Boom, and I.M. Wienk, Microstructures in phase-inversion membranes. Part 1. Formation of macrovoids, *Journal of Membrane Science*, 73 (1992) 259-275.
- [136] B.J. Chisholm, R.B. Moore, G. Barber, F. Khouri, A. Hempstead, M. Larsen, E. Olson, J. Kelley, G. Balch, and J. Caraher, Nanocomposites Derived from Sulfonated Poly(butylene terephthalate), *Macromolecules*, 35 (2002) 5508-5516.
- [137] M.-K. Song, S.-B. Park, Y.-T. Kim, K.-H. Kim, S.-K. Min, and H.-W. Rhee, Characterization of polymer-layered silicate nanocomposite membranes for direct methanol fuel cells, *Electrochimica Acta*, 50 (2004) 639-643.
- [138] L. Shi, R. Wang, Y. Cao, C. Feng, D.T. Liang, and J.H. Tay, Fabrication of poly(vinylidene fluoride-co-hexafluoropropylene) (PVDF-HFP) asymmetric microporous hollow fiber membranes, *Journal of Membrane Science*, 305 (2007) 215-225.
- [139] H.A. Tsai, M.J. Hong, G.S. Huang, Y.C. Wang, C.L. Li, K.R. Lee, and J.Y. Lai, Effect of DGDE additive on the morphology and pervaporation performances of asymmetric PSf hollow fiber membranes, *Journal of Membrane Science*, 208 (2002) 233-245.
- [140] M. Khalid, A.F. Ismail, C.T. Ratnam, Y. Faridah, W. Rashmi, and M.F. Al Khatib, Effect of radiation dose on the properties of natural rubber nanocomposite, *Radiation Physics and Chemistry*, 79 (2010) 1279-1285.
- [141] J. Carretero-Gonzalez, H. Retsos, E.P. Giannelis, T.A. Ezquerro, M. Hernandez, and M.A. Lopez-Manchado, Miscibility-dispersion, interfacial strength and nanoclay mobility relationships in polymer nanocomposites, *Soft Matter*, 5 (2009) 3481-3486.
- [142] H. Cai, F. Yan, Q. Xue, and W. Liu, Investigation of tribological properties of Al₂O₃-polyimide nanocomposites, *Polymer Testing*, 22 (2003) 875-882.
- [143] B.-S. Chiou, E. Yee, G.M. Glenn, and W.J. Orts, Rheology of starch-clay nanocomposites, *Carbohydrate Polymers*, 59 (2005) 467-475.
- [144] W.-H. Seol, Y.M. Lee, and J.-K. Park, Preparation and characterization of new microporous stretched membrane for lithium rechargeable battery, *Journal of Power Sources*, 163 (2006) 247-251.
- [145] M.A. Frommer, R. Matz, and U. Rosenthal, Mechanism of Formation of Reverse Osmosis Membranes. Precipitation of Cellulose Acetate Membranes in Aqueous Solutions, *Product R&D*, 10 (1971) 193-196.
- [146] K.-Y. Lin, D.-M. Wang, and J.-Y. Lai, Nonsolvent-Induced Gelation and Its Effect on Membrane Morphology, *Macromolecules*, 35 (2002) 6697-6706.
- [147] M.K. Souhaimi and T. Matsuura, *Membrane Distillation: Principles and Applications*. 2011: Elsevier Science.

- [148] L. Yan, Y.S. Li, C.B. Xiang, and S. Xianda, Effect of nano-sized Al₂O₃-particle addition on PVDF ultrafiltration membrane performance, *Journal of Membrane Science*, 276 (2006) 162-167.
- [149] D.T. Myat, M. Mergen, O. Zhao, M.B. Stewart, J.D. Orbell, T. Merle, J.-P. Croué, and S. Gray, Effect of IX dosing on polypropylene and PVDF membrane fouling control, *Water Research*, 47 (2013) 3827-3834.